University of California
Los Angeles

Modeling the Mechanics of the Cytoskeleton

A dissertation submitted in partial satisfaction
of the requirements for the degree
Doctor of Philosophy in Mechanical Engineering

by

Mo Bai

2012

ABSTRACT OF THE DISSERTATION

Modeling the Mechanics of the Cytoskeleton

by

Mo Bai

Doctor of Philosophy in Mechanical Engineering

University of California, Los Angeles, 2012

Professor William S. Klug, Chair

This dissertation investigates the mechanics of semiflexible filament network and the effects of polydispersity, anisotropy, and labile crosslinks through numerical simulations. The study first demonstrates that the single parameter nonaffinity length λ derived from monodisperse semiflexible filament network no longer holds for polydisperse and nematic anisotropic networks; it then extends the static response of network to dynamic response by allowing crosslinks to break and rebind according to Bell's law.

This study starts with exploring the effects of filament length polydispersity on the mechanical properties of semiflexible network. Extending previous studies on monodisperse network, the responses of networks of bimodal and exponential length distributions are tested numerically. It is found that in polydisperse networks, mixtures of long and short filaments interact cooperatively to generally produce mechanical response closer to the affine prediction than comparable monodisperse networks of either long or short filaments. Overall, length polydispersity has the effect of sharpening and shifting the affine/nonaffine(A/NA) transition to lower network densities.

The effect of adding long, stiff filaments to a semiflexible network is studied next. It is shown that the addition of a small fraction of longer and stiffer filaments (microtubules) to a nonaffine network (actin filaments) leads to a significant increase in its overall elastic moduli, even though the long filaments do not form a stress bearing network by themselves. Moreover, there is a strong negative correlation between long filament density and local

geometric measures of nonaffinity.

Anisotropic, monodisperse network is then investigated and like isotropic networks, it undergoes an A/NA transition controlled by the ratio of the filament length to the nonaffinity length λ. Deep in the nonaffine regime, however, these anisotropic networks exhibit a vanishing linear response regime for highly ordered networks and a dependence of the shear modulus on shear direction. These features can be understood in terms of a generalized floppy modes analysis of the nonaffine mechanics and a type of cooperative Euler buckling, which are discussed in this study, too.

Lastly, by allowing crosslinks to break and rebind, network's dynamic response is studied. It is shown that force-induced crosslink breakage leads to significant creeping and the network retains part of its elastic modulus even after significant plastic flow. The spatial correlation of crosslink breakage is also studied.

This simulation approach provides an important way to investigate the complex static and dynamic response of semiflexible filament network. Its results have been compared with analytical analysis and experimental data which prove its validity. The study provides several important insights on the fundamental mechanism of semiflexible network and cytoskeleton under static/dynamic loading, the design of experiment on both *in vivo* and *in vitro* cytoskeletal network, and even the design of a novel, synthetic polymer material.

The dissertation of Mo Bai is approved.

Jiun-Shyan (JS) Chen

Pirouz Kavehpour

Alex J. Levine

William S. Klug, Committee Chair

University of California, Los Angeles

2012

To my family

Table of Contents

List of Figures

Acknowledgments

First of all, I would like to express my sincere appreciation and thanks to my advisor, Bill Klug. I'm grateful for the opportunity to have worked in his lab and learned from him. Throughout my years at UCLA, he has provided continuous guidance, patience and support for my academic and professional endeavors. His extensive knowledge, excitement for mechanics, and kindness will always be my inspiration. I'm thankful to have worked with my co-advisor, Alex Levine, who has led me through the exciting world of biophysics. I'm also indebted to my former advisor from University of Florida, Jacob Chung, who has supported and encouraged me to pursue my dreams. Thanks to Jiun-Shyan Chen and Pirouz Kavehpour for serving in my committee and helpful discussions.

I'm grateful to have collaborated with Andrew Missel on many fruitful projects, for his helpful discussion on coding and physics. Roie Shlomovitz has generously assisted in my research through suggestion and discussion. Their help is greatly appreciated.

I have had an extremely wonderful time spent with my office-mates: Lin, Ankush, Jee, and Luigi. I wouldn't have been feeling so comfortable working in the lab without their kindness, help, humor and encouragement. I'm thankful to all my friends I met at UCLA, who have made my four years here so colorful, enjoyable, and memorable.

Finally, I owe special thanks to my family. My parents have always encouraged me to pursue my dreams and given me the support whenever I need them. I'm indebted to have my wife, Wenwen, by my side through so many years. This work would not be possible without her sacrifice, caring, and unconditional love. So, this work is dedicated to you.

Vita

2001-2005	B.S. Hydraulic Engineering, Tsinghua University, Beijing, China
2005-2007	M.S. Mechanical Engineering, University of Florida, Gainesville, FL, U.S.
2008-2012	Graduate student, Mechanical and Aerospace Engineering, University of California, Los Angeles, CA, U.S.

CHAPTER 1

Introduction

Eukaryotic cells present a lot of interesting engineering lessons. The mechanical behavior of cell is of great interest to many scientists and researchers. The interior of these eukaryotic cells is filled with a low density, chemically heterogeneous biopolymer gel, so called the cytoskeleton. The cytoskeleton is the main source of force generation and controls the deformation of cells.

In spite of the chemical complexity of the cytoskeleton, it appears from a variety of experiments that the fundamental mechanics of cells stem primarily from the filaments, crosslinks, and molecular motors, which are the building blocks of cytoskeleton. Finding the quantitative relation between the microstructure of cytoskeleton and its observed properties can give more insights on understanding the mechanical behavier of cells.

The microstructure of cytoskeleton exhibits some remarkable and desireable properties. This low-density network, which only has a few percent volume fraction, can rapidly change its morphology, modify its linear and nonlinear moduli, and exert controlled forces on its surroundings. Those features, if transplanted to the design of new material, would have revolutionary impacts on branches of engineering from biomedical to aerospace where the demands for drastic but reversible changes in shape and stiffness cannot be met by today's synthetic materials. For example, molulus-adaptability would provide a solution for the common bioengineering problem of stiffness mis-match of orthopedic and tissue implants. And a stiff, light-weighted carbon-nanotube-network material capable of large deformation would generate a new direction for design of adaptive aerospace structures.

1.1 Cytoskeletal Structure of Cells

The cytoskeleton is a cellular "scaffold" or "skeleton" contained within the cytoplasm and is present in all cells. Cytoskeleton is a structure that maintains cell's shape, protects the cell, enables cellular motion, and plays important roles in both intracellular transport and cellular division. The cytoskeleton determines, in large part, the morphology and mechanical properties of cells.

The cytoskeleton consists of three major classes of filaments: the cable-like actin filaments (Fig. 1.1(A)), the rope-like intermediate filaments (Fig. 1.1(B)), and the pipe-like, hollow microtubules(Fig. 1.1(C)). The filaments are accompanied by a large amount of accessory proteins which either crosslink filaments to each other or crosslink them to other cellular structures. The thickness of these three types of filaments are shown side by side in Fig. 1.1. Typically, the diameter of actin filaments is of 6 nm; intermediate filaments are slightly thicker with diameter around 10 nm; and microtubules have a hollow structure with outer diameter on the order of 25 nm. With the their length in the range of 1 to 1000 μm, these filaments are very slender. As for the cytoskeletal proteins which work as filament bonds, they usually have a molecular dimension on the order of 10nm, which is on the same order of filament's thickness.

The cytoskeletal filaments were initially identified by electron microscopy. Since then, the constituent proteins that made up the cytoskeletal filaments: actin, intermediate filament proteins, and tubulin have been chemically purified. Furthermore, the actin and tubulin proteins have been solved at atomic resolution. However, the structure of intermediate filaments is still uncertain. The chemical structure of the three types of filaments will be discussed in the following sections.

1.1.1 Actin Filaments

Actin filament is the major components of cytoskeleton. The actin family contains over a dozen classes of proteins and its building block is the actin monomer. An actin filament is consist of a one-start, left-handed helix of actin monomers. Fig. 1.2 shows its two-stranded

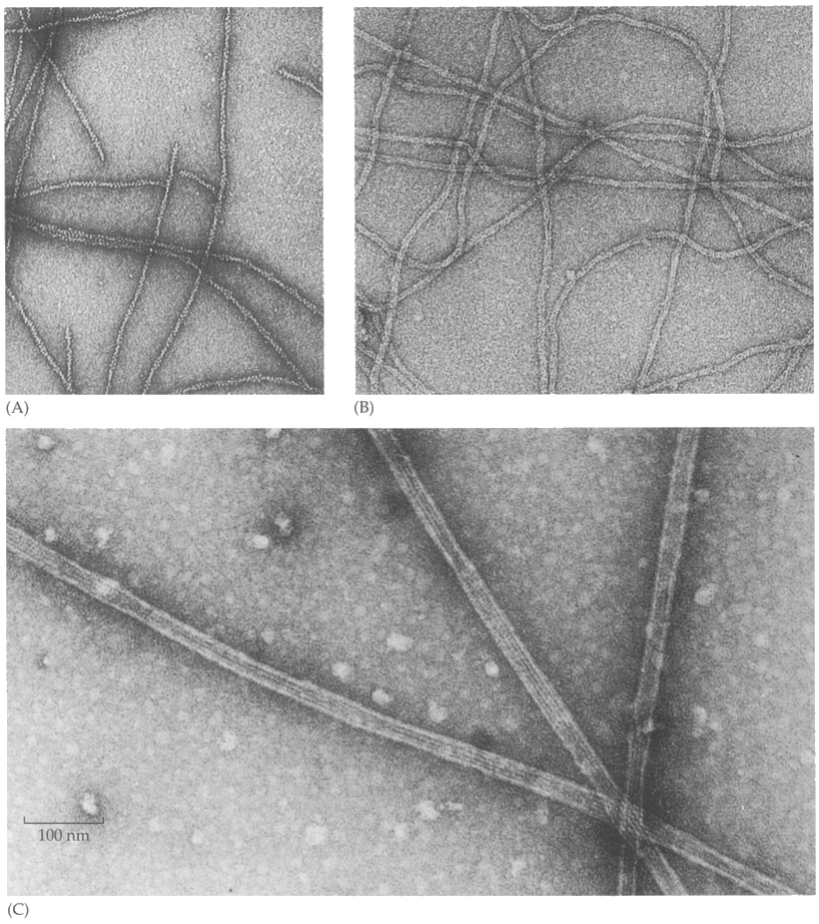

Figure 1.1: Electron micrographs of cytoskeletal filaments [1]

lattic structure(A) and atomic model(B). The full period of the filament is 72nm, which contains 26 subunits. Because rotation per monomer is large, and there is extensive monomer-monomer contact between alternate monomers, the actin filament is more appropriately viewed as a two-stranded, right-handed helix, with the so-called protofilaments strands.

Several experiments have been performed to evalute the actin filament's stiffness. A clever experiment on muscle fibers by Higuchi *et al.* [5] provides estimates of actin filament's longitudinal stiffness. Muscle fibers have banded appearance due to the repeating of structure unit, the sarcomere. The sarcomere consists of thin filaments (mainly actin filaments) and thick filaments. Higuchi *et al.* compared the stiffness of a muscle fiber at two different lengths, 1.8 μm and 2.4 μm. They used those lengths because only the thin filaments was stretched 0.6μm in that region, with all the other sarcomere parts unchanged in length. In

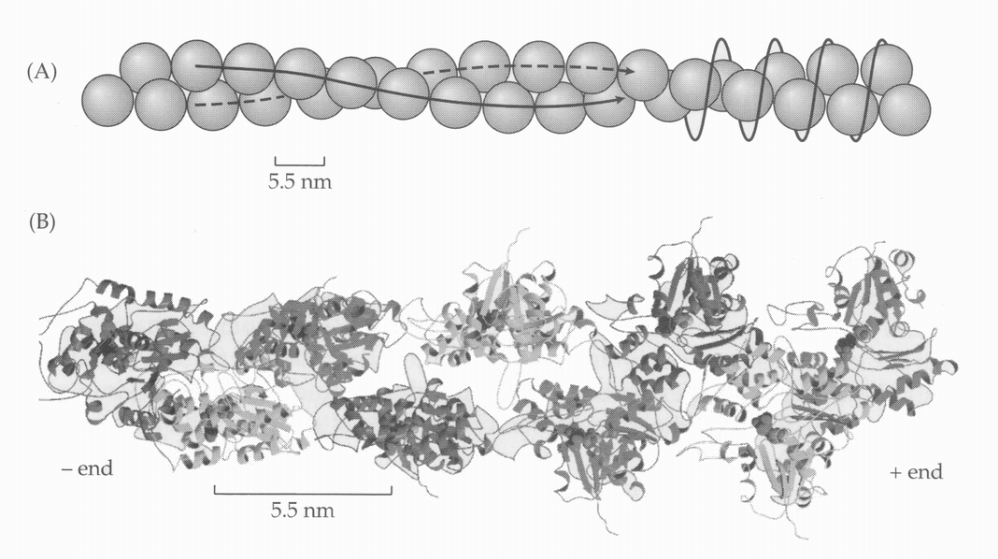

Figure 1.2: Structure of the actin filament [2]

this way, the only part withstands the pulling is the thin filament. The thin filament is about 1 μm long and with a cross section area of $1.05 \times 10^{-15} m^2$. From the experiment, an increase in tension of 50 kPa in the shorter muscle increases the length by 1.2 nm. They estimated the longitudinal stiffness of a 1 μm filament is 53 pN/nm. Since the thin filaments cross section area is about 23 nm^2, the Young's modulus can be calculated to be 2.3 GPa.

Another experiment performed by Howard and Hudspeth [6] tested the bending stiffness of stereocilia (a mechanosensing organelle of hair cells). Their results can also be used to estimate the Young's modulus of actin filaments, which are the main components of stereocilia. The experiment is on a hair bundle consisting of some stereocilia, each of which is composed of a cylindrical core of crosslinked actin filaments. A glass fiber is attached to the hair bundle and forces are applied onto the fiber to pivot the stereocilia. The bending stiffness attributed to the stereocilia is measured to be $\kappa = 600\mu$N/m. To find the Young's modulus of actin filament, a relation between the stereocilia and the actin filaments is needed. Consider a cantilever beam model for a stereocilium brought forward by Howard and Ashmore [7] as shown in Fig. 1.3. It has a base of radius a and length l. The distal region is much longer and more rigid than the base so its deformation is neglected. At the basal region, use the beam equation:

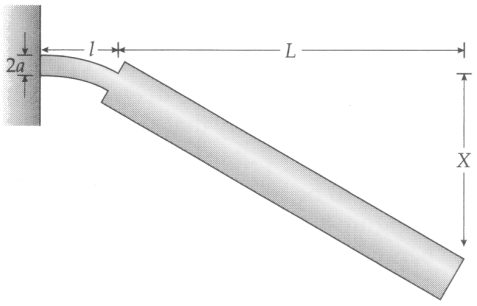

Figure 1.3: A cantilever beam model with a flexible base [1]

$$\frac{d^2y}{dx^2}(x) = \frac{M(x)}{E_bI_b} \cong \frac{FL}{E_bI_b} \tag{1.1}$$

where E_bI_b is the rigidity of the basal region. Since the distal region is rigid enough to neglect its deformation, the displacement X at the end can be calculated from

$$\frac{X}{L} = \frac{dy}{dx}(l) = \int_0^1 \frac{d^2y}{dx^2}dx = \frac{FLl}{E_bI_b} \tag{1.2}$$

After rearrangement, the bending stiffness can be represented as

$$\kappa = \frac{E_bI_b}{lL^2} \tag{1.3}$$

If the base is composed of n crosslinked filaments of radius r, then the filaments occupy a fraction $\gamma = n \cdot \frac{r^2}{a^2}$ of the basal cross section area. Then the flexural rigidity is

$$E_bI_b = \gamma E \cdot I_b = nEI\frac{r^2}{a^2} \tag{1.4}$$

where EI is the flexural rigidity of a single filament. If considering the number of stereocilia N, κ can be written as

$$\kappa = N\frac{nEI}{lL^2}\frac{a^2}{r^2} \tag{1.5}$$

From Howard and Hudspeth's experiment measurement, the stereocilia's bending stiffness κ is around $600\mu N/m$. The number of stereocilia N is about 50, number of filaments n is

around 30, the basal length l and radius a can be estimated to be around 1 μm and $50nm$. The area moment of inertia of a single actin filament is $I = A^2/4\pi$, where A is the filament's cross section area, and could be estimated to be around $19nm^2$. Plug in those values to the equation, and the Young's modulus E of actin filament can be calculated to as 1.6 GPa, which is in reasonable agreement with the 2.3 GPa predicted in the muscle experiment presented before.

1.1.2 Microtubules

Microtubules are made up from the $\alpha\beta$ tubulin heterodimer and there are five classes of proteins in the tubulin family. The lattice and atomic structures of the microtubule is shown in Fig. 1.4. The tubulin dimers associate with each other head-to-tail to form a protofilament. The protofilaments then associate latterally to form a sheet that closes to form the tube-like microtubule. Most cellular microtubules have 13 protofilaments and 3 starts. But microtubules are highly polymorphic in structure that some researchers have observed microtubules with as few as 8 protofilaments and as many as 19 protofilaments.

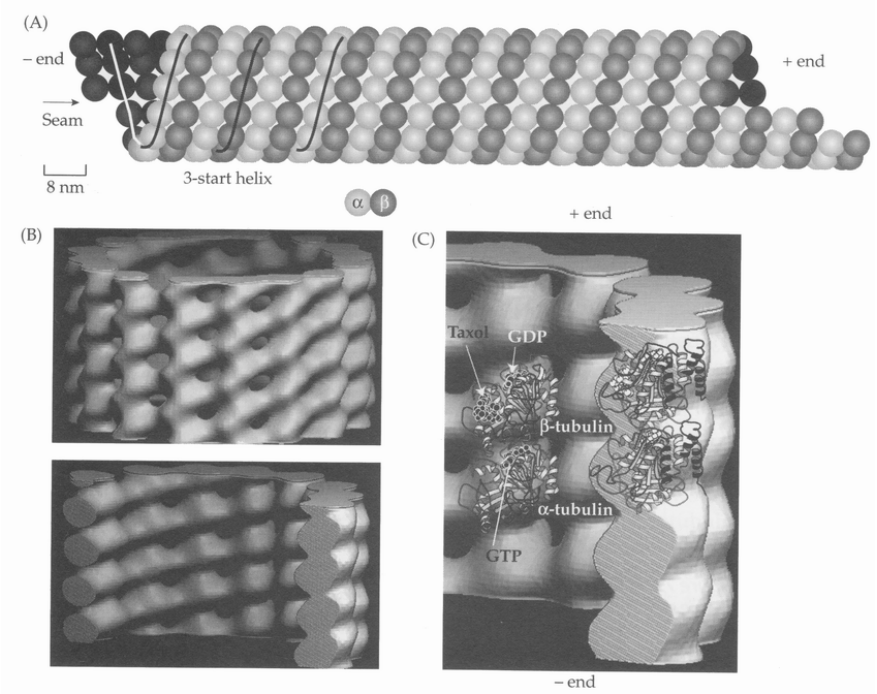

Figure 1.4: Structure of the microtubule [3]

Because of its hollow structure and relatively large diameter compared with other types of filaments, microtubules have a very large bending stiffness. Some experiments have been performed to determine the bending stiffness of microtubules. One experiment by Okuno [8] measures the flexural rigidity of sperm whose bending rigidity is mainly due to the stiffness of microtubules. They assume that in the most relaxed sperm there is no crosslinking between microtubules, and the flexural rigidity of a single microtubule is 20 to $30\times10^{-24}\mathrm{N}\cdot m^2$. Another experiment made by Gittes *et al.* [9] tests the rigidity of microtubules polymerized from purified brain tubulin. The flexural rigidity of those tested microtubules is about $26\times10^{-24}\mathrm{N}\cdot m^2$. From results of the above two experiments, the Young's modulus of microtubules can be estimated to be around 2.0 GPa, which is similar to that of the actin filaments. However, since microtubule's diameter is about 4 times as that of an actin filament, their bending stiffness then should differ by $4^4 = 256$ times. As a result, microtubule's bending stiffness is so stiff compared to actin filament, that it plays an important role in controlling cytoskeleton's overall response to mechanical loading.

1.1.3 Intermediate Filaments

The intermediate filament is made of the coiled-coil, a parallel dimer of alpha-helices. The alpha-helics are hydrophobic on one side and hydrophilic on the other side. So coiled coils are composed of alpha-helics whose hydrophobic surfaces are packed together to avoid exposure to solvent.

For now, the structural organization of the coiled-coil dimers in the intermediate filament is not known for sure, and it is possible that the arrangement differs between classes of filaments. One model is that homodimers form antiparallel tetramers, which associate head-to-tail to form a protofilament. And a pair of protofilaments forms a protofibril, and 4 protofibrils wrap around each other to form a 10nm filament with an organization like a piece of string. From this model, there will be 16 coiled-coils in each intermediate filaments, which is in agreement with a mass per unit length of 47kDa/nm for neurofilaments [10].

Because many materials composed of intermediate filament proteins are of commercial

interest (such as hair and wool), the mechanical properties of intermediate filament have been studied extensively. Intermediate filament has very different properties in dry and hydrated states. For example, when hair is fully hydrated, its longitudinal Young's modulus decreases only about 3-fold compared with that of dry hair, whereas its transverse Young's modulus decrease as much as 30-fold. The reason is that hydration softens the crosslinks between coiled-coils, allowing the intermediate filaments to shear, but the softening has very little effect on their longitudinal stiffness [1]. For the same reason, the flexural rigidity of hydrated intermediate filament is surprisingly low. In this sense, the intermediate filament behaves very similarly to rope when considering mechanical properties.

1.1.4 Crosslinks

Besides filaments and microtubules, there exist some other auxiliary proteins which are very important to the mechanics of cytoskeletal structure. Crosslink is a kind of actin binding protein that binds nearby filaments or microtubules to form a connected structure. For example, actin filaments must be tightly crosslinked together to resist bending forces. If they are not crosslinked, the stiffness could be less then 1% compared with crosslinked ones. Crosslinks are in large numbers that the mean distance between crosslinks can be as small as 1 μm, a distance much shorter than either the typical filament length or the thermal persistence length, which will be discussed in details in the following chapters.

1.1.5 Motors

Motor protein is another important auxiliary mini-filament protein for cytoskeleton. Motor proteins convert chemical energy derived from the hydrolysis of ATP into mechanical work used to drive cell motility. The widely accepted framework for understanding this chemo-mechanical transduction process is the rotating crossbridge model. The model contains two key ideas. First, the motor cycles between attached and detached states. Second, while attached, the motor undergoes a conformational change (a "kick" of order 1pN) that moves the load-bearing region of the motor in the direction along the filament. If recovery takes

place during the detached phase of the cycle, there will be a net displacement of the motor toward its next binding site on the filament [1].

1.2 Review of Mechanical Models of Cytoskeleton

The field of cell mechanics recently has undergone rapid development with particular attention to the rheology of the cytoskeleton and the reconstituted gels of some of the major cytoskeletal components: actin filaments, intermediate filaments, microtubules, and their crosslinking proteins. A wide range of computational models have been developed for cytoskeletal mechanics, ranging from finite-element based continuum models to actin filament based network models. Numerous experimental techniques have also been developed to quantify cytoskeletal mechanics, typically involving a mechanical perturbation of the cell in the form of either an imposed deformation or force and observation of the static and dynamic responses of the cell. These experimental measurements, along with new computational approaches, have given rise to several theories for describing the mechanics of cells, modeling the cytoskeleton as a elastic, viscoelastic, or poroviscoelastic continuum, or a tensegrity (tension integrity) network incorporating discrete structural elements bearing tension or compression [11]. The following sections will review those analytical and numerical cytoskeletal models.

1.2.1 Continuum Elastic or Viscoelastic Models

Cells can be modeled as continuum if the smallest length scale of interest is significantly larger than the dimensions of the microstructure. For example, if deformations are considered for a whole cell, the length scale of interest is several orders of magnitude larger than the distance between the cell's filaments, and as such a continuum description may be appropriate.

In essence, continuum mechanics is a coarse-graining approach that averages the contributions of the cytoskeleton's discrete filaments and microtubules and replaces them with the local microscopic stress-strain relationship with averaged constitutive laws that apply at macroscopic scale. Predictions of the continuum model, are only as good as the consti-

tutive law (stress-strain relation) on which they are based. This could range from simple linear elasticity model, nonlinear elasticity model, to viscoelastic model which can capture the deformation's time-dependent behavior.

Many researchers have successfully implemented finite-element based continuum model to capture the mechanical behavior of cells. The simulated results have also been compared with experimental data. For example, Drury and Dembo [12] simulated the deformation of neutrophils in micropipette aspiration using finite-element method, its mechanical behavior has been successfully captured by their viscoelastic model.

Continuum models of cell have proven useful in exploiting and interpreting results of a number of experiments. However, current models do not yet typically account for active biology: deformations and stresses experienced as a direct consequence of biochemical responses of the cell to mechanical load. But, by contrasting the predicted purely mechanical response to experimental observations, one could isolate phenomena involving active biology, such as cell contraction or migration, from the passive mechanical response of the cell [11].

Another limitation of continuum models is the lack of description of cytoskeletal filaments. As such, they are not applicable for situations where the length of interest is on the same order of the filaments, for example, the micromanipulations of the cell with a probe of the same size or smaller than the cytoskeletal mesh (0.1-1.0μm). This includes most AFM experiments. In addition, the continuum models exclude Brownian motions of the cytoskeleton due to thermal fluctuations, which have been shown to play a key role in cell motility [11].

1.2.2 Multiphasic Models

Most continuum models mentioned above have implemented constitutive models that assume cells consist of a single-phase material (fluid or solid). However, cells are highly complex structures whose properties depend on the interactions among the varying concentrations of water, charged or uncharged macromolecules, ions, and other molecular components contained within the cytoplasm [11]. These phenomena often cannot be described by single-phase models. To further investigate the mechanical behaviors of cells, a number of recent

studies have developed multiphasic constitutive laws to model the interactions among solid, fluid, and in some cases, ionic phases of cells. The goals of such studies have been to characterize the relative contributions of different physical mechanisms responsible for empirically observed phenomena such as cell viscoelasticity or volume change under mechanical or osmotic loading, and to account for the coupling of mechanical, chemical, and electrical events within living cells.

The multiphasic models consists of the momentum balance equations for both solid and liquid phases, and another momentum exchange equation (Darcy's law) relating solid and liquid phases. The equations can be solved numerically using finite element method. Baaijens *et al.* used a biphasic, viscoelastic finite-element mesh to model the micropipette aspiration test [13]. Comparison of the model to the experimentally measured response of chondrocytes to a step increase in aspiration pressure shows that the biphasic viscoelastic model could predict all aspects of the cell's creep response to a step aspiration.

Compared with single-phase continuum models, multiphasic models may provide a more realistic insight of the physics that govern cell's mechanical behavior. As most current multiphasic models are based on a continuum approach, the constitutive laws and parameters are essential to the prediction accuracy. That requires more experiments to be done to determine appropriate parameter values for the constitutive law.

1.2.3 Tensegrity-based Cytoskeletal Models

Tensegrity, the portmanteau of tensional integrity, was first introduced into architecture by R.B. Fuller in 1961 [14]. He defined tensegrity as a system through which structures are stabilized by loading members in pure tension or compression (like a camp tent etc). Ingber *et al.* [15] proposed a new cytoskeletal model based on tensegrity. The idea is that the cytoskeletal filaments carry preexisting tensile stress or prestress, and this prestress is partly balanced by compression-bearing microtubules and partly by forces that arise at cell adhesions to the extracellular matrix.

Many experimental data is consistent with the cellular tensegrity model. One of the

strongest evidences in support of the tensegrity model is the observed proportional relationship between cell stiffness and the cytoskeletal prestress. Experimental data also show that microtubules carry compressive stress, which balances a substantial portion of the prestress. Both of the above phenomenona are key features of tensegrity structure. So far, these two findings have provided the most convincing evidences in support of the cellular tensegrity model [11].

Stamenovic [16] developed a cable-and-strut model based on the tensegrity structure. The model consists of two elements: cable and strut. The tensile prestresses in cables are balanced by compression-supporting struts. Stamenovic derived an analytical equation for the shear modulus G of the cable-and-strut model as

$$G = 0.8(P - P_Q) + 0.2(BP + B_Q P_Q) \tag{1.6}$$

where P is the prestress carried by the cables and P_Q is the portion of P balanced by the struts, B=(dF/dL)/(F/L) is the nondimensional cable stiffness and B_Q=(dQ/dl)/(Q/l) is the nondimensional strut stiffness. The difference P-P_Q represents the portion of P transmitted to and balanced by the substrate. The relationship between G and P predicted by the above equation has been compared with experiments and it agrees very well with the data.

Tensegrity model is a model which takes account of the cytoskeletal micro-structure and its important property: the prestress. The current formulation of tensegrity model is simple, but can explain many of the key behaviors of cells.

1.2.4 Single Filament-based Models

MacKintosh *et al.* investigated the cytoskeleton network on microscopic scale [17]. They developed an analytical model using statistical mechanics for the bending and strecthing of a single filament. Based on this analytical model, they further analyzed filament network with binding crosslink proteins. The response of the network to macroscopic strains and stresses involves two distinct single-filament responses: bending and stretching. Models based on both of these effects have been proposed and analyzed. In the case of uniform shear, if only

rotation and stretching of individual filaments are possible, it is so-called affine network, in which the macroscopic strain falls uniformly across the whole network. In contrast, bending-dominated network involves non-affine deformations, in which the state of strain varies from one region to another within the network. Head *et al.* investigated the cytoskeletal filament network and claim that the affine or non-affine behaviors depend on filament length and crosslink concentration. Non-affine behavior is expected either at low concentrations or for short filaments, while the deformation is increasingly affine at high concentration or for long filaments [18, 19]. The details of the affine to non-affine transition, and the important mechanical property of cytoskeleton, *semiflexibility*, will be discussed in next section.

1.3 Semiflexible Networks

Cytoskeleton, which is essentially a type of biopolymer, can be studied as a system of crosslinked networks of rather stiff one-dimensional filaments. In networks where the filaments are sufficiently stiff in response to bending and crosslinked to each other at a high enough density, the thermal persistence length of the filaments becomes longer than the mean distance between crosslinks along a typical filament, which can then store elastic energy both in bending and stretching deformations. Systems conforming to this ordering of length scales may be termed *semiflexible networks* to distinguish them from the more thoroughly studied gels of flexible polymers for which rubber elasticity theory may be applied [20]. For the purpose of designing advanced structural materials, stiff synthetic polymers and even carbon nanotubes are attractive examples of filaments that may be used to form semiflexible networks [21, 22]. However, the most ubiquitous example is the cytoskeleton. Cytoskeleton, which is composed primarily of the filamentous protein aggregate F-actin, pervades much of the extra-nuclear cellular interior and is simultaneously the principal source of cellular mechanics and force generation [23–27]. In addition to containing a host of molecular motors (*e.g.*, myosin) and a plethora of F-actin crosslinking and bundling proteins, the chemically complex F-actin network of the cytoskeleton is pierced by a number of microtubules. These microtubules are even more highly incompliant mechanically, having a bending stiffness approximately 250 times larger than the F-actin filaments making up the network in which

they are embedded. Understanding the mechanical effect of these semiflexible networks is the main focus of this dissertation. For the purpose of this work, the complex chemical microstructure of the filaments is neglected. These macromolecular aggregates can be treated then as elastic beams when considering the collective mechanics of a gel or network formed by crosslinking them.

Particularly in the case of F-actin it is possible to produce permanently [28–30] or otherwise [29,31–33] crosslinked networks in which the mean distance between the crosslinks is significantly shorter than the thermal persistence length of the constituent filaments. For example, in the work of [29], F-actin filaments were crosslinked into a network having a mean spacing between crosslinks on the order of 2μm, while the thermal persistence length ℓ_P of these filaments is about an order of magnitude larger. Such systems can be thought of as highly simplified *in vitro* models of the cytoskeleton, without stiff microtubules, active molecular motors, and other constituents.

The mechanical response of these networks deviates from the predictions of traditional rubber elasticity theory, applicable to gels of flexible polymers. The underlying reasons are clear. Flexible polymer networks are composed of filaments whose thermal persistence length is typically much shorter than the mean distance between crosslinks on a given filament. Each polymer acts as a random walk and, under imposed strain, stores elastic free energy (entropically) in response to only the change in the separation between consecutive crosslinks along the chain. There is no bending energy cost. Semiflexible filaments, on the other hand, can store elastic energy by bending on scales comparable to or larger than the mean distance between crosslinks. Under uniformly applied shear strain, the sample, when deforming affinely (as in the expected minimum energy configuration required by stress balance for uniform density), should not store any energy in these bending modes. This means that, with the appropriate modification of the single filament force extension curve, one should be able to understand the linear elastic properties of a semiflexible network [34]. For sufficiently sparse networks, however, the assumption of affine deformation breaks down at small and intermediate length scales that are typically longer than both the mean distance between crosslinks and even the length of the filaments. In such nonaffinely deforming net-

works, elastic energy energy is stored almost entirely in the bending of filaments. Previous work [35–39] has shown that, as a function of increasing network density or filament bending stiffness, semiflexible networks admit a sharp cross-over from a bending dominated elastically compliant regime, which sets in at network densities above the rigidity percolation transition [40], to stiffer networks where elastic strain energy is stored primarily in the stretching of filaments. Moreover, under uniformly applied strain at the boundaries, the geometry of the deformation field in the softer, bending dominated regime is spatially heterogeneous (*i.e.*, non-affine) and shows large deviations from the affine deformation prediction of continuum elasticity theory [41]. This cross-over is controlled by the ratio of the filament length L to the so-called non-affinity length λ, which is a function of the network density parameterized by the mean distance between cross-links along a filament as well as the bending and stretching moduli of these constituent filaments.

Understanding the mechanics of even simple semiflexible networks has proven to be difficult. For random statistically isotropic networks of this type, their collective elastic properties should depend only on the mechanics of the individual filaments and the network density. In more complex systems, e.g., those exhibiting broken rotational symmetries [42], composites having multiple filament types [43,44], or elastically compliant crosslinks [45–47], other relevant variables are present. This dissertation discusses the role of polydispersity in random and isotropic networks of mechanically identical semiflexible filaments in Chapter 3, and polydispersity in isotrpic networks of mechanically heterogeneous filaments in Chapter 4, then network with anisotropic filament orientations is discussed in Chapter 5. While all these chapters are focused on static responses of the system, the frequency dependent rheology [48–52] and especially living cells [53–59] have been a very interesting topic and the focus of much attention in the research of semiflexible filament network systems. Chapter 6 of this dissertation discusses the rate dependent rheology of the system.

CHAPTER 2

Numerical Models of Cytoskeletal Networks

To understand the multi-scale mechanical behavior of semiflexible cytoskeletal networks, a numerical model which includes stretchable/bendable filaments and crosslinks is developed. Filaments are placed onto a square box with random orientation and position. The density of the network is controlled by the total number of filaments and size of the box. To facilitate finite element method, each filament is discretized into some small segments and modelled as beam elements with both streching and bending degree of freedom. Wherever two filaments cross with each other, a crosslink is placed at their intersection. For permanent crosslinks, rigid pins are used to model the crosslinks and they constrain the relative displacements between the two filaments while allowing free rotation; for labile crosslinks, stiff springs with finite stiffness are used to model the crosslinks such that crosslinks may be removed from or added to the network during simulation. Periodic Lees-Edwards boundary conditions are used at the four edges of the box generating an infinitely large network to remove the boundary effect. The energy and force equations for an element will be derived in the following sections.

2.1 Elastic Energy and Filament Discretization

The elastic energy of each filament is composed of bending and stretching components. For bending energy, we apply Bernoulli-Euler beam theory to the filament that the bending energy is a quadratic function of the filament's curvature. For stretching, we have two options: (a) to assume a Hookean (linear) stress strain relation, or (b) to coarse-grain the effects of short-length-scale fluctuations and adopt a nonlinear entropic elasticity model for the stretch energy.

2.1.1 Bending Energy

In the limit of continuum, Bernoulli-Euler beam theory, the bending energy of an initially straight beam is given as

$$E_{\text{bend}} = \int_L \frac{\kappa}{2}\Big(\frac{1}{R}\Big)^2 ds \tag{2.1}$$

where R is the radius of curvature along the filament contour L parameterized by arclength s, and κ is the bending modulus. Assume the configuration of filament could be described by a position map $\vec{x}(s)$ of arclength s, such that the tangent to the curve of filament is

$$\hat{n}(s) = \frac{\partial}{\partial s}\vec{x}(s) \equiv \vec{x}_{,s}(s) \tag{2.2}$$

from which the curvature can be computed as

$$1/R = |\hat{n}_{,s}| = |\vec{x}_{,ss}|. \tag{2.3}$$

To model the filament with finite degrees of freedom, filament is discretized into a set of $(N-1)$ straight beam segments (elements) L_n

$$L = \bigcup_{n=1}^{N-1} L_n \tag{2.4}$$

with each segment linearly interpolating the positon between two adjacent nodes $\vec{x}_n$ and $\vec{x}_{n+1}$, such that the tangent vector for segment L_n is

$$\hat{n}_n = \frac{\vec{x}_{n+1} - \vec{x}_n}{\ell_n} \tag{2.5}$$

where ℓ_n is segment length calculated from

$$\ell_n = |\vec{x}_{n+1} - \vec{x}_n|. \tag{2.6}$$

Since it's assumed that each segment is straight, all the bending energy is only associated with the nodes connecting those straight segments. Assuming the straight segments L_{n-1} and L_n represents a filament contour arc passing through nodes $(n-1)$,n, and $(n+1)$, the curvature at node n can then be calculated from curvature's definition as

$$1/R_n = \frac{\arccos\left(\hat{n}_{n-1} \cdot \hat{n}_n\right)}{\ell}.$$

where ℓ is the average segment length which can be simply calculated as $\ell = (\ell_n + \ell_{n+1})/2$. Now the bending energy associated with node n is

$$E^n_{\text{bend}} = \frac{\kappa}{2}(1/R_n)^2\ell = \frac{k_{\text{bend}}}{2}\arccos^2(\hat{n}_{n-1}\cdot\hat{n}_n)$$

where k_{bend} is the bending stiffness which is defined as $k_{\text{bend}} \equiv \kappa/\ell$. Writing the nodal bending energy E^n_{bend} in terms of the nodal positions $\vec{x}_{n-1}$, $\vec{x}_n$, and $\vec{x}_{n+1}$ gives

$$E^n_{\text{bend}} = \frac{k_{\text{bend}}}{2}\arccos^2\left(\frac{\vec{x}_n - \vec{x}_{n-1}}{|\vec{x}_n - \vec{x}_{n-1}|}\cdot\frac{\vec{x}_{n+1} - \vec{x}_n}{|\vec{x}_{n+1} - \vec{x}_n|}\right)$$

from which the following derivatives, i.e., nodal forces, can be computed as follows

$$\begin{aligned}
\vec{F}_{n-1} = \frac{\partial E^n_{\text{bend}}}{\partial \vec{x}_{n-1}} &= \frac{k_{\text{bend}}\arccos(\hat{n}_{n-1}\cdot\hat{n}_n)}{\ell_{n-1}\sqrt{1-(\hat{n}_{n-1}\cdot\hat{n}_n)^2}}[\hat{n}_n - (\hat{n}_n\cdot\hat{n}_{n-1})\hat{n}_{n-1}] \\
\vec{F}_{n+1} = \frac{\partial E^n_{\text{bend}}}{\partial \vec{x}_{n+1}} &= \frac{k_{\text{bend}}\arccos(\hat{n}_{n-1}\cdot\hat{n}_n)}{\ell_{n}\sqrt{1-(\hat{n}_{n-1}\cdot\hat{n}_n)^2}}[(\hat{n}_n\cdot\hat{n}_{n-1})\hat{n}_n - \hat{n}_{n-1}] \\
\vec{F}_{n} = \frac{\partial E^n_{\text{bend}}}{\partial \vec{x}_{n}} &= -\frac{\partial E^n_{\text{bend}}}{\partial x_{n-1}} - \frac{\partial E^n_{\text{bend}}}{\partial x_{n+1}}.
\end{aligned}$$

Although continuum mechanics is applied in this research, thermal forces play an important role in the cytoskeletal filament network such that relating the statistical, microscale thermal quantities of the filament with macroscale, continuum mechanics quantities is imperative. The following derivation relates filament's macroscale bending modulus κ with its microscale property: the *persistance length* L_p. The relation between κ and L_p is

$$\kappa = L_p k_B T. \tag{2.7}$$

where k_B is the Boltzmann constant and T is the absolute temperature. The persistance length, L_p is an important parameter describing a filament's resistance to thermal forces. It is defined as

$$\langle\cos(\theta(s) - \theta(0))\rangle = \exp\left(-\frac{s}{2L_p}\right) \tag{2.8}$$

where $\langle\rangle$ means average over time, and θ is the angle between the filament's tangential

direction and horizontal direction. Let $f = \langle \cos(\theta(s)) \rangle$, then

$$\begin{aligned}
\frac{df}{ds}\Delta s &\approx f(s+\Delta s) - f(s) \\
&= \langle \cos(\theta(s+\Delta s)) - \cos(\theta(s)) \rangle \\
&= \langle \cos(\theta(s+\Delta s) - \theta(s) + \theta(s)) - \cos(\theta(s)) \rangle \\
&= \langle \cos(\Delta\theta + \theta(s)) \rangle - \langle \cos(\theta(s)) \rangle \\
&= \langle \cos(\theta)\cos(\Delta\theta) - \sin(\theta)\sin(\Delta\theta) \rangle - \langle \cos(\theta) \rangle
\end{aligned}$$

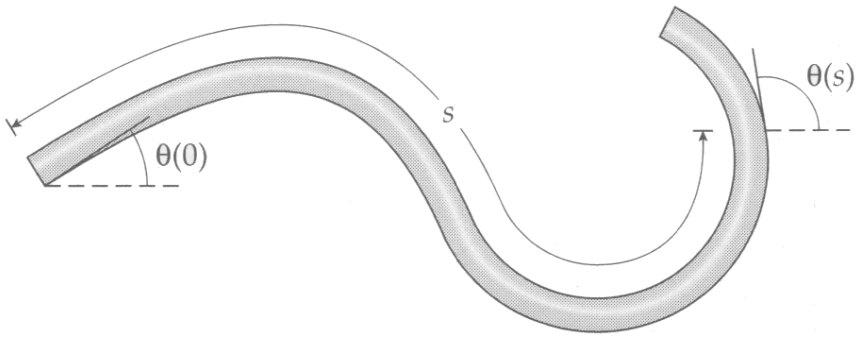

Figure 2.1: Thermal bending of a slender rod [1]

Because the thermal force on segment $(s, s+\Delta s)$ are independent of the thermal force on segment $(0, s)$, the tangent angels $\theta(s)$ and Δs are statistically independent. Thus it

$$\begin{aligned}
\frac{df}{ds}\Delta s &\approx \langle \cos(\theta) \rangle \cdot \langle \cos(\Delta\theta) \rangle - \langle \sin(\theta) \rangle \cdot \langle \sin(\Delta\theta) \rangle - \langle \cos(\theta) \rangle \\
&= \langle \cos(\theta) \rangle \cdot [\langle \cos(\Delta\theta) \rangle - 1]
\end{aligned} \tag{2.9}$$

Thus

$$\begin{aligned}
\frac{df}{ds} &\approx \frac{\langle \cos(\Delta\theta) - 1 \rangle}{\Delta s} f(s) \\
&\approx -\frac{1}{2}\left\langle \frac{\Delta\theta^2}{\Delta s} \right\rangle f(s) \\
&= -\frac{1}{2}\left\langle (\frac{\Delta\theta}{\Delta s})^2 \Delta s \right\rangle f(s) \\
&= -\frac{\langle \Delta U \rangle}{EI} f(s) \\
&= -\frac{1}{2}\frac{k_B T}{EI} f(s)
\end{aligned} \tag{2.10}$$

where U is energy density, whose time average can be proved to be $\frac{1}{2}k_BT$ using statistical mechanics theory. The proof can be found from any statistical mechanics book and will be skipped here; E is the Young's modulus of filament, and I is the area moment of inertia of filament's cross section. Solving it then gives

$$\langle \cos(\theta(s) - \theta(0)) \rangle = \exp(-\frac{kTs}{2EI}) \tag{2.11}$$

Compare Eq. 2.11 with Eq. 2.8 and note in continuum mechanics $\kappa = EI$, one can get Eq. 2.7.

2.1.2 Stretching Energy

Cytoskeleton in cells is always under thermal fluctuation. Because of their different persistence length, actin filaments and microtubules act much differently under thermal forces. For actin filament, which has a typical persistence length of 17 μm that is on the same order of its contour length, its stretching energy is stored in thermal (entropic) form; for microtubule, whose persistence length is around 2 mm that is much longer than its own length, stores its energy mostly in athermal form. As a result, two different models have been used to model the actin filaments and microtubules. For microtubules, since they are athermal, linear elastic model can be applied to them. For actin filaments, if small stretching deformation is assumed, the linearized stretching modulus from thermal fluctuation of the filament can be treated as constant for the stretching, and linear elastic model can still be applied in this case; for large deformation, an entropic elastic model is derived using statistical mechanics. The following sections introduce both of these models.

2.1.2.1 Linear Hookean elasticity

In the limit of continuum, the stretching energy of a beam is given as

$$E_{\text{stretch}} = \int_L \frac{\mu}{2} \left| \frac{d\vec{x}}{ds} \right|^2 ds \tag{2.12}$$

where μ is the stretching modulus and $\vec{x}$ is the position of filament's cross-section after deformation. If small deformation is assumed, we may neglect the continuum limit and simply

treat each segment as a linear Hookean spring for stretching. Define the stretching stiffness as $k_{\text{stretch}} \equiv \mu / L_n$, where L_n is the unstretched length of a segment, then its stretching energy can be written as

$$E^n_{\text{stretch}} = \frac{k_{\text{stretch}}}{2}(\ell_n - L_n)^2, \quad n = 1, \ldots, N-1 \tag{2.13}$$

where segment length ℓ_n is defined as above. Assume the reference positions of the segment's nodes are $\vec{x}_n$ and $\vec{x}_{n+1}$, and the current positions are $\vec{X}_n$ and $\vec{X}_{n+1}$. From this definition it is straightforward to derive the internal "spring" forces due to segment strecthing of the two nodes as follows

$$\vec{F}_n = \frac{\partial E^n_{\text{stretch}}}{\partial \vec{x}_n} = -k_{\text{stretch}} \left(|\vec{x}_{n+1} - \vec{x}_n| - |\vec{X}_{n+1} - \vec{X}_n| \right) \hat{n}_n \tag{2.14}$$

$$\vec{F}_{n+1} = \frac{\partial E^n_{\text{stretch}}}{\partial \vec{x}_{n+1}} = k_{\text{stretch}} \left(|\vec{x}_{n+1} - \vec{x}_n| - |\vec{X}_{n+1} - \vec{X}_n| \right) \hat{n}_n \tag{2.15}$$

where $\hat{n}_n$ is the tangent vector of the segment as defined before.

2.1.2.2 Entropic elasticity

Actin filament and many other semiflexible networks are essentially highly non-linear materials. In constrast with the linear spring model, a more thorough treatment of the actin filament's elastic properties involves taking into account the so-called *entropic elasticity* of the filaments; that is, the resistance of the filaments to bending/stretching due to entropy. As an example of this, consider a filament of arclength L_{arc}. At finite temperature T, it will deform and wiggle due to thermal noise, resulting in a mean end-to-end filament distance of $L_0(L_{\text{arc}})$. If one tries to stretch the filament beyond this length (thus lowering its elastic energy), one will encounter resistance due to entropy.

MacKintosh *et. al* first discussed this feature of actin filaments [17] and derived a transcendental equation for the end-to-end filament distance L as a function of applied tension τ (or, as in the present case, the tension in the filament as a function of end-to-end distance). This relation is given by

$$L_{\text{arc}} - L = \frac{k_B T}{2\tau(L)} \left[\sqrt{\frac{\tau(L)}{\kappa}}\, L \coth\left(\sqrt{\frac{\tau(L)}{\kappa}}\, L \right) - 1 \right], \tag{2.16}$$

where κ is the bending modulus of the filament. It is easier to work in dimensionless units; dividing each side by the persistence length $L_p \equiv \kappa/k_BT$ leads to the following equation for the dimensionless variable $x \equiv L/L_p$:

$$x_{\text{arc}} - x = \frac{1}{2\phi(x)} \left[x\sqrt{\phi(x)} \coth\left(x\sqrt{\phi(x)}\right) - 1 \right], \tag{2.17}$$

where $\phi(x) \equiv \tau(L_p x)\, {L_p}^2/\kappa$. The function $\phi(x)$ has a few important features of note: it diverges like $(x_{\text{arc}}-x)^{-2}$ as $x \to x_{\text{arc}}$; it diverges like x^{-2} as $x \to 0$; and it goes as $a(x-x_0)$ near the equilibrium length x_0. Thus, so long as the filaments are subject to small deformations, the Hookean spring approximation of the previous section should be sufficient. However, if the nonlinear behavior of the gel is of interest and deformation is large enough that the small deformation assumption no longer holds, it's needed to go beyond this approximation and calculate the tension using the above equation.

Since it is quite computationally inefficient to solve this transcendental equation for each rod at each simulation time step, it is necessary to find a proper fitting function for $\phi(x)$ (and thus for $\tau(L)$). For a given value of x_{arc} (and thus x_0), there exists a Taylor expansion for $\phi(x)$ around x_0 given by

$$\phi(x) = \sum_{n=1}^{\infty} \frac{c_n(x_0)}{n!} (x - x_0)^n. \tag{2.18}$$

Due to the singularities in $\phi(x)$, this series converges very slowly; a Padé approximant works much better, but must be taken to high order to work for large tension. We have found two approaches to fit this function: the first is an ad hoc approach inspired by Padé which involves using two different fitting functions, one for $x < x_0$ and one for $x \geq x_0$. The fit function ϕ_{fit} for $x \geq x_0$ has the form

$$\phi_{\text{fit}}(x) = \frac{1}{(x_{\text{arc}} - x)^2} \sum_{n=1}^{N} \frac{a_n}{n!} (x - x_0)^n, \tag{2.19}$$

where the coefficients a_n are determined by matching the first N derivatives of $\phi_{\text{fit}}(x)$ with the first N derivatives of $\phi(x)$ at $x = x_0$.

For $x < x_0$ the fit function has the form

$$\phi_{\text{fit}}(x) = \frac{\pi^2}{x^2} \left[\frac{P_m(x)}{Q_n(x)} - 1 \right], \tag{2.20}$$

where $P_m(x)$ and $Q_n(x)$ are polynomials of order m and n, respectively. Both $P_m(x)$ and $Q_n(x)$ are equal to 1 at $x = x_0$. The above equation can be rearranged to give

$$\frac{P_m(x)}{Q_n(x)} = 1 + \frac{x^2}{\pi^2}\phi_{\text{fit}}(x); \tag{2.21}$$

if we force the first $N = m+n$ derivatives of $\phi_{\text{fit}}(x)$ to match those of $\phi(x)$, then $P_m(x)/Q_n(x)$ is simply the Padé approximant to the function $1 + x^2\phi(x)/\pi^2$.

In order to determine the coefficients in these functions for a given m and n, we used the usual method of determining Padé coefficients given a Taylor series. We found that the $m = 3$, $n = 4$ Padé approximant worked best to fit $\phi(x)$ over the full range of x values [1]. For both $x \geq x_0$, the energy of the filament was determined by simply integrating the fit function; for $x < x_0$, the energy of the filament was determined by finding a Padé approximant to $1 - x\phi_{\text{fit}}(x)/\pi^2$.

The second approach involves using a fit function of the form

$$\phi_{\text{fit}}(x) = \sum_{n=1}^{N} \frac{a_n}{n!}(x - x_0)^n + \frac{b(x - x_0)}{(x_{\text{arc}} - x)^2} \tag{2.22}$$

and matching the first N derivatives of $\phi(x)$ (b is fixed by matching the constant in front of the leading divergence of $\phi(x)$). This function provides a good fit for tensile load, but not for compressive load.

2.1.3 Single Filament Mechanics

The mechanics of individual filament is modelled using classical, Bernoulli-Euler linear elastic continuum beam theory and both bending and stretching of the filament are considered. For a filament with undeformed length L, its total strain energy after deformation can be represented as

$$E_{\text{fil}} = \int_L ds \left[\frac{\mu}{2}\left|\frac{d\vec{x}}{ds}\right|^2 + \frac{\kappa}{2}\left(\frac{d\theta}{ds}\right)^2\right], \tag{2.23}$$

where s is the arc-length along undeformed filament, $\vec{x}$ is the position of filament's cross-section after deformation, and θ is the angle of rotation of the cross-section between the

[1] It should be noted that only the first five terms of the Taylor series are used for $\phi(x)$, rather than the first seven. The multiplication by x^2 allowed for a Padé approximant of order $m + n = 7$ to be used despite only using the first five terms of the Taylor expansion.

undeformed, and deformed configurations. To compute the strain energy of a filament numerically, each filament are discretized into piecewise straight segments as discussed above. So a discrete version of the strain energy of a single filament is just the summation of bending and stretching energies over all segments and adjacent segment pairs as

$$E_{\text{fil}} = \sum_{\text{segments}} E_{\text{stretch}} + \sum_{\text{angles}} E_{\text{bend}} \tag{2.24}$$

$$= \frac{\mu}{2} \sum_{n=1}^{N-1} \frac{(\ell_n - L_n)^2}{L_n} + \frac{\kappa}{2} \sum_{n=2}^{N-1} \frac{\beta_n^2}{\ell}, \tag{2.25}$$

where the L_n and ℓ_n represent the undeformed/rest length and deformed length of the segments, β represents the angle between two adjacent segments, and the ℓ parameter is the average of the rest lengths of two segments adjoined at an angle spring, i.e. $\ell = (\ell_n + \ell_{n+1})/2$. Note that the total number of nodes on a filament is assumed to be N, so the number of segments is $(N-1)$ and number of angles is $(N-2)$.

The relative stiffness of single filament bending and stretching modes is described by the bending length $\ell_b = \sqrt{\kappa/\mu}$. For a zero-temperature prismatic rod having constant cross-sectional and elastic properties along its length, Bernoulli-Euler continuum beam theory gives the familiar results $\mu = E\mathcal{A}$ and $\kappa = EI$, where E is the 3-D Youngs modulus, and $\mathcal{A}$ and I are the area and area-moment of inertia of the cross section, such that $\ell_b = \sqrt{I/\mathcal{A}}$ is of the order of filament diameter. We note that for semiflexible filaments such as F-actin at room temperature, the effective longitudinal compliance can be significantly larger than the zero-temperature value. In this a case tensile loading extends the filament primarily through the pulling out of thermally generated undulations [34]. This leads to an effective μ that is smaller than the stretching rigidity $E\mathcal{A}$ of the underlying proteins, and thus a larger value of ℓ_b.

2.1.4 Crosslinks

Two models are developed to implement the crosslinks which bond filaments at their intersections. The first model uses linear springs with high stiffness as crosslinks to bond the two segments at the intersection of two filaments. The energy in a bonding crosslink can be

calculated from

$$E_{\text{cross}} = \frac{1}{2} k_c (x_c - x_{c0})^2 \tag{2.26}$$

where x_c and x_{c0} are the deformed (current) and undeformed (initial) lengths of crosslink, and k_c is the stiffness of crosslink. The initial state of the spring-like crosslinks is always at the intersection of two filaments during network model set-up, thus its initial length x_{c0} is essentially zero within a tolerance as small as the computer machine precision. Thus, this guarantees that the network is set up to a zero energy state. The spring-like crosslink is useful when labile crosslinks are modeled in Chapter 6, where crosslinks have to be attached and detached during each time step. Another advantage of this type of crosslink is that filaments can be discretized uniformly because the crosslinks are placed onto segments and they don't have any requirement on node positions, which is different than the second model, as discussed as follows.

The second model use node constraints to tie two intersecting filaments. As a result, nodes have to be generated for each of the filaments where they intersect. One of the nodes is so-called master node and the other is called slave node, which moves with master node and is not an active degree of freedom. The constraint crosslink's advantage over spring-like crosslink is that there's no need to calculate the crosslink energy and force and only the master node's degree of freedom will be put into solver, which saves computation time. The major disadvantage of this type of crosslink is that filaments can not be discretized uniformly (adaptive meshing has to be implemented) and segments may be too short due to too-close crosslinks which can cause convergence diffculties to the numerical solver. the tie has infinite stiffness and no energy contribution. Special care has been taken to get rid of those too-short segments by eliminating one of every two too-close crosslink constraints.

2.2 Network Model Setup

Using discretized filament as stated above, a two-dimensional network composed of thousands of filaments is generated and modelled. Each filament is placed with randomly chosen position and orientation in a square box of width W and area $A = W^2$. Wherever two

filaments cross with each other, a crosslink (spring-like or rigid constraint, depending on applications) is placed at their intersection. Each crosslink constrains the relative displacements of two filaments while allowing free rotation. Spring-like crosslink will contribute to be the network's total energy, while rigid constraint does not. To avoid the effect of finite boundary and also save the computational time of simulating a too large network, Lees-Edwards periodic boundary condition [60] is applied at the four edges of the square box. This effectively change the simulation of network in a finite square box to the simulation of network in an infinite two-dimensional plane with periodic patterns. Shear loading is applied on the top and bottom boundaries of the network with opposite directions. An example network demonstrating the model for a bimodal length distribution is shown in Fig. 2.2.

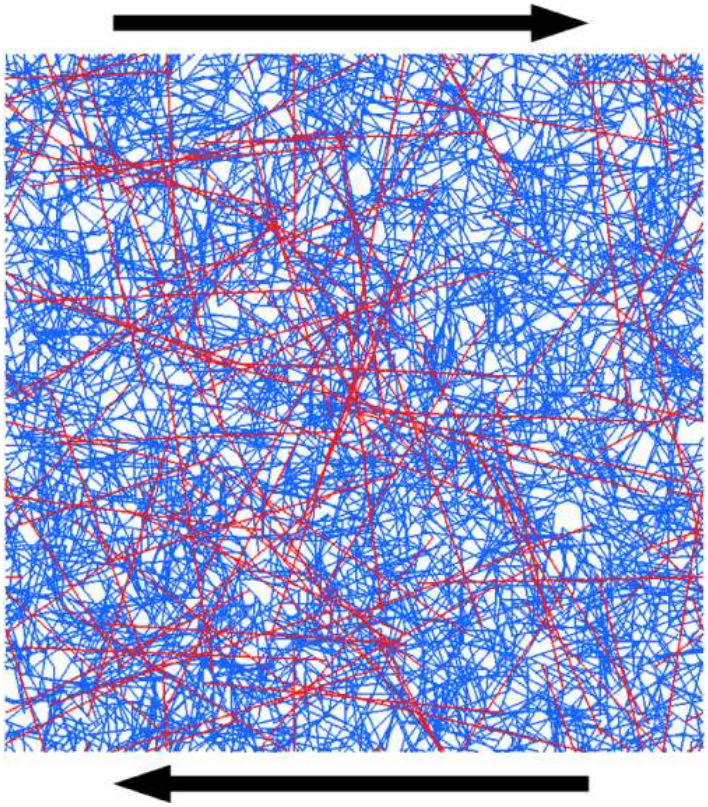

Figure 2.2: A typical simulated bimodal length polydisperse network, with short filaments shown in blue and long filaments in red. Arrows show the shearing directions imposed on the top and bottom periodic boundaries

Both force control loading and shear control loading have been developed for the network.

The total strain energy of a network can be calculated from summing up all the strain energy in filaments, crosslinks (if spring-like crosslinks are used), and minus the work done by external force (if force control is applied). Static equilibrium of the network is obtained by minimizing the total energy using an iterative quasi-Newton optimization code L-BFGS-B [61, 62].

CHAPTER 3

Geometric Polydispersity: Bimodal and Exponential Length Distributions

3.1 Introduction

Previous experimental and theoretical work has shown that decreasing crosslink density in monodisperse semiflexible networks leads to a sharp affine to nonaffine (NA/A) crossover from a high-density affine regime to a nonaffine one, characterized by bending-dominant, nonaffine deformation [30, 31, 35–39, 63–69]. Mechanically, nonaffine networks are several orders of magnitude more compliant than is predicted by continuum linear elasticity for a uniform, affine strain field; in contrast, affine networks can achieve more than 90% of the stiffness predicted by continuum elasticity. Geometrically, when subjected to uniform strains along their boundaries, nonaffine networks have a heterogeneous deformation field, where denser regions in the network tend undergo local rigid body motions compelling sparser "connector" regions to experience large bending deformations; whereas affine networks follow a homogeneous strain field compatible with the boundary conditions and consistent with continuum elasticity theory. Energetically, because of the sparsely connected regions with larger distance between crosslinks, filaments in nonaffine network tend to bend more than stretch; however, in affine networks, stretching energy accounts for as much as 99% of the total energy.

This chapter talks about the linear elastic response of semiflexible networks with two classes of *length polydispersity*: bidisperse i.e. short and long, and exponential length distributions. The purpose of doing so is two-fold. First, to better connect the current state of the theory, chiefly focussed on monodisperse networks, to both *in vitro* experiments on typically

polydisperse F-actin [70–72] and eventually to studies of the elastic properties of living cells [73]. These experimental systems are generally highly polydisperse; this work seeks to understand the implications of that type of disorder on the affine to nonaffine crossover. There is a clear reason for doing so: in previous work it has been shown that the crossover can be understood in terms of a single control parameter, the ratio of the length of a filament L to the nonaffinity length, λ. While this provides a universal framework for understanding monodisperse systems, it remains to be seen whether the crossover in polydisperse networks can be characterized in an analogous manner. Second, a basic question related to the engineering of optimal semiflexible networks is proposed. One desirable feature of these systems is that they make fairly rigid solids at low volume fractions. For example, the cytoskeleton occupies less than one percent of the cell's volume but confers its mechanical rigidity. Assuming that one could control the length distribution of the semiflexible filaments, how can one chose the optimal length distribution to maximize the rigidity of the network at fixed mass density? In this work, the contribution to the network's collective rigidity per unit mass mass density is termed as its mechanical efficiency and what network design principles maximize this quantity is discussed in this chapter. These questions about the mechanics of semiflexible networks with length polydispersity are addressed by numerical simulation using two-dimensional model networks of linear elastic beams, introduced in Chap. 2.

The reminder of this chapter starts with investigation of the length polydispersity with bidisperse networks consisting of only two classes of filament length: long and short. Model networks with exponentially distributed lengths are then considered, which more faithfully describe experimental F-actin systems. In sec. 3.3, the simulation results are presented: first a set of complementary phase diagrams describing the mechanical response of bidisperse networks with varied compositions of long and short filaments, and second, comparisons among monodisperse, bimodal, and exponential length distributions of the effects on mechanical modulus, deformation affinity, and energy storage. For the polydisperse networks that have been examined, the first general finding is that while there remains a well-defined affine to nonaffine crossover, the network density for the cross-over can be significantly depressed relative to the predictions determined from monodisperse networks having filament lengths

equal to mean length of the polydisperse system. Specifically, a small fraction of longer filaments can have a disproportionately strong effect of increasing the mechanical stiffness of an otherwise nonaffine network of shorter filaments, and thereby delaying the network softening transition to lower network densities. Secondly, while examining directly the geometry of the strain field or the partitioning of energy between bending and stretching modes, however, little difference has been seen between monodisperse and polydisperse networks. Thus it appears to be important to directly measure the geometry of the deformation field or the partitioning of elastic energy between stretching and bending modes to observe affine to nonaffine crossover in polydisperse networks. The third key finding is that, deep in the nonaffine regime where even polydisperse networks are highly compliant relative to the standard prediction based on affine deformation, broad distributions of filament lengths provide for the most rigid networks per unit of filament length density. This appears to be a useful design principle for creating low density but rigid filament networks when in the nonaffine regime. In sec. 3.4, the implications of these results are discussed for the mechanics of the semiflexible F-actin networks that are the frequent subject of *in vitro* experimental models of the cytoskeleton, and consider the bearing of our results on the strategies for design of advanced materials. Part of the material in this chapter is from Bai *et al.* [74]

3.2 Network Geometry

Throughout this work, units of microns are employed for simulation length, with nominal filament length $L_0 = 2$ for monodisperse networks, and bending length $\ell_b = 0.012$ representing typical values for F-actin filament. The dangling ends on both ends of filament do not contribute to the mechanics of the network [36], and are removed from our simulation network. The overall mechanical response of the filament network is therefore determined by ℓ_b along with the mean distance between crosslinks ℓ_c, which serves as an effective mechanical description of network density. For monodisperse semiflexible gels, it has been shown that the mechanical and geometric nonaffinity depend on the combination of ℓ_b and ℓ_c through a

single length scale, the so-called nonaffinity length,

$$\lambda = \ell_c(\ell_c/\ell_b)^z$$

where previous numerical simulations [35] have empirically identified $z = 1/3$.

Extending the approach of [35–37], we calculate ℓ_c for a generic polydisperse network as follows. Considering a filament of length L lying along the x-axis, the probability of crossing with another filament placed with random position and orientation can be calculated as

$$P_c(L) = \frac{2L\langle L\rangle}{\pi A}, \tag{3.1}$$

where the angled brackets here and throughout this chapter denote averaging over filament lengths for the given polydispersity $P(L)$. Thus, $\langle L\rangle$ is the average length taken over all filaments in the network. For a large number of filaments, $N \gg 1$, the probability $p_n(L)$ that this filament of length L is crosslinked n times is given by a binomial distribution with N trials and success probability $P_c(L)$, which can be approximated well by an exponential distribution

$$p_n(L) = \frac{e^{-NP_c(L)}\,[NP_c(L)]^n}{n!}. \tag{3.2}$$

The mean distance between crosslinks is then calculated as the ratio $\ell_c = \Lambda/n_c$ of the average total distance between crosslinks pairs (filament length less the dangling ends),

$$\begin{aligned}\Lambda &= \int_0^\infty dL\, P(L) \sum_{n=2}^{\infty} p_n(L)\, L\, \frac{n-1}{n+1} \\ &= \langle L\rangle + \langle Le^{-NP_c(L)}\rangle - \frac{2\langle L\rangle}{\langle NP_c(L)\rangle}\big(1 - \langle e^{-NP_c(L)}\rangle\big)\end{aligned} \tag{3.3}$$

to the mean number of crosslink pairs per filament

$$\begin{aligned}n_c &= \int_0^\infty dL\, P(L) \sum_{n=2}^{\infty} p_n(L)(n-1) \\ &= \langle NP_c(L)\rangle + \langle e^{-NP_c(L)}\rangle - 1.\end{aligned} \tag{3.4}$$

3.2.1 Affine Response

In comparing the mechanical responses of different networks, here throughout in this chapter the computed shear modulus is reported relative to the value it would have under an affine

(uniform) shear deformation, G_{affine}, which can be calculated analytically in a similar manner by averaging the shear stiffness of each filament of length L at angle θ as

$$G_{\text{affine}} = \frac{\mu N}{2\pi A} \int_0^\infty dL P(L) \int_0^{2\pi} d\theta \, \sin^2\theta \cos^2\theta \sum_{n=2}^{\infty} p_n(L) \, L \, \tfrac{n-1}{n+1},$$

which simplifies to

$$G_{\text{affine}} = \frac{\mu N}{8A} \Lambda. \tag{3.5}$$

There are two good reasons to report the numerically computed shear modulus, G relative to the value that would be expected under an affine shear strain, G_{affine}. First, the primary mechanical signature of the affine to nonaffine transition is the deviation of network's shear modulus G from its affine prediction G_{affine}, as given in Eq. (3.5). Second, the calculation of the affine shear modulus G_{affine} automatically accounts for the mechanical effect of dangling ends. Clearly, in the strained network the dangling ends—i.e., the lengths of the filaments extending past the crosslinks closest to the ends of the filaments—cannot store elastic energy. They are irrelevant to the elasticity of the system. If one were to compare two monodisperse networks having the same total length density but different filament lengths, the system with the shorter filaments (but in greater number) would have more of these dangling ends and thus be more elasticity compliant. By normalizing the observed shear modulus by the affine prediction, we take this dangling end effect into account, allowing us to concentrate on the less trivial changes in the mechanics. Finally we note in passing that as a consequence of dangling ends, a network of monodisperse filament lengths has, in fact, a polydisperse distribution of active, load-bearing filament lengths, as discussed further in Appendix A. Hence, in the sense of mechanically relevant filament lengths, all random semiflexible networks are polydisperse. To be clear then, we use the term "monodisperse" in the commonly understood sense, referring to the lengths of filaments in isolation.

3.3 Results

3.3.1 Bidisperse Length Distribution

The numerical studies begins with considering *bidisperse* networks, composed of filaments of only two lengths: N_s "short" filaments of length L_s, and $N_l = N - N_s$ "long" filaments of length $L_l = rL_s$, with the length ratio $r > 1$. In anticipation of the application of this work to polydisperse F-actin networks, the mechanical properties of all the filaments are fixed to be identical. All filaments are assigned the same bending and stretching moduli μ and κ. This makes the bending length ℓ_b a constant.

For such bimodal distributions the composition of the network can be described by three scalar quantities: (i) the total filament length density, (ii) the fraction of that density stored in the longer (or equivalently the shorter) filaments, and finally (iii) the ratio of the length of the long filaments to the short ones. There are clearly other parameterizations of this information possible; discussions below talk about which parameterizations are most directly obtainable from experimental parameters, and which are most useful in understanding the mechanics of the network. Although such bidisperse filament distributions are not easily realizable in experiment or commonly found in biological materials, understanding this system is useful since it is the most easily characterized form of length polydispersity due to the simplicity of the distribution.

In the following a *mechanical phase diagram* is presented which shows the observed shear modulus of the network G as a function of two of the parameters characterizing the density and length distribution of the network. To do this one of the three parameters discussed above must be fixed. The ratio of the length of the long filaments to the short ones, $r = L_l/L_s$, is fixed and vary independently to the length density of the short and long filaments. For the bimodal-length networks considered here, the expression for the average length

$$\langle L \rangle = \frac{N_s}{N} L_s + \frac{N_l}{N} L_l = \frac{N_s + rN_l}{N} L_s, \tag{3.6}$$

leads to a natural decomposition of the length density (i.e., the total length of filaments per

unit area in our two dimensional system) as

$$\rho = \frac{N\langle L\rangle}{A} = \frac{N_s L_s}{A} + \frac{N_l L_l}{A}, \tag{3.7}$$

where we denote partial densities of long and short filaments as

$$\rho_l = \frac{N_l L_l}{A} \quad \text{and} \quad \rho_s = \frac{N_s L_s}{A}. \tag{3.8}$$

These two densities reflect quantities that have the most direct meaning in experiment, representing the total amount of material (or filament length) stored in the forms of long and short filaments. Lastly, we note that, although we separate the filament density into long and short densities, the shear moduli G and G_{affine} are computed for the entire bimodal network as a whole. Furthermore, while for a given network composition G_{affine} is defined uniquely by eqn. (3.5), G is subject to some variation from one randomly generated network instance to another. Although points plotted in the phase diagram and elsewhere below each represent results for a single network instance, we have compared multiple instances for a few compositions, measuring variations in G as much as on the order of 5% for networks in the NA regime. Networks in the A regime are more self-averaging, showing sample-to-sample variation of the modulus of $< 1\%$. Most important, however, is the observation that these sample-to-sample variations are everywhere dramatically smaller than the (average) differences between affine and non-affine samples. Based on these considerations, and because in the A regime G/G_{affine} approaches one independent of network composition, attempt to curtail computational costs is made by generally clustering simulation data points in the NA region.

Fig. 3.1 shows a mechanical phase diagram for bidisperse networks with long/short length ratio $r = 5$. The color contours report the simulated network shear modulus G normalized by G_{affine} over a range of long and short filament densities ρ_l and ρ_s, rendered dimensionless by multiplication with short filament length L_s. Just as for monodisperse networks [36], G/G_{affine} generally increases with increasing density ρ (or decreasing ℓ_c). However, the plot makes clear that the mechanics of polydisperse networks is also strongly dependent on the composition of filament lengths, as indicated by ρ_l/ρ_s. Specifically, the contours of constant

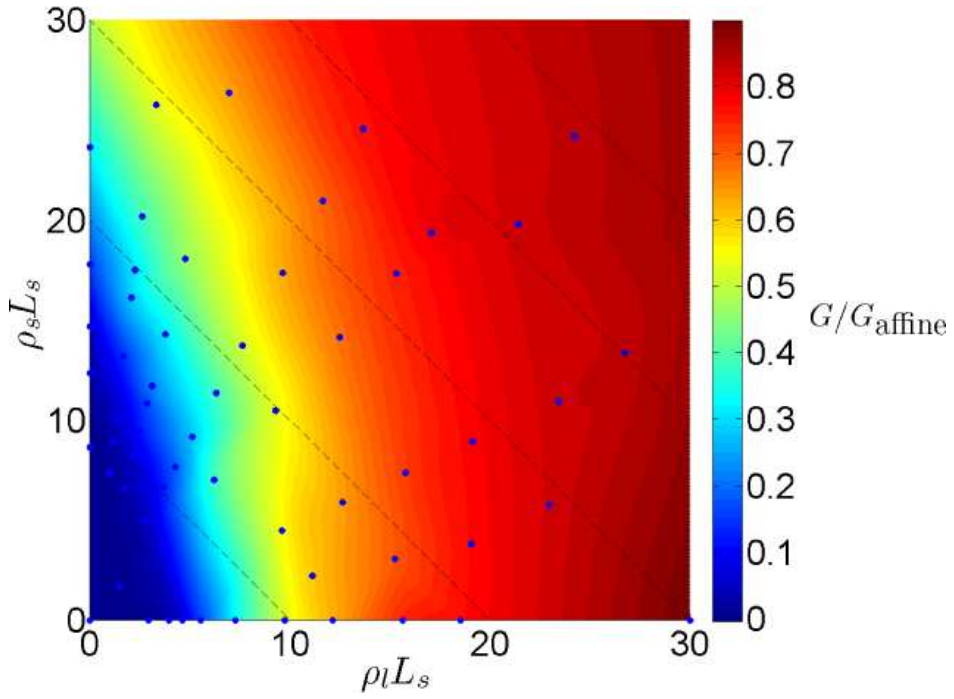

Figure 3.1: The phase diagram of G/G_{affine} versus filament densities ρ_l and ρ_s normalized by short filament length L_s, for a series of bimodal-length networks with $r = L_l/L_s = 5$. Blue dots indicate actual simulation data points. Contours were generated by piecewise cubic interpolation of the simulation data using the subroutine `griddata` from MATLAB (The MathWorks, Inc.). Dashed lines of constant total filament density $\rho = \rho_l + \rho_s$ are shown as a guide to the eye to distinguish the composition dependence of G/G_{affine}.

mechanics (G/G_{affine}) are generally curved "downward" toward the ρ_l axis, relative to the straight (dashed) lines of constant total density ρ with slope -1. In other words, as the composition is shifted from short-dominated ($\rho_l < \rho_s$) toward long-dominated ($\rho_l > \rho_s$) the gradient direction of G/G_{affine} turns increasingly toward the ρ_l axis. Consequently, the phase diagram suggests an enhanced stiffening effect from redistributing the sum of filament lengths into long filaments. That is, as the concentration of long filaments increases, addition of a unit of length density in the form of long filaments stiffens the network increasingly more than addition of the same unit in the form of short filaments.

Conversely, one can consider changes in the densities of the long and short filaments along contours of constant G/G_{affine}. For short-dominated networks with $\rho_l \ll \rho_s$, contours

of constant mechanics track closely with lines of constant total density. Thus, simply exchanging a unit of short-filament density for a unit of long-filament density, say by splicing together r short filaments to create one new long filament, will have little effect on the mechanical response of the network. However, as the concentration of long filaments increases, the contours of constant mechanics turn continuously downward, such that many units of short-filament density can be exchanged for a single unit of long-filament density while leaving the mechanical response unchanged. In summary, long filaments are more efficient than short filaments in stiffening the network. We refer to this property as a greater *mechanical efficiency* of the long filaments relative to that of the shorter ones.

To understand the greater mechanical efficiency of the longer filaments distinct from the dangling ends effect, it is useful to review the results of the mechanics of monodisperse filament networks and the nonaffine to affine crossover. There, as noted above, it was found that the shear modulus G and the so-called *mechanical affinity* measure G/G_{affine} depends on the filament mechanics and network density through only one parameter L/λ, the ratio of the length of the filaments to the *nonaffinity length* $\lambda = \ell_c(\ell_c/\ell_b)^{\frac{1}{3}}$. If we have two monodisperse networks of long and short filaments having the same value of G/G_{affine} (such pairs of networks can be read off of the vertical and horizontal axes of Fig. 2) then it must be that $L_l = rL_s$ and $L_s/\lambda_s = L_l/\lambda_l$ since the function $G/G_{\text{affine}}(L/\lambda)$ is one-to-one. Recalling that the mechanics of the individual filaments in each network are identical, it follows then that

$$\frac{(\ell_c)_l}{(\ell_c)_s} = r^{\frac{3}{4}}. \tag{3.9}$$

For monodisperse networks at all but the smallest densities, ℓ_c is proportional to the inverse of the length density [75]. Thus from Eq. (3.9) and $r = 5$ we find that networks of long and short filaments with the *same* G/G_{affine} will have a significant difference in the length density $\rho_l = r^{-\frac{3}{4}}\rho_s \approx 0.3\rho_s$. This is consistent with the values of G/G_{affine} along the axes of Fig. 3.1. The longer filament network is equally rigid (compared to the affine prediction) as a shorter filament network at about three times the length density. In this example, we may say that the longer filaments are three times more mechanically efficient.

One might imagine that this concept of the mechanical efficiency of a filament accounts

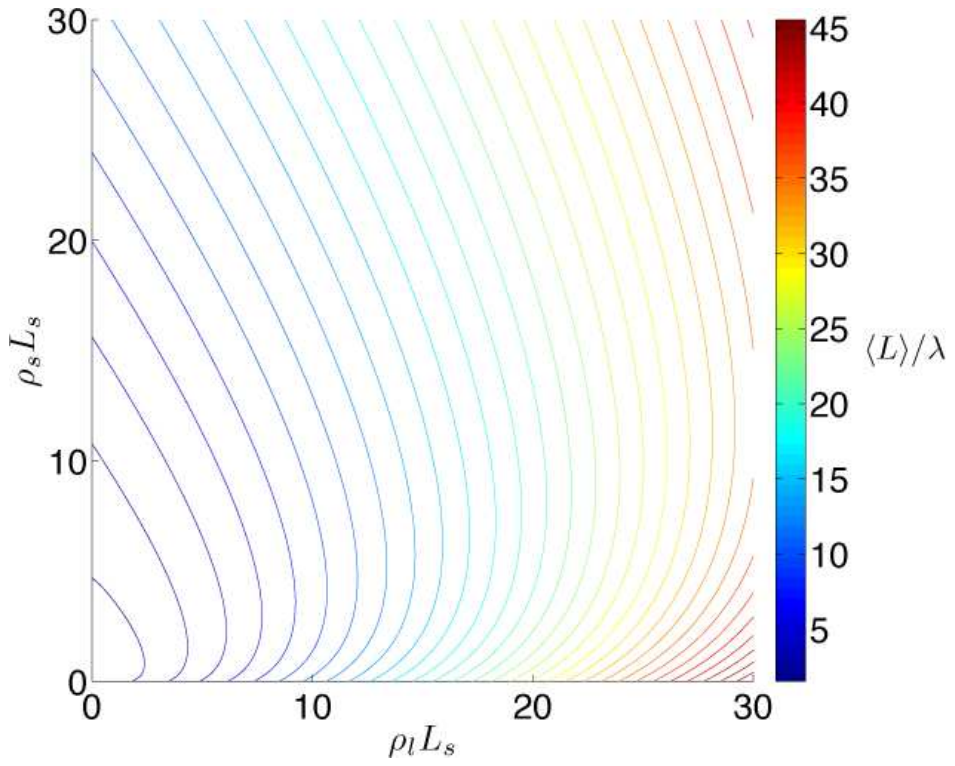

Figure 3.2: Phase diagram of $\langle L \rangle / \lambda$ as computed from eqn. (3.3) and (3.4) for a bimodal network with long/short length ratio $r = L_l/L_s = 5$, as a function of partial densities of long and short filaments ρ_l and ρ_s defined in eqn. (3.8), and normalized by short filament length L_s.

for the entire structure of the lines of constant modulus and not just for their endpoints on the two axes of the mechanical phase diagram and thus explains why lines of equal mechanics deviate significantly from lines of constant total length density (shown as black dashed lines in Fig. 2) in bidisperse networks. These ideas, however, have only been validated for monodisperse networks. To generalize these results to polydisperse ones, we propose replacing the filament length L in the ratio L/λ by the mean filament length in the network $\langle L \rangle$. The determination of λ proceeds as before. There is no *a priori* reason to demand that the functional dependence of G/G_{affine} on $\langle L \rangle / \lambda$ is identical to that of the same quantities for monodisperse networks, but we expect such an analogous relation between modulus and $\langle L \rangle / \lambda$ for fixed composition to be at least monotonically increasing and one-to-one. If this be the case, contours of constant $\langle L \rangle / \lambda$ correspond to contours of constant modulus and

larger values of $\langle L\rangle/\lambda$ correspond to more affine and mechanically incompliant networks. In Fig. 3 we plot the contours of $\langle L\rangle/\lambda$ *vs.* the partial densities. The lines of constant G/G_{affine} in Fig. 2 appear to agree to much higher precision with the lines of constant $\langle L\rangle/\lambda$ in Fig. 3 than with the (dashed) lines of constant length density.

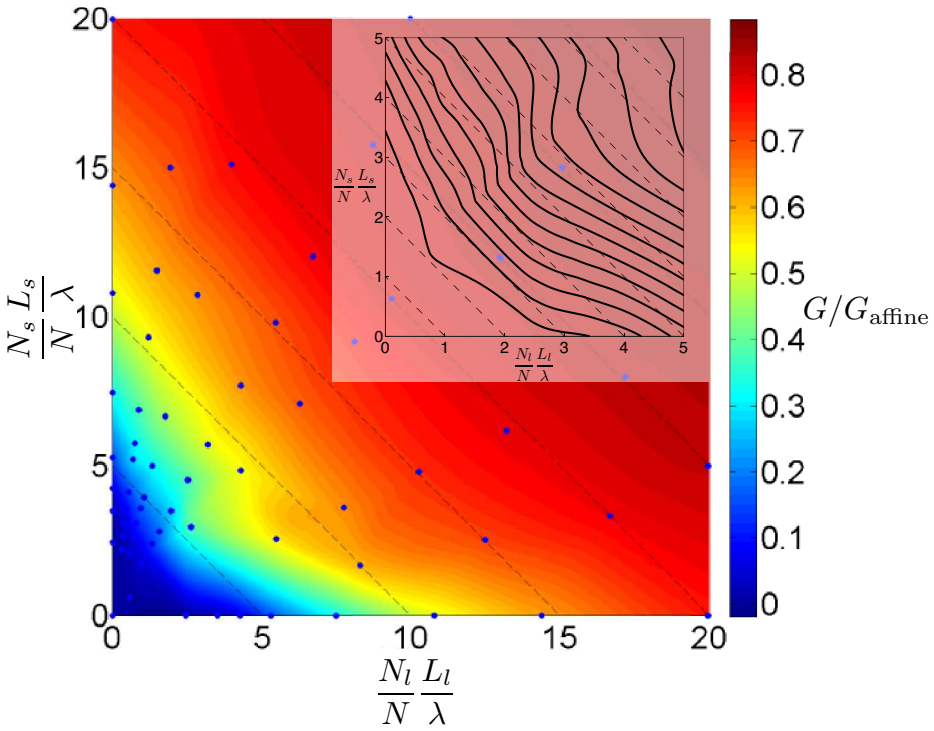

Figure 3.3: The phase diagram of G/G_{affine} versus $\frac{N_l L_l}{N\lambda}$ and $\frac{N_s L_s}{N\lambda}$ for the same series of bimodal-length networks with $r = L_l/L_s = 5$ plotted in Fig. 3.1. This alternative parameterization has the advantage of rendering contours of constant $\langle L\rangle/\lambda$ as straight (dashed) lines of slope -1 (see text). Contours of G/G_{affine} bend toward the origin away from lines of constant $\langle L\rangle/\lambda$, demonstrating that polydisperse networks are stiffer, or mechanically more affine, than monodisperse networks of equal $\langle L\rangle/\lambda$. Inset: zoomed in view of the highly nonaffine region of the phase diagram.

To make a quantitative comparison between Figs. 2 and 3, it is helpful to redefine the two axes of the mechanical phase diagram in a manner that directly incorporates $\langle L\rangle/\lambda$. For bidisperse networks we may use the following decomposition

$$\frac{\langle L\rangle}{\lambda} = \frac{N_l L_l}{N\lambda} + \frac{N_s L_s}{N\lambda}. \tag{3.10}$$

Fig. 3.3 shows the mechanical phase-diagram replotted as G/G_{affine} *vs.* $\frac{N_l L_l}{N\lambda}$ and $\frac{N_s L_s}{N\lambda}$. Dashed lines indicate the straight contours of $\langle L\rangle/\lambda$ with slope -1, revealing that contours of constant G/G_{affine} tend to curve toward lower $\langle L\rangle/\lambda$ for mixed compositions of long and short filaments. In other words, for each value of $\langle L\rangle/\lambda$, there is a mechanically optimal composition $N_l L_l/N_s L_s = \rho_l/\rho_s$ at which G/G_{affine} attains a maximum value. It appears that this maximum is attained near to the line of equal composition, $\rho_l = \rho_s$, although a precise location is difficult to identify due to the noise in the contour plot generated by interpolation over a rather sparse set of data points. Throughout the phase-diagram, and most clearly at lower densities (see the inset of Fig. 4), bidisperse networks, i.e., those for which $\rho_l, \rho_s \neq 0$ are always stiffer than monodisperse networks (where either ρ_l or $\rho_s = 0$) of the same $\langle L\rangle/\lambda$. Thus, the proposal that G/G_{affine} depends on only $\langle L\rangle/\lambda$ is not precisely satisfied, but lines of constant $\langle L\rangle/\lambda$ more nearly correspond to lines of constant mechanics. Interestingly, the residual corrections, especially at small values of $\langle L\rangle/\lambda$, where the network is expected to deform in a highly nonaffine manner, show that maximal mechanical efficiency occurs generically for compositions in which the two contributions to $\langle L\rangle/\lambda$ are roughly equal: $\frac{N_l L_l}{N\lambda} \approx \frac{N_s L_s}{N\lambda}$.

The stiffening effect of length polydispersity is more dramatically demonstrated by comparing fixed composition cuts through the phase diagram, as shown in Fig. 3.4, which plots G/G_{affine} as a function of $\langle L\rangle/\lambda$, for a selection of different long/short filament length ratios $r = L_l/L_s$, and compositions ρ_l/ρ. As pointed out in Fig. 4, we find that the ratio of the mean filament length to the nonaffinity length does not determine uniquely the mechanics of the network. G/G_{affine} is dependent on both the length ratio r and composition ρ_l/ρ at fixed $\langle L\rangle/\lambda$. Consistent with the phase diagram in Figs. 3.1 and 3.3, we see that polydispersity in filament lengths increases network's stiffness, or more precisely, the mechanical affinity, G/G_{affine}, and that this effect is most significant for sparse networks that are in the nonaffine regime where $\langle L\rangle/\lambda \lesssim 15$. For example, at $\langle L\rangle/\lambda \approx 2.5$, a polydisperse network with about 10% of its density ($\rho_l/\rho = 0.11$) stored in the form of long filaments ($r = 5$) is an order of magnitude stiffer than a monodisperse network of the same density. Likewise, distributing one third of the same density ($\rho_l/\rho = 0.35$) to filaments that are 10 times longer ($r = 10$)

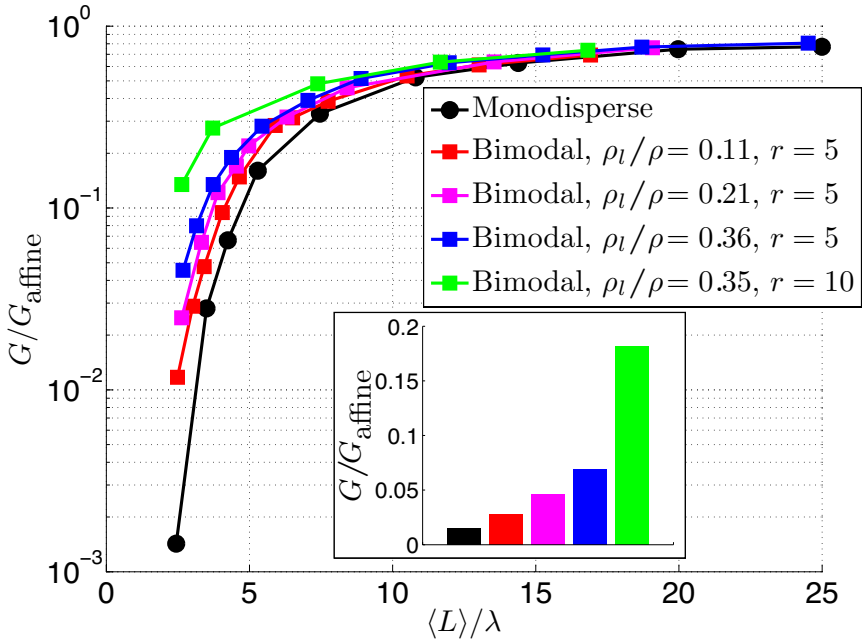

Figure 3.4: Normalized shear modulus G/G_{affine} versus $\langle L\rangle/\lambda$ for the whole network. The dangling ends which don't contribute to the network's mechanics have been removed. Curves are grouped by long filament length fraction, ρ_l/ρ, and long/short length ratio r. The inset shows significant G/G_{affine} increase between monodisperse and bimodal polydisperse network at $\langle L\rangle/\lambda = 3$.

than the rest stiffens the network a hundred-fold. This demonstrates that network stiffening effect is sensitive to both long filament length fraction ρ_l/ρ and the long/short length ratio r. The latter dependence is clearly demonstrated by comparison of the $\rho_l/\rho = 0.36$, $r = 5$ (magenta) and $\rho_l/\rho = 0.35$, $r = 10$ (green) curves. These have the same total length density of long filaments, but differ by a factor of two in the long/short length ratio, illustrating that simply splicing together pairs of long filaments stiffens the network by a roughly half a decade, at least deep in the nonaffine regime. As expected for affine networks (i.e., those with $\langle L\rangle/\lambda > 20$) there is essentially no mechanical effect of the filament length distribution once the dangling ends effect has been removed.

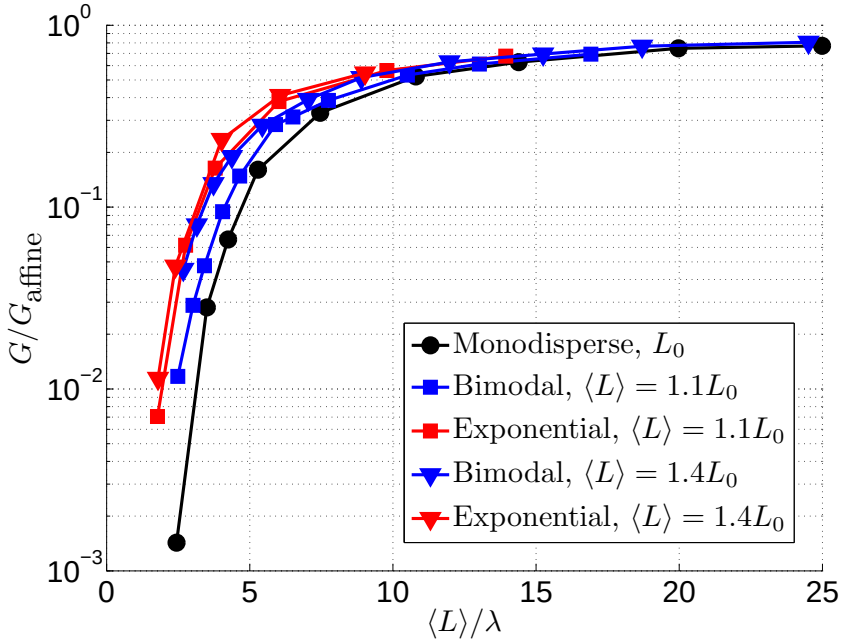

Figure 3.5: Normalized shear modulus G/G_{affine} versus $\langle L\rangle/\lambda$, for monodisperse, bimodal polydisperse and exponential polydisperse networks. Bimodal networks were defined with $L_s = L^{\text{mono}}$ and $r = 5$. Exponential length distributions were truncated at $\ell_0 = L_0/4$ as indicated in eq.(3.11), so as to neglect filaments too short to be mechanically active.

3.3.2 Exponential Length Distribution

Bidisperse networks provide a restricted class of polydisperse systems that can be easily characterized and thus systematically explored, as in the previous section. It is well-known, however, that the most ubiquitous example of semiflexible networks is found in the predominantly F-actin based cytoskeleton and its simplified *in vitro* models. Previous theoretical and *in vitro* experimental studies have predicted and shown that the polymerization process results in polydisperse filament networks with filaments having varying length. *In vivo*, dynamically growing and remodeling actin networks are also known to have a rather broad length distribution. Theoretically, the lengths of actin filaments have been predicted to be exponentially distributed [1]. Viamontes *et al.* [72] measured the length distribution of the filaments used in their experiment and found a peaked distribution, which appeared exponential at larger lengths. They claimed that the polydispersity is responsible for affecting

orientational ordering and perhaps also other properties of the network. In recent theoretical and experimental studies on composite F-actin/microtubule networks, Bai *et al.* [44] and Lin *et al.* [43] found that polydispersity in the mechanical stiffness of filaments can have a large effect on the overall mechanical response of a gel, while affecting the geometric nonaffinity to a lesser degree. Those studies revealed that the addition of just a small fraction of stiff microtubules to a soft, nonaffine, actin gel can effect an increase in the effective shear by several orders of magnitude. Here we consider whether an exponential distribution of filament lengths can produce similar cooperative changes to the mechanical response of networks.

Based on our intuition gleaned from the bidisperse case, we expect the rare long filaments to have a disproportionately large effect on the mechanics of the network deep in the nonaffine regime. To explore this we consider an exponential length distribution

$$P(L) = \begin{cases} \frac{1}{\ell} e^{-\frac{L-\ell_0}{\ell}}, & \text{for } L \geq \ell_0 \\ 0, & \text{otherwise} \end{cases} \tag{3.11}$$

cutoff at $\ell_0 = 0.25L_0$. Here L_0 is the filament length of our monodisperse networks to which we compare our data. The details of the distribution at short lengths, smaller than that of the mean distance between crosslinks, are mechanically irrelevant. The exponential distribution is characterized by a single decay length ℓ, which we adjust to set the desired mean filament length

$$\langle L \rangle = \int_{\ell_0}^{\infty} P(L) L dL. \tag{3.12}$$

Using this measure, in Fig. 3.5 we plot G/G_{affine} for networks having an exponential length distribution as a function of $\langle L \rangle / \lambda$, along with the analogous mechanical data from the previously discussed mono- and bidisperse networks.

Comparing the mechanics of networks having exponential distributions (red triangles and squares) to those of a monodisperse (black filled circles) and two bidisperse (blue squares and triangles) networks we note two points. First, while the mechanics are relatively insensitive to the mean length (comparing the red squares and red triangles), at least over the range explored, overall in the nonaffine regime the exponential filament distribution leads to the most stiff networks for a given value of $\langle L \rangle / \lambda$. Second, the curves are essentially identical

in shape. Hence, it appears that measurement of the G/G_{affine} vs. $\langle L\rangle/\lambda$ alone does *not* provide a means to determine the form of the filament length distribution. The principal effect of polydispersity is simply to push the crossover to nonaffine mechanics to even lower values of $\langle L\rangle/\lambda$. We also note that exponential length distributions generate the greatest mechanical efficiency within the set of distributions studied. These results are consistent with the observations that within the bidisperse networks larger r and roughly equal length densities (i.e., broader distributions) exhibit greater mechanical efficiency. It is tempting to speculate that all of these results when taken together point to the principle that broader filament length distributions generally lead to higher mechanical efficiency in the nonaffine regime. We return to this point in the discussion.

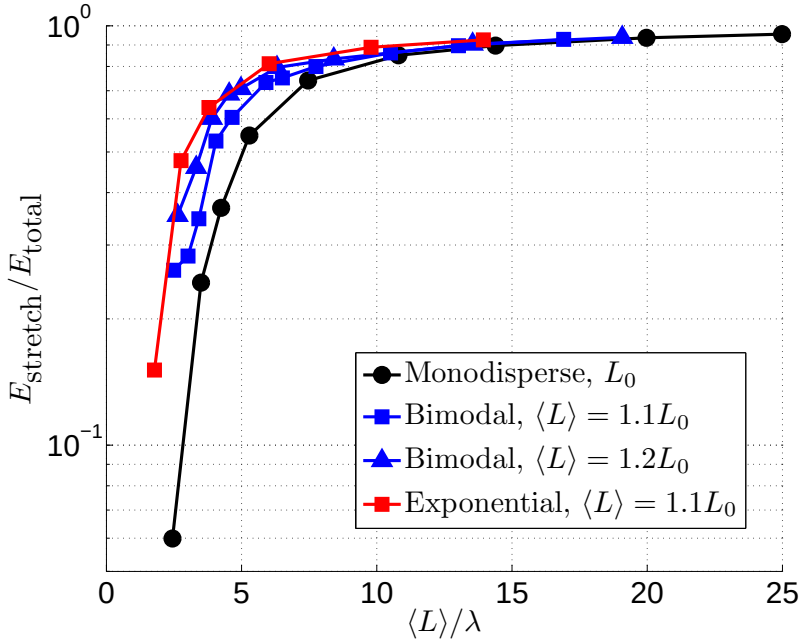

Figure 3.6: The stretching energy fraction in total energy is plotted against $\langle L\rangle/\lambda$. Two comparisons are made: the effect of long filament length fraction in bimodal polydispersity; the effects of bimodal and exponential polydispersities.

3.3.3 Deformation Field and Elastic Energy Storage

Previous studies on monodisperse gels have shown that the changes in the mechanical properties across the affine-nonaffine transition are driven, as semantically implied, by changes in the nature of the deformation field from affine at high crosslink densities, to nonaffine at low densities. Under purely affine strains, all filaments in a network are subjected to pure stretching (length change) deformation along their lengths. However, in sparse and nonaffinely deforming networks, filaments undergo a combination of stretching and bending deformations. To explore whether the same mechanisms apply for polydisperse networks, we plot in Fig. 3.6 the fraction of energy stored in stretching, as a function of $\langle L\rangle/\lambda$, for representative monodisperse, bimodal, and exponential networks. It is clear from this plot that, just as in the monodisperse case, polydisperse networks shift their energy from stretching to bending as the density of filaments/crosslinks is decreased. A closer comparison to the monodisperse case reveals that the polydisperse networks undergo a slightly delayed, and sharper shift from stretching to bending. Decrease in the stretching fraction sets in more abruptly, and at lower values of $\langle L\rangle/\lambda$. Thus, the enhanced stiffening seen in polydisperse networks at low densities is correlated with and likely derived from a suppression of appearance of bending deformations as the network is made more sparse.

To test the intuition from monodisperse studies that the increase in bending energy should be also a signature of increasingly nonaffine strains, we also examine directly the network deformation fields. Figure 3.7 shows a vector plot of the displacement field for a random sampling of nodes in three typical bidisperse networks (r=5, ρ_l/ρ=0.11) above, below, and just at the onset of the A/NA transition. At and above the transition ($\langle L\rangle/\lambda$=10, 25) the strain field is visually indistinguishable from a pure (affine) shear; whereas below the transition ($\langle L\rangle/\lambda$=3) the presence of non-affine deformation is clearly manifested in the vortex-like patterns exhibiting significant vertical (and even horizontally retrograde) displacements. To be quantitative in describing the degree of non-affine deformation we consider the geometric nonaffinity measure introduced previously [35–37]

$$\Gamma(r) = \langle(\theta - \theta_{\text{affine}}(r))^2\rangle/\gamma^2 \tag{3.13}$$

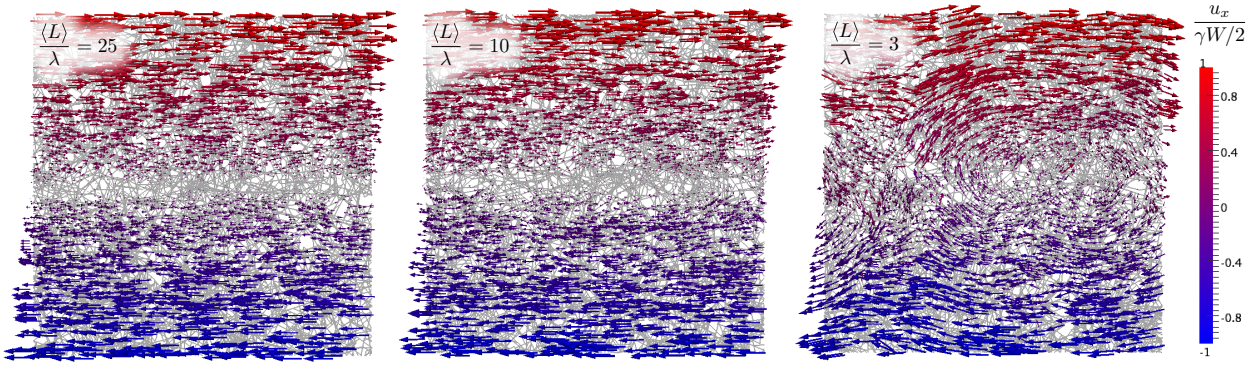

Figure 3.7: Vector field plots of the displacement field in bidisperse networks (r=5, ρ_l/ρ=0.11) well above ($\langle L \rangle/\lambda$=25), well below ($\langle L \rangle/\lambda$=3), and just at the onset ($\langle L \rangle/\lambda$=10) of the A/NA transition. Network filaments are shown superposed in gray. Color contours represent the value of horizontal displacement normalized by the maximum affine displacement at the top boundary. Vector glyphs are plotted at a randomly sampled subset of nodes, with lengths uniformly rescaled for better visibility.

where θ is the rotation angle of the line connecting two network nodes separated by distance r, $\theta_{\text{affine}}(r)$ is the corresponding rotation angle under an affine deformation, and γ is the shear strain. In Fig. 3.8 we plot Γ vs. separation distance r normalized by ℓ_c, for monodisperse, bimodal, and exponential networks above ($\langle L \rangle/\ell_c$=25), near ($\langle L \rangle/\ell_c$=10), and below ($\langle L \rangle/\ell_c$=3) the A-NA transition. The plot shows that polydispersity has little overall impact on the qualitative trends of geometric nonaffinity: for affine networks Γ increases but plateaus as $r \to 0$, while for nonaffine networks Γ continues to grow as r is reduced. Quantitatively, for very sparse networks ($\langle L \rangle/\lambda$=3) polydispersity leads to some increase — albeit slight — in the overall nonaffinity as compared with monodisperse networks. For higher $\langle L \rangle/\lambda$ overall quantitative differences in nonaffinity between monodisperse and polydisperse are more ambiguous. The discrepancy between impact of polydispersity on mechanical affinity (e.g., G/G_{affine} and E_{stretch}/E) and geometrical nonaffinity (Γ) suggest that the correlation between network mechanical properties and deformation field that is apparent for monodisperse networks is not a general feature of networks of polydisperse length distributions. A similar observation of independence between mechanical and geometrical measures of nonaffinity was also found in the work presented in next chapter on composite networks of soft

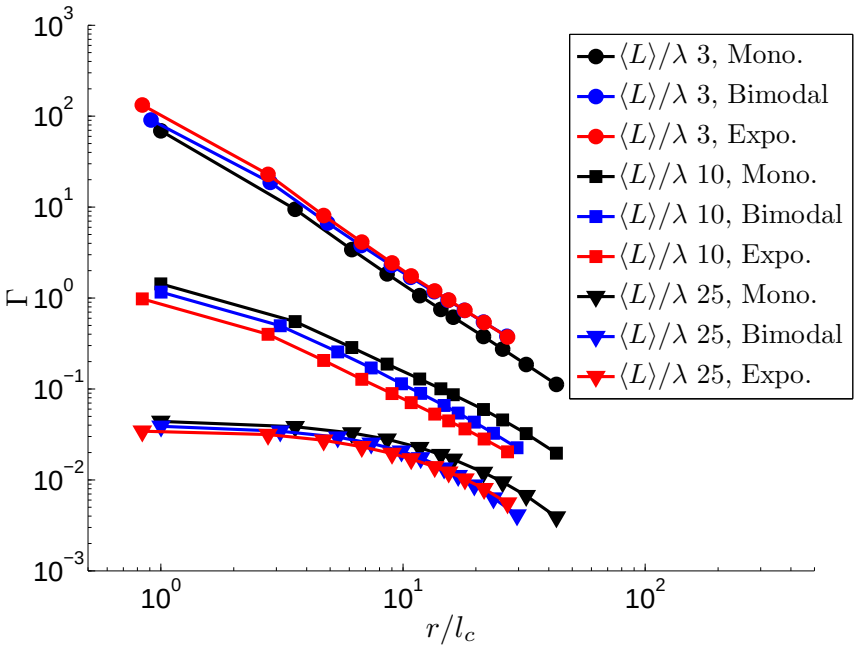

Figure 3.8: Nonaffinity Γ plotted against normalized measuring distance r/ℓ_c. Monodisperse and polydisperse networks with different filament densities: $\langle L\rangle/\lambda = 3$, $\langle L\rangle/\lambda = 10$, and $\langle L\rangle/\lambda = 25$ are tested and plotted.

F-actin-like filaments and stiff microtubule-like filaments [44].

3.4 Discussion

The principle conclusion of this chapter is that for polydisperse networks the mean filament length alone is not sufficient to determine its mechanics when that network is in the nonaffine regime. In order to quantify this property the bidisperse networks are examined and the mechanical efficiency of a filament length distribution — the ratio of the network's shear modulus to its affine value as a function of total length density, is introduced. To put this in another way: Given a fixed mass of filament making material (e.g., monomeric actin) to span a given region, one may ask which partitioning of that mass into filaments (i.e., which length distribution) provides for the most rigid network. Deep in the nonaffine regime, it appears that the broader the distribution of lengths, the stiffer the network. Such broad length distributions proved the most efficient use of the material to create a stiff random structure.

In the affine regime, on the other hand, the filament length distribution is irrelevant except for the rather trivial dangling end effect.

There are two main consequences of this result. First, experiments that seek to observe the nonaffine regime (primarily in F-actin gels) must be concerned about the role of polydispersity and particularly the presence of long "impurity" filaments in the sample. These rare long filaments suppress the mechanical effect of nonaffine deformation requiring one to create even more sparse networks to observe a regime in which $G/G_{\text{affine}} \ll 1$. One may speculate that for a sufficiently broad filament length distribution it may be possible to suppress the highly compliant nonaffine mechanical regime down to network densities approaching the rigidity percolation transition. In this case there may be no mechanically distinct nonaffine regime intermediate between the critical regime associate with stress percolation and the $G/G_{\text{affine}} \approx 1$ regime normally associated with an affinely deforming elastic solid. Regardless of the suppression of the dramatic network softening in the nonaffine regime seen in monodisperse networks, the geometric signature of nonaffine deformation and the change in the partitioning of elastic energy between filament bending and stretching associated with the entry into the nonaffine regime is still found in polydisperse networks. It appears that these latter two signatures of the nonaffine regime originally observed in simulations of monodisperse networks are more robust to network heterogeneity than the mechanical signature, i.e., $G/G_{\text{affine}} \ll 1$. This observation is also supported by simulations [44] and experiments [43] on F-actin and microtubule composite networks. We suggest that measures of the either energy storage in bending degrees of freedom or the direct geometric measure of nonaffine deformation are more reliable experimental measures of nonaffinity than the mechanical effect. The analytical and numerical prediction of the nonaffine/affine transition by [35–39, 65–69, 76] has been found qualitatively consistent with *in vitro* experiments, however quantitative validation is so far not definitive. [63] performed a series of experiments measuring overall stiffness of actin networks under varying crosslink densities with three different kinds of crosslinking proteins. While this study found that the overall shear modulus of the network increased with crosslink density, the measured stiffness of networks predicted to be in the nonaffine region as defined in the paper by [36] did not deviate noticeably from

the affine shear modulus prediction. [64] experimentally probed the geometric nonaffinity in F-actin networks at various actin/crosslink densities, finding that the measured nonaffinities for both dense and sparse networks lie between the theoretical pure affine and pure nonaffine limits. However, the differences in measured nonaffinity among networks at various densities were found to be rather small.

Experimentalists have not yet observed the predicted abrupt change in modulus associated with the affine to nonaffine crossover for monodisperse network predicted in both theory and simulation. Based on our results regarding the effect of polydispersity on the affine to nonaffine transition, it appears that one contributing factor to this discrepancy is polydispersity, or more specifically, the presence of at least a low density of longer filaments. We suggest that these longer filaments push the mechanical softening to even smaller network densities. Also since for polydisperse networks, geometric nonaffinity is not directly associated with mechanical affinity as opposed ro monodisperse network, those two nonaffinities are suggested to be measured directly and studied separately.

Secondly, if one were to engineer biomimetic semiflexible networks that are sparse and yet wish to maximize the linear modulus for a fixed amount of material, developing a random network with a broad filament distribution appears to be ideal. This suggests a design principle for the construction of of simultaneously light-weight (due to the low volume fraction of the network) and rigid materials from filament networks. This principle may be exploited using F-actin, microtubules, or even carbon nanotubes. By analogy to traditional fiber-based composites, semiflexible networks have the distinguishing feature that filaments play both the role of fiber reinforcement, and the matrix. Accordingly, by pushing the A/NA transition toward the percolation threshold, length polydispersity greatly enhances the strength-to-weight ratio of the network at low fiber densities. Furthermore, in contrast to traditional fiber composites, for which design strategies are needed to control local (non-affine) strain gradients, which serve as the main source fiber debonding failure, semiflexible networks are free of bi-material, fiber-matrix interfaces, and can therefore perform robustly despite non-affine strains. These latter observations raise new questions about the optimal design for such strong and light materials created out of crosslinked stiff filaments. Is there

a particular length distribution, set of impurities (e.g., stiffer filaments) or even network organization (e.g., local nematic order [42]) that maximizes the mechanical efficiency of the filaments? In this study we note that polydispersity enhances mechanical efficiency. It remains to be seen how length polydispersity interacts with the addition of mechanically stiffer filaments to enhance (or not) the mechanical efficiency of the composite network. Moreover, it is an open question whether the structure of the cytoskeleton is so organized as to take advantage of the enhanced mechanical efficiency of highly polydisperse networks.

We close by pointing out some of the limitations of the present analysis. First, we have confined our attention to polydisperse networks of filaments with fixed mechanical properties, as described by the bending length ℓ_b. As noted above, previous studies of monodisperse networks found that scaling by the nonaffinity length λ universally captures the effects of changing crosslink density ℓ_c and the relative stiffness of filaments in bending and stretching. While herein we have reported modulus results only for simulations where ℓ_c is varied with ℓ_b fixed, we have also examined the modulus as a function of ℓ_b for a few select length compositions (not shown). In these few cases, G/G_{affine} still collapses as a function of $\langle L \rangle / \lambda$ along with the cases where ℓ_c was varied. Secondly, the present analysis focuses purely on the linear shear response of networks. This leaves open the question of the effect of length polydispersity on the nonlinear network response. In particular, previous theoretical studies by Onck, *et al.* [77, 78] and Mahadevan, *et al.* [79, 80] have shown that changes in the local geometry of filaments brought about by large network deformations are important in defining the nonlinear response. By defining the network geometry with initially straight filaments, and restricting our analysis to small shear strains, we neglect these nonlinear effects. Likewise we neglect the role of initial prestress, which is likely present in real semiflexible networks cross-linked in the presence of thermal fluctuations. Exhaustive studies of the interaction of length polydispersity with each of these effects would be interesting to pursue as future research.

CHAPTER 4

Mechanical Polydispersity: Composite Actin-Microtubule Networks

4.1 Introduction

As stated in previous chapters, the affine to non-affine (A/NA) cross-over of monodisperse semiflexible network is characterized by three effects. First, the non-affine networks are significantly softer than that predicted by the affine theory. Secondly, the geometry of deformation in the NA regime is quite complex. Under uniformly applied shear strain at the boundaries of a NA sample, the observed strain field is far from being spatially uniform as would be expected for a continuum elastic object. In fact, large regions are typically found in which the material is not shearing, but rather undergoing local rigid body motions. The regions of the network in between these rigidly moving sections become distorted and store elastic energy. Finally, deep in the NA regime, sheared networks store elastic energy almost entirely in the bending deformations of the filaments. In the affine regime, however, networks store energy predominantly in the stretching modes of the filaments as is the expected response to a uniform shear strain. These phenomena may be understood by noting that in more sparsely cross-linked networks that are deep in the NA regime it is not meaningful to write the elastic free energy of the system in terms of a gradient expansion of the local strain field. Presumably this breakdown of continuum elasticity can be attributed to the large quenched spatial variations of local elastic response of the network. Under uniformly applied shear, regions of the network that are slightly more dense than their surroundings perform rigid body motions and thereby do not store elastic energy. Because these motions do not allow for a state of uniform shear strain, filaments in the sparser regions are thereby

forced to bend to simultaneously accommodate the strain field boundary conditions at the edges of these more rigid regions and at the boundaries of the sample where the shear strain is applied. Because few filaments store elastic energy, the NA networks appear to be anomalously soft when compared to the predictions assuming affine deformation wherein each filament undergoes a deformation determined solely by its orientation with respect to the shearing direction. Lastly, assume the lengths of filaments could be made longer, these slightly more rigid regions would become more strongly connected mechanically. These stronger connections would enforce more precise self-averaging of the strain field in the sample resulting in a more nearly affine deformation field and a stiffer mechanical response as more filaments store elastic energy. Since the local deformation field (under uniformly applied strain at the boundaries) approaches that of simple shear, bending deformations could be suppressed so that the elastic energy is now stored predominantly in stretching deformations of the filaments.

Based on this understanding, it makes intuitive sense that we should be able to shift the NA/A cross-over by adding a small set of extremely stiff and longer impurity filaments, or in other words, *polydispersity*. These stiffer and/or longer filaments are expected to act as local affine geometry enforcers smoothing out the spatial heterogeneities in the strain field and recruiting more of the network's filaments to carry elastic energy. In this way it is expected to see the addition of polydispersity to result in: (i) a large increase in the shear modulus, (ii) a transition of elastic energy from bending to stretching, and (iii) a decrease in some direct geometric measure of the non-affinity of the deformation field. In the work by Lin *et al.* [43], such experiments were performed. From the data on the nonlinear response of their system, it is clear that the addition of microtubules (much stiffer and longer than actin filaments) to NA F-actin networks shifts the mode of energy storage from bending to stretching. This may seem to be most easily interpreted as geometry driving mechanics — the microtubules indeed act to homogenize the spatial fluctuations in the strain field and thereby drive the system to an affine response. The numerical simulations of actin filament and microtubule network shown later in this chapter strongly support the observation of the shift in elastic energy storage from bending to stretching in response to the addition

of stiffer impurity filaments. However, it is found the geometry of the deformation field is not necessarily rendered more affine by the addition of the stiff impurity filaments. The simulation results, discussed in more detail below, may be summarized as follows: (i) It is found that the addition of microtubule-like impurities generically stiffens the network; (ii) The addition of the impurity filaments to NA networks acts generically to shift the elastic energy storage from bending to stretching modes in agreement with the work of Lin *et al.*; (iii) In the transition region between the NA and A regimes the impurities do indeed suppress the total geometric measure of non-affinity. Deep in the non-affine regime, however, these impurities actually enhance the geometric measure of non-affinity. Examining this in more detail, significant negative correlation is found between the local measures of impurity density and non-affine geometry. Yet, deep in the non-affine regime the stiff filaments act primarily to redistribute this non-affine deformation in space rather than to globally suppress it. Finally, we point out the method by which the stiff impurity filaments are mechanically coupled to the semiflexible network plays an important role to be discussed further below.

The fact that stiffer impurities stiffen even non-affine networks may appear trivial since such effects are well-known with regard to the addition of rigid impurities into elastic continua [81]. The theoretical analysis of this effect, however, relies on a gradient expansion of the elastic energy of the continuum material. Inasmuch as this gradient expansion fails dramatically in the NA regime, it is not *a priori* clear that the addition of stiffer impurities would have a similar effect on such networks. Our numerical simulations confirm that despite the inappropriateness of gradient expansion theories for non-affine networks, the stiffening phenomenology persists. This agreement notwithstanding, our results also suggest that geometry does not drive mechanics in the A/NA cross-over precisely as originally thought. While the impurities always enhance the shear modulus, they do *not* suppress purely geometric measures of non-affinity, particularly when deep in the NA regime. This suggests for the first time that there is some sort of decoupling between mechanics and the geometry of the deformation field in highly NA composite networks. The desideratum for affine deformation in such materials remains mysterious.

The remainder of this chapter is organized as follows. In Sec. 4.2 we discuss the numerical

finite-element model used to study the mechanics of semiflexible composite networks. There are many types of composite semiflexible networks that may be imagined. For example, we may consider networks in which the filaments are mechanically identical but not monodisperse in length. Or, we might consider networks of identical filaments linked by cross-linkers having different elastic compliances. Here we discuss only the form of heterogeneity motivated by the experiments of Lin *et al.* We present our results on the mechanics, energy storage, and deformation field geometry of the networks in Sec. 4.3. Finally, in Sec. 4.4 we discuss the implications of our work for cellular mechanics, the mechanical modification of synthetic fiber networks, and for more general questions of the elastic response of disordered solids. Part of the material in this chapter is from Bai *et al.* [44]

4.2 Model

Our model system is a two-dimensional network composed of two types of filaments, qualitatively representing a mixture of F-actin and microtubules. Filaments of the first type, which we term *soft matrix* filaments, are uniformly assigned a length L and bending and stretching moduli κ and μ respectively. We place these first filaments with uniformly distributed random positions and orientations in a square box of edge length W and area $A = W^2$. Intersecting filaments are rigidly pinned together at their crossing points, mimicking the effect of actin-binding crosslinking proteins. Within this soft network, we embed a second class of longer and stiffer *impurity* filaments with the same stretching modulus, μ but having increased length $L_I > L$ and bending modulus $\kappa_I > \kappa$. To represent the steric interactions of the impurities with the matrix, we rigidly crosslink stiff filaments at their intersections with soft filaments. However, bearing in mind the absence of microtubule-binding protein crosslinkers, we do *not* crosslink stiff filaments at their intersections with other stiff filaments. The key associated point is that the stress percolating network is formed chiefly by the soft matrix filaments, with the stiff impurity filaments acting only as locally stiff inclusions. The impurities alone do not form a load bearing network. An example network representative of the model is illustrated in Fig. 4.1, with the matrix filaments shown as thin blue lines and the impurities as thick red lines.

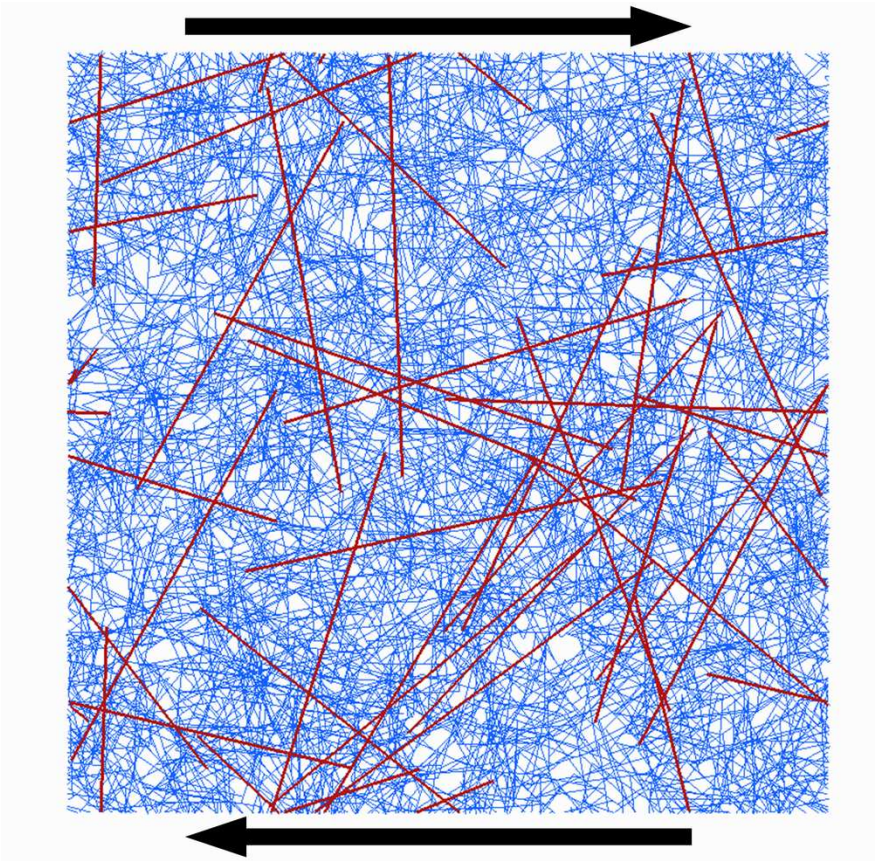

Figure 4.1: A typical polydisperse network showing the short, soft matrix filaments (thin blue lines) and long, stiff impurity filaments (thick red lines), with $L_I/L = 5$, $L/\lambda = 10$, and $n_I = 10.3$. Arrows indicate shear strain imposed through the periodic boundaries.

Apart from the system size W and filament length L, the soft matrix is characterized by two additional key length scales: the "bending length," $\ell_b = \sqrt{\kappa/\mu}$ describing the bending stiffness of individual filaments, and the average distance between cross-links, ℓ_c serving as an inverse measure of matrix density (more specifically, the density of matrix crosslinks). Previous work [35–37] has revealed that the A/NA transition in monodisperse networks is characterized by the non-affinity length, λ, which emerges as a function of ℓ_b and ℓ_c,

$$\lambda = \ell_c(\ell_c/\ell_b)^z. \tag{4.1}$$

with z empirically identified to be 1/3. With the addition of stiff impurities in this work, we track the composition of the resulting polydisperse networks by the number of impurities per unit area, denoted n_I. Accordingly, the mechanics of the composite network is characterized

by four parameters: the ratio of the matrix filament length to nonaffinity length, L/λ; the density of stiff impurities, n_I; the ratio of filament lengths, L_I/L; and the ratio of bending moduli, κ_I/κ. To simplify the our study of the model, we assume values for the last two parameters reflecting the properties characteristic of F-actin and microtubules. We set $L_I = 5L$ mimicking a network in which the stiffer microtubules are longer than the surrounding network of F-actin. Likewise, noting that the measured bending persistence length of microtubules is in the range 1–6 mm, and that of F-actin is about 17 μm, we set $\kappa_I = 250\kappa$. In the following section we examine the influence of the remaining two parameters, L/λ and n_I on the mechanics of composite networks.

4.3 Results

The primary mechanical signature of the transition from the A to the NA regime is the depression of the measured shear modulus, G, relative to the value for an affinely deforming network of the same density, G_{affine}. The latter can be derived analytically by considering the pure stretching of filaments under a prescribed affine strain, which after correcting for the non-stress-bearing ends of filaments dangling past the last crosslink, is given as [35, 36]

$$G_{\text{affine}} = \frac{\pi}{16}\frac{\mu}{L}\left(\frac{L}{\ell_c} + 2\frac{\ell_c}{L} - 3\right). \tag{4.2}$$

Throughout this chapter we compare the measured shear modulus of composite networks to the affine modulus of only the matrix.

Figure 4.2 shows the normalized network shearing modulus G/G_{affine} as a function of the density of impurities, n_I, as obtained from simulations with $L/\lambda = 1$, 10, and 25. These results confirm the expectation that, for an initially monodisperse soft matrix network nominally in the affine regime (*i.e.*, $G/G_{\text{affine}} > 10$) the addition of stiff impurities in any amount has little effect on the overall network stiffness. Specifically, the effect on the $L/\lambda = 25$ case, being well above the A/NA transition, is barely distinguishable.

Even near the A/NA transition at $L/\lambda = 10$ the effect of impurities on the modulus is minimal. However, in contrast to the insensitivity at large L/λ, addition of stiff impurities

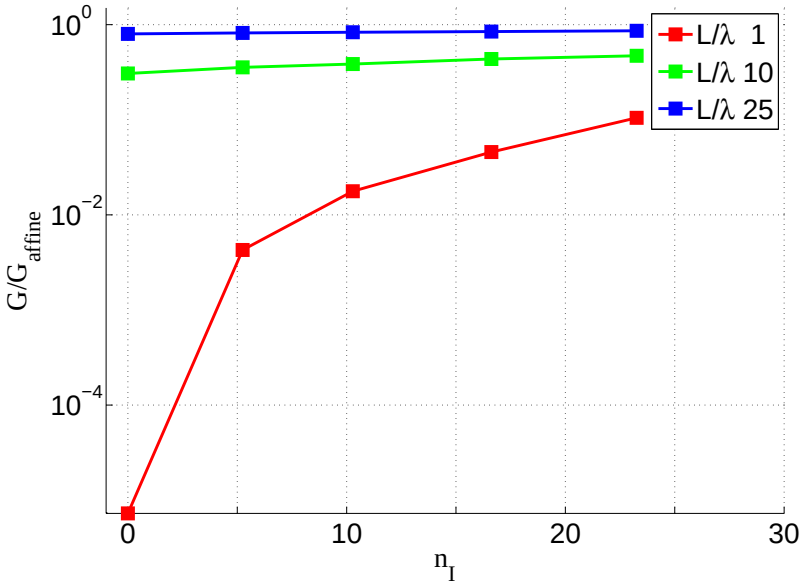

Figure 4.2: Normalized shear modulus G/G_{affine} versus impurity density n_I. The values of L/λ describe soft matrix networks that are well above (L/λ=25), near (L/λ=10), and well below (L/λ=1) the A/NA transition.

to a non-affine matrix ($L/\lambda = 1$ in Fig. 4.2) increases the modulus by more than four orders of magnitude. This effect is seen even for rather small numbers of impurities.

To understand the mechanism behind the dramatic stiffening effect of the impurities, we plot in Fig. 4.3 the fraction of energy stored in stretching of matrix filaments E^M_{stretch} relative to total matrix energy E^M_{total} as a function of n_I. Again for affine networks with $L/\lambda = 25$ there is no noticeable difference between the monodisperse soft network and the composite network with impurities: across the entire range of n_I nearly all of the energy is stored in stretching of matrix filaments, consistent with the interpretation of affine deformation. Near the A/NA transition at $L/\lambda = 10$, the stretching fraction drops to about 0.8, and begins to show a trend of increasing with impurity density. However, this effect is most pronounced well below the A/NA transition. At $L/\lambda = 1$, the addition of stiff impurities transforms heavily bending-dominated monodisperse network into a composite network where nearly all of the strain energy in the matrix is stored in the form of stretching. Remarkably, with the addition of even very small numbers of impurities (n_I=5) the stretching energy fraction

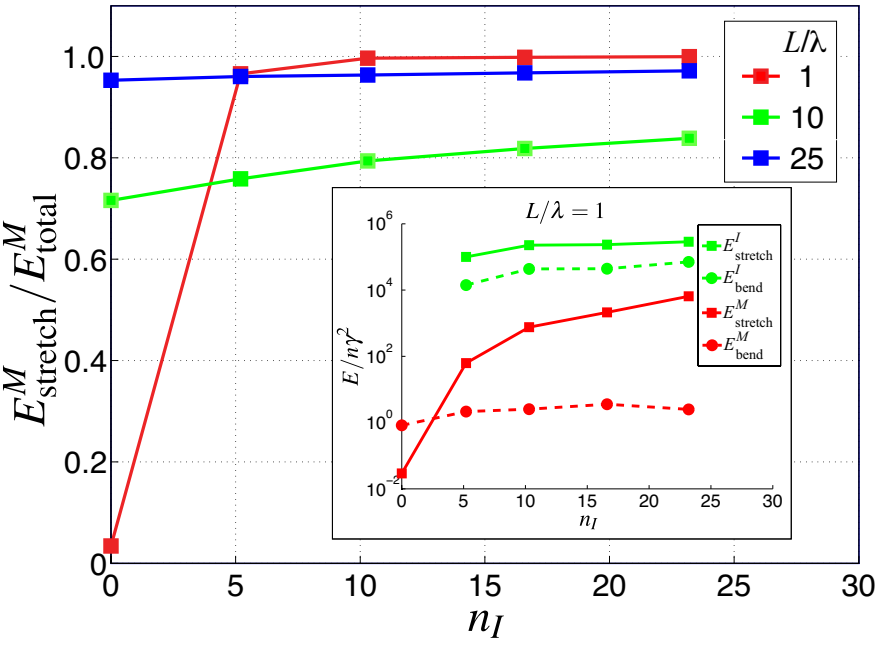

Figure 4.3: Distribution of strain energy *vs.* impurity density n_I. Main panel: energy fraction stored in stretching for soft matrix filaments alone, for $L/\lambda = 1$, 10, and 25. Inset: bending and stretching energies for matrix and impurities, as fractions of the total network energy for $L/\lambda = 1$.

in the nonaffine $L/\lambda = 1$ matrix surpasses that of the more affine $L/\lambda = 10, 25$ networks. To uncover in greater detail how impurities change the distribution of strain energy, we plot in the inset of Fig. 4.3 the amount of stretching and bending energy per filament, normalized by the shear strain γ^2, for both the impurity and matrix filaments. This reveals that the increase of the stretching to bending ratio in the matrix is associated primarily with a sharp increase of the matrix stretching energy, while the bending energy of matrix filaments remains nearly unchanged from its $n_I = 0$ value. Furthermore, the energies per filament of the impurities — which also remain roughly constant over the range of n_I — are greater than those of the matrix filaments. This reveals that the large increase in shear modulus demonstrated in Fig. 4.2 is attributable to an overall increase in the stretching energy of the network — stored in both the matrix and impurity filaments: as n_I increases, the bending of the weak matrix filaments is not suppressed, but rather augmented by additional stretching of the existing matrix along with the newly added impurities. Despite the fact that the impurities

do not form a self-supporting load bearing network, they are able to carry stresses mediated by their connectivity through the matrix.

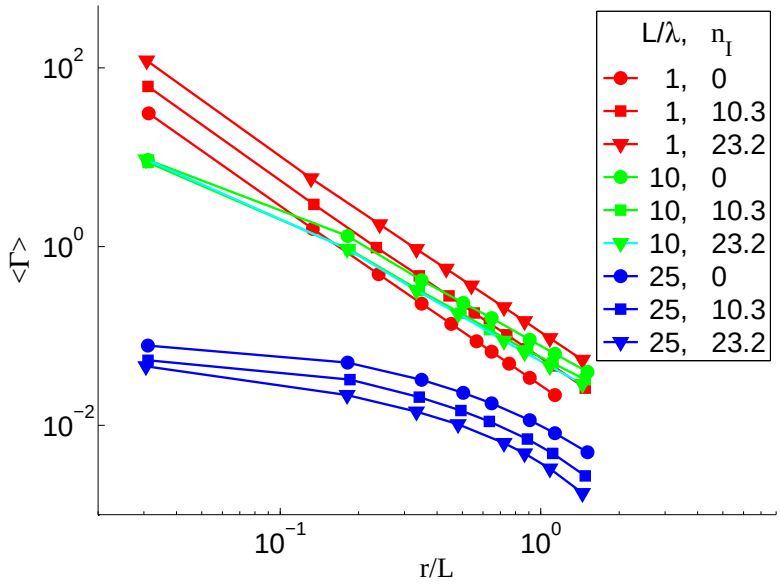

Figure 4.4: Nonaffinity normalized by overall shear strain $\Gamma = \langle(\Delta\theta)^2\rangle/\gamma^2$, plotted against point pair distance r normalized by short filament length L.

Previous studies of monodisperse networks have shown that the depression of G/G_{affine} with decreasing L/λ is correlated with (i) an increasing fraction of bending energy stored in the network, and (ii) increasingly non-affine deformation of the network. From the above discussion of Fig. 4.3 it is clear that the first of these correlations is not shared universally for polydisperse networks. This turns out to be the case for the second correlation as well. The non-affinity can be characterized quantitatively by the geometric measure $\langle\Delta\theta^2(r)\rangle = \langle(\theta - \theta_{\text{affine}})^2\rangle$, where $\theta(r)$ is strain-induced rotation of the vector connecting a pair of points separated by distance r, θ_{affine} is the rotation corresponding to an affine deformation, and the average is taken over all point pairs with separation r in a network. Dividing by the magnitude square of the shear strain, γ^2, we define the normalized geometric nonaffinity as $\Gamma(r) \equiv \langle\Delta\theta^2(r)\rangle/\gamma^2$. Figure 4.4 shows the geometric nonaffinity measurements for several of the combinations of L/λ and n_I shown in Figs. 4.2 and 4.3. As a function of L/λ the geometric nonaffinity shows the same trend as in monodisperse networks [35, 36]: for L/λ

above the A/NA transition (L/λ=25, blue curves), the nonaffinity gradually increases going to short distances but plateaus at a small value at short length scales, i.e. as $r/L \to 0$. In contrast, in NA networks the nonaffinity grows monotonically as r is reduced. Roughly speaking, this means that the closer one examines the deformation field the more nonaffine it appears. The behavior for intermediate values of L/λ near the A/NA transition essentially interpolates between that of the high and low values, pushing the plateau to smaller r/L values, and increasing the overall nonaffinity.

Figure 4.4 also shows that the qualitative L/λ dependence of the nonaffinity is unaffected by impurity density. The main effect of variation in n_I at fixed L/λ is to shift the $\Gamma(r)$ curves up or down. However, a close inspection reveals that the direction of this shift depends on L/λ. For the affine matrix with $L/\lambda = 25$, increasing n_I shifts $\Gamma(r)$ downward. Consistent with intuition, this shows that the addition of stiff impurities reduces the amount of bending making the already affine matrix even more affine. For the matrix near the transition with $L/\lambda = 10$, the same effect is evident, albeit much less pronounced. However, counter to intuition, the effect of adding impurities to the nonaffine matrix with $L/\lambda = 1$ is precisely the opposite: with increasing n_I the $\Gamma(r)$ curve shifts upward. This shift implies that impurities do not reduce, but rather *amplify* the nonaffinity of an already nonaffine matrix. Thus, when added to a softer network, impurities generally have the impact of *enhancing* the difference between affine and nonaffine deformation. Affine networks become more affine, and nonaffine networks become more nonaffine. The implication of this is unexpected based on our simple picture of the stiff filaments acting as local geometric regulators: an increase in the modulus with the addition of stiff impurities does *not necessarily* indicate a reduction in the degree of geometric nonaffinity and the bending of network filaments. In all previous studies on monodisperse networks, G/G_{affine} and Γ have been inversely correlated. However, here the addition of impurities to the nonaffine network with $L/\lambda = 1$ produces an appreciable increase in both G/G_{affine} and Γ. Hence, the relation between the mechanical and geometric measures of nonaffinity for generic networks is apparently more complex than heretofore believed.

To address the question of *how* impurities can enhance nonaffinity, the spatial distribution

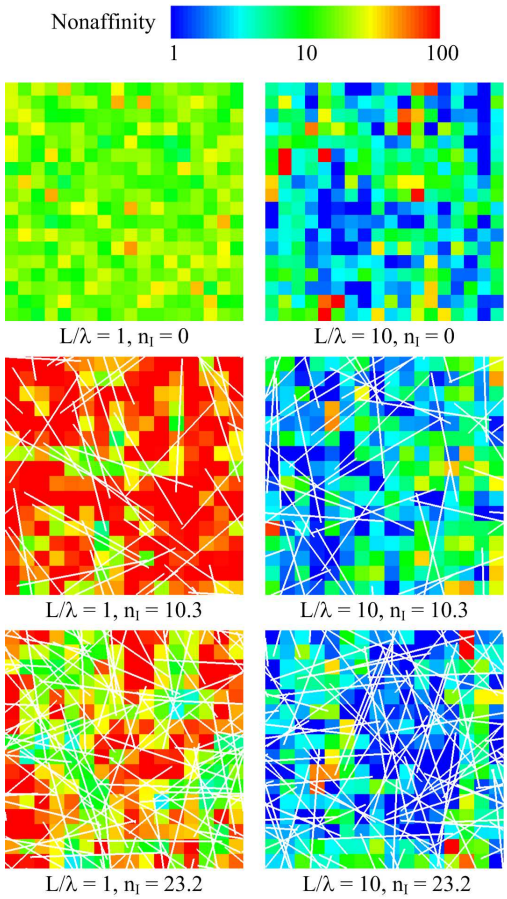

Figure 4.5: Spatial map of geometric nonaffinity, computed within each box as $\Gamma(r) = \langle \Delta\theta^2 \rangle / \gamma^2$, with the average taken over all point pairs with separation r in a box. The value of r used in this figure is $1.3\ell_c$

of Γ is examined. As shown in Fig. 4.5, the simulated networks are discretized with a 18×18 grid, and the nonaffinity of the matrix filaments is computed in each box of the grid as $\Gamma(r) = \langle \Delta\theta^2 \rangle / \gamma^2$, with the average computed by summing over all point pairs at some separation r within a box. The computed spatial map of nonaffinities is plotted in Fig. 4.5 for $L/\lambda = 1$ and 10, at three different impurity densities, with the impurity filaments overlaid as thick white lines. The nonaffinity maps of the polydisperse composite networks reveal a general pattern of low nonaffinity (blue boxes) in regions well populated by impurities, with the peaks of nonaffinity (red boxes) tending to the "gaps" between impurities. This pattern is prominent for the most nonaffine networks (L/λ=1), where the addition of impurities to the monodisperse matrix with a spatially uniform local nonaffinity measure leads to localization

of local nonaffinity in the gaps between impurities. When averaged over the whole sample, the net effect of this spatial rearrangement of the nonaffine deformation into the gaps between the stiff impurities it to actually increase the total value of nonaffinity at all length scales. For the L/λ=10 networks near the A/NA transition in the absence of impurities, the spatial heterogeneity of the local nonaffinity is greater than for the equivalent networks with L/λ=1. For these networks in the cross-over region between affine and nonaffine, the "corralling" of the local nonaffinity by the impurity filaments is not as pronounced — consistent with weak overall quantitative variation of $\Gamma(r)$ with n_I shown in Fig. 4.4 — but the remains qualitatively similar.

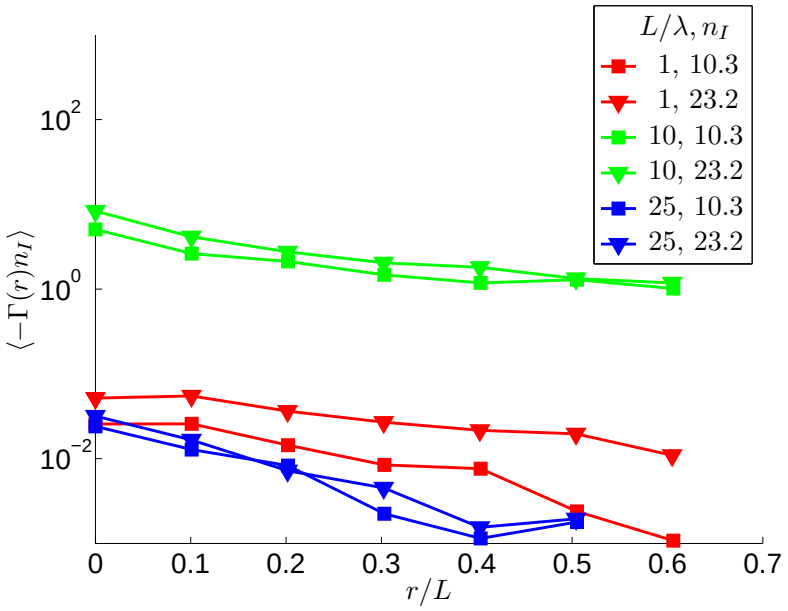

Figure 4.6: Nonaffinity-impurity density correlation

This localization of nonaffinity due to the introduction of impurities can be explored in a more quantitative manner by examining the spatial correlation function of the local measure of geometric nonaffinity Γ with the local length density (i.e. length per unit area) of the stiff impurity filaments. This function is shown in Fig. 4.6. There is a significant negative spatial correlation between the nonaffinity and impurity density. The correlation length appears to be roughly constant over the entire range of L/λ and n_I, suggesting that it is set by L, the length of the filaments making up the softer semiflexible matrix

into which the impurities are embedded. Interestingly, the magnitude of the anticorrelation varies by two orders of magnitude as one passes through the A/NA transition. Deep in the NA regime where the nonaffinity is large, and deep in the A regime where it is small, the local effect on the geometric nonaffinity due to the introduction of a few stiff filaments is approximately one hundred times weaker than it is in the transition region ($L/\lambda \sim 10$) between these two regimes. While this is reminiscent of a second order phase transition where the susceptibility of order parameter field to its conjugate variable diverges at the critical point, the dramatic enhancement of the susceptibility of the local nonaffinity to the presence of the stiff filaments cannot be understood in this way. Specifically, there is no diverging correlation length associated with the cross-over as seen the spatial dependence of the correlation functions in the A, NA, and cross-over regimes. Instead, in the cross-over regime the system can be locally coerced into affine deformation by the impurities more readily than it can in either the NA or A regimes, but the spatial extent of this coercion is in all cases fixed by the microscopic length scale in the problem — the length of the filament — and no cooperative enhancement of the nonaffinity reduction occurs due to the interactions of the (softer) filaments of the network.

Finally, it is noted that the details of how the impurity filaments are coupled to the matrix of soft semiflexible filaments plays an important role in the mechanics of the network and in the partitioning of elastic energy between bending and stretching modes in it. In the two-dimensional simulations the impurity filaments are necessarily cross-linked into the network. They are not allowed to be crosslinked to each other so that the stiff filaments cannot form a stress-bearing network at any area density. Nevertheless, as shown in Fig. 4.3, the impurities can store both stretching and bending energy. In contrast with three dimensional networks, such as those explored by Lin and collaborators, the microtubules may simply be embedded into the network of F-actin and have only steric interaction with that network. In this case the stiff microtubules can support bending stresses but not tensile/compressive ones. To examine in our two-dimensional simulation the importance of storing tensile stress in the stiff impurity filaments, we re-examined the same networks described above, but with the extensional modulus of the impurity filaments artificially set to zero (still keeping their

bending moduli fixed). We found that while addition of impurities still produced an increase in matrix stretching energy with no change in matrix bending energy, the effect was greatly reduced — so much so that bending remained the dominant mode of energy storage in the matrix. This demonstrates that build-up of tensile stress in impurities strongly enhances the shift in the balance of elastic energy from the bending to the stretching modes of the soft matrix filaments (i.e. the F-actin).

4.4 Discussion

Biopolymer networks of microtubules and F-actin provide an interesting testing ground for the study of the mechanics of heterogeneous semiflexible networks. Understanding this system has important implications for the long-term goal of determining the relationship between the microstructure and mechanics of the cytoskeleton of living cells. More generally, these composite systems of stiff impurities in a background of cross-linked semiflexible filaments provides a new way to study the A/NA cross-over. Can the stiff impurities be considered merely as extra geometric constraints that enforce affine deformation in a nominally nonaffine network? Will these impurities have a significant effect on the mechanical moduli of the network and what is the impurity concentration dependence of these mechanical effects?

It is shown that in a simple model system the effect of the introduction of a small number of stiff impurity filaments can dramatically increase the shear modulus of the network in the nonaffine regime and shift the elastic energy storage from being primarily in the bending of the filaments to their stretching. In affine networks the addition of impurities increases the collective shear modulus of the network linearly in the impurity density. This linear dependence holds even in the transition region between A and NA networks. Deep in the NA regime we find that the introduction of a low density of impurities produces an increase in the shear modulus of over four orders in magnitude that is *nonlinear* in the impurity number density. Moreover, when the impurity filaments can store tensile stress they shift the elastic energy storage of the network from bending to stretching modes.

These points appear to support the simple intuitive notion that the introduction of the stiff impurities act as extra geometric constraints forcing the nominally nonaffine network to deform in an affine manner. This simple interpretation, however, is shown to be incorrect by the direct examination of the geometry of the deformation field in these composite networks (comprised by the softer semiflexible filament network and stiffer impurities). The geometric measure of nonaffinity in all cases studied, affine networks, highly nonaffine networks, and ones in the transition region between these two extremes, varies very little in response to the introduction of the impurities. Rather, the impurities have the effect of redistributing spatially the nonaffinity in the deformation field in such a way as to only weakly change its spatially integrated value. Thus, we refer to the action of the impurities as merely corralling rather than suppressing geometric nonaffinity in the composite network. This corralling effect is due to the fact that the effect of an impurity filament is primarily to locally suppress nonaffine deformations by moving such nonaffinities away from it. The magnitude of the change in local nonaffinity around an impurity filament depends strongly on L/λ, having a strong maximum in the transition region between A and NA networks – $L/\lambda \approx 10$. The range of this effect, however, is controlled by the length of the soft semiflexible filaments making up the network and appears to be independent of both the density of impurities and nonaffinity length λ. More work needs to be done to better understand the local response of the network to the introduction of the impurity.

A sufficient number of impurities then will force the nonaffinity into small areas of the network. This point has important implications for the particle tracking experiments designed to explore the geometry of the deformation field in heterogeneous semiflexible networks. The introduction of stiff impurities may make the network appear to deform affinely if the system's deformation field is not resolved at a sufficient level of spatial resolution since the regions of nonaffine deformation should become localized in the network.

The principal point of contact of this work to the experiments of Lin and collaborators is found in the effect of the impurities upon the balance of elastic energy storage between the bending and stretching modes of the soft semiflexible network. The simulation results show that in non-affine networks the impurities, even at very low concentrations shift the

energy storage from bending to stretching. The interpretation of the appearance of nonlinear stress hardening in the nonaffine F-actin networks with embedded (stiff) microtubules is that the microtubules are shifting the elastic energy from F-actin bending to stretching. This is clearly consistent with our results, but, as discussed above not necessarily an indication that the global level of bending and nonaffine deformation has been reduced in the system.

In order to shift the energy storage in NA networks from bending to stretching by the introduction of stiff impurities, it is found to be necessary that there be some sort of mechanical linkage between the microtubules and the F-actin so that these stiff impurities can store tension. When the storage of tensile stresses in the impurities is prevented, as might be expected for impurities that have only steric interactions with the softer matrix, the increase in matrix stretching energy was less dramatic. We suppose that while the onset of stress hardening may require an increase in the amount of stretching energy in the network, it may not be necessary for the stretching energy to dominate over bending energy. Perhaps the smaller increases in actin stretching consistent with microtubules (under zero tension) could be sufficient to trigger nonlinear strain hardening. If so, we suspect that the presence of crosslinks between the microtubules and the surrounding F-actin network should significantly increase the effect of these impurities on the nonlinear elastic response of the composite network. It remains for future work to examine to this hypothesis using three-dimensional models with purely steric and crosslinked couplings of the impurities to the matrix.

CHAPTER 5

Anisotropy and Buckling

5.1 Introduction

The previous two chapters are focused on the mechanics of statistically *isotropic* filament networks. In this chapter, the mechanics of anisotropic semiflexible networks is studied. There are two main motivations for this study. Firstly, it is found that cellular cytoskeletal networks are sometimes dominated by oriented stress fibers and can thus be anisotropic [82]. Applying the emerging understanding of semiflexible network mechanics to cells therefore demands that we confront such lower symmetry problems. Secondly, recall that in isotropic, monodisperse semiflexible networks, there's one single length scale, the nonaffinity length λ, which controls the network's nonaffine-affine crossover. Then there are basic questions that we seek to answer related to the effect of a broken rotational symmetry on the nonaffine-affine crossover and to the mechanics of the system in the nonaffine regime.

Anisotropic networks are characterized by two parameters: a filament density, same as isotropic networks, and a nematic order parameter S, which characterizes network's nematic anisotropy. It is found that for all values of the nematic order parameter, the network undergoes an affine to nonaffine crossover as network density is reduced. Previous work on the affine to nonaffine crossover in isotropic networks showed that there is a single control parameter for the crossover, L/λ, where the nonaffinity length λ is a function of both the filaments' mechanical properties and the network density; λ does not reflect the orientational order of the filaments. It will be shown later in this chapter that, for highly anisotropic networks, L/λ does not alone determine the elastic constants of the system in the linear response regime. While this finding by itself is not surprising, it is also found that the linear

response regime narrows dramatically for highly ordered networks, causing the shear response at finite strain to develop a more complex dependence on the shearing direction than can be understood in terms of the symmetries of the elastic constant tensor for a orthotropic solid. This finding emphasizes the inapplicability of linear continuum elasticity theory in the simultaneous limits of large orientational order and nonaffinity. In other words, these nonaffine anisotropic networks do not behave as some orthotropic solid with redefined elastic constants. The source of this strong nonlinearity is related to the vanishing of the linear elastic response regime of a perfectly aligned filament system and, for disordered but nematic networks, can be understood in terms of cooperative bending and then Euler buckling closely related to the "floppy modes" analysis of Heussinger and Frey [38]. Part of the material in this chapter is based on the work by Missel *et al.* [42]

5.2 Network Model and Analytical Prediction

Similar to the simulations discussed in prevoius chapters, a two-dimensional filament networks is studied, which is composed of identical filaments of length L and having bending and stretching moduli κ and μ respectively. To produce a system of N filaments with statistically uniform density and filament anisotropy characterized by nematic order parameter S, one endpoint of each filament was laid down at random in a square box of edge length W and area $W^2 = A$, and assigned an orientation chosen from the distribution $P(\theta)$ with respect to nematic direction $\hat{n}$. Intersections between crossing filaments are treated as rigid ties (crosslinks), as discussed in Sec. 2.1.4. Filaments are added until the system reaches the selected density. A representative example of such a network, a magnified region thereof, and the distribution of filament angles are shown in Fig. 5.1. The filaments are discretized such that nodes were placed at all crosslink locations and also at regular intervals between crosslinks to allow for bending.

The networks are characterized by a nematic order parameter S and a filament density, measured in terms of the mean distance between cross-links along a filament, ℓ_c. The mechanics of the monodisperse filaments is set by $\ell_b = \sqrt{\kappa/\mu}$. Finally, all energy scales are set by a single filament elastic modulus and all moduli in this chapter are measured in terms of

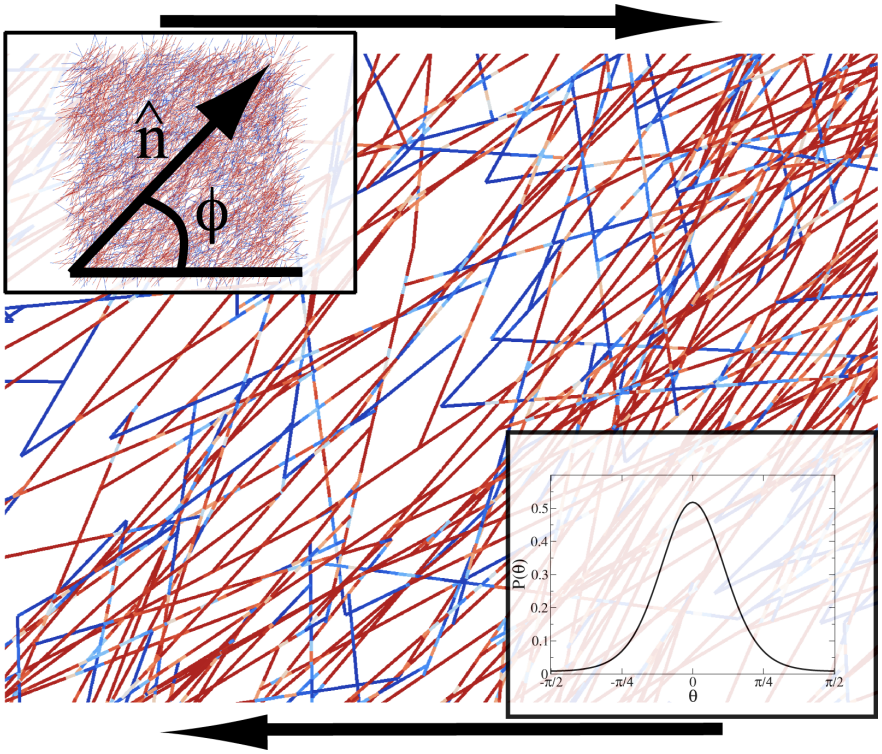

Figure 5.1: Top left: A typical nematic network with diagram defining the shear orientation angle ϕ. Bottom right: The angular distribution $P(\theta)$ of filament orientations relative to the nematic director. Center: A closeup of a network (shear direction indicated by arrows) showing the partitioning of elastic energy into filament stretching (red) and bending (blue).

μ.

For a given $P(\theta)$, the nematic order parameter is defined as $S = \int_{-\pi}^{\pi} d\theta\, P(\theta) \cos 2\theta$ describes the degree of anisotropy; $S = 0$ corresponds to an isotropic system, and $S = 1$ is a system with all filaments aligned. We compute the mean distance between crosslinks from the filament density $\rho = N/A$ using the following method, which is a generalization of the method employed by Head *et al.* for isotropic systems [35]. Consider a straight filament lying at an angle θ with respect to the nematic director. Given a second filament at some angle ψ with respect to the first, the probability of their crossing is $L^2|\sin\psi|/A$. Integrating over ψ with a weight $P(\theta + \psi)$ we find that the mean number of filaments crossing the original one

lying at angle θ with respect to $\hat{n}$ is Poisson distributed with mean

$$n_c(\theta) = 2\rho L^2 \int_0^\pi d\psi \, \sin\psi \, P(\theta + \psi). \tag{5.1}$$

Integrating over the orientation of the original filament, we find that the mean distance between cross-links is given by

$$\ell_c = L \, \frac{1 + \langle e^{-n_c} \rangle - 2\left(\left\langle \frac{1}{n_c} \right\rangle - \left\langle \frac{e^{-n_c}}{n_c} \right\rangle \right)}{\langle n_c \rangle - (1 - \langle e^{-n_c} \rangle)}, \tag{5.2}$$

where the angle brackets denote averaging over θ with weight $P(\theta)$. More details of the derivation of ℓ_c and G_{affine} can be found in Appendix B. For an isotropic gel, Head *et al.* found that nonaffine to affine (NA-A) crossover is controlled by L/λ where $\lambda = \ell_c(\ell_c/\ell_b)^z$ with $z = 1/3$ [35]. Scaling arguments [35] and mean field theories [69] suggest $z = 2/5, 1/4$ respectively. Although for anisotropic networks, it needs to be seen whether the NA-A crossover can still be characterized by L/λ, this work just follows Head *et al.*, and uses $z = 1/3$ to calculate λ throughout this dissertation. Note that λ is built up from ℓ_b, which is a function only of the filaments' mechanics, and ℓ_c, which is a function only of network density.

Two-dimensional elastic continua with nematic order (i.e. broken rotational symmetry) may be characterized by four independent elastic constants [83]. Writing the energy density U in terms of strain u_{ij}, we have $U = \frac{1}{2} C_{ijkl} u_{ij} u_{kl}$ [84]. The elastic stiffness tensor C_{ijkl} can be identified in terms of its four independent components as C_{1111}, C_{2222}, C_{1212}, and C_{1122}. To find out the expression of C_{ijkl} for the network, we have to start with analyzing a single filament. Consider a single filament in the network with direction $\hat{e}(\theta)$, which means its direction is oriented at angle θ. If deformation field is affine, the filament's strain energy will solely be stored in stretching along $\hat{e}(\theta)$. Since u_{ij} is in the global coordinate system, it has to be transformed to a rotated coordinate system with angle θ as follows

$$u_{ij}(\theta) = \begin{bmatrix} \cos\theta & \sin\theta \\ -\sin\theta & \cos\theta \end{bmatrix} \begin{bmatrix} u_{11} & u_{12} \\ u_{21} & u_{22} \end{bmatrix} \begin{bmatrix} \cos\theta & -\sin\theta \\ \sin\theta & \cos\theta \end{bmatrix} \tag{5.3}$$

Note that only the $u_{11}(\theta)$ is of interest which represents the stretching strain of the filament, all the other components are irrelevant. Also noting that $\hat{e}(\theta) = [\cos\theta, \sin\theta]$, filament's

strething strain, $u_{11}(\theta)$, can be written as

$$u_{11}(\theta) = \hat{e}_i u_{ij} \hat{e}_j \tag{5.4}$$

Now, the energy density of the filament network can be written in terms of filament stretching energy as

$$U = \rho \int_0^{2\pi} d\theta \, P(\theta) \frac{1}{2} \mu (\hat{e}_i u_{ij} \hat{e}_j)(\hat{e}_k u_{kl} \hat{e}_l) \sum_{n=2}^{\infty} p_n(\theta) L \frac{n-1}{n+1} \tag{5.5}$$

where n is the number of cross-links per filament, is summed over using their Poisson distribution $p_n(\theta)$. From the definition of elastic stiffness tensor $C_{ijkl} = \partial U / \partial u_{ij} \partial u_{kl}$, the components of elastic stiffness tensor C_{ijkl} can be calculated in the following equation, where they are all linearly proportional to the stretching modulus μ of the constituent filaments

$$C_{ijkl} = \mu \rho \int_0^{2\pi} d\theta \, P(\theta) \hat{e}_i \hat{e}_j \hat{e}_k \hat{e}_l \sum_{n=2}^{\infty} p_n(\theta) L \frac{n-1}{n+1}, \tag{5.6}$$

This work is focused exclusively on the shear modulus $G(\phi)$, which is dependent on ϕ, the *shear orientation angle* between the displacement and nematic directions as shown in Fig. 5.1. For a given ϕ, using Eq. (5.6), G takes the form of

$$G_{\text{affine}}(\phi) = G_{\text{affine}}(0) \left[1 - 8 \sin^2 \phi \cos^2 \phi \right] + \Gamma \sin^2 \phi \cos^2 \phi \tag{5.7}$$

with

$$\begin{aligned} G_{\text{affine}}(0) &= \mu \rho L \int_0^{2\pi} d\theta \, P(\theta) \sin^2 \theta \cos^2 \theta \sum_{n=2}^{\infty} p_n(\theta) \frac{n-1}{n+1}, \\ \Gamma &= \mu \rho L \int_0^{2\pi} d\theta \, P(\theta) \sum_{n=2}^{\infty} p_n(\theta) \frac{n-1}{n+1}. \end{aligned} \tag{5.8}$$

We refer to the above as the affine prediction for the shear modulus of our anisotropic solids. The angular dependence of $G_{\text{affine}}(\phi)$ has a simple interpretation. A shear deformation with displacement along $\hat{x}$ is, to linear order, equivalent to stretching and compressing along the $\pm\pi/4$ directions with respect to $\hat{x}$. Filaments oriented at angles $\pm\pi/4$ with respect to $\hat{x}$ will be stretched/compressed along their axes, and thus have the most strain energy. Thus networks sheared so that the displacement and nematic director are separated by these angles will have maximal shear moduli.

5.3 Results

The depression of the shear modulus G below its affine value G_{affine} serves as a mechanical measure of the departure from affinity. Geometric measures of this departure [35,85] measure the spatial heterogeneity of the strain field as a function of length scale. Following Head *et al.* [35] we adopt our geometric measure of nonaffinity as $\Delta(r) = \langle(\omega - \omega_{\text{affine}})^2\rangle(r)$, where ω is the strain-induced change in angle between an arbitrary axis and the line joining two network points separated by a distance r, ω_{affine} is the change of this angle given purely affine deformations, and the average is taken over all point pairs with separation r in a network.

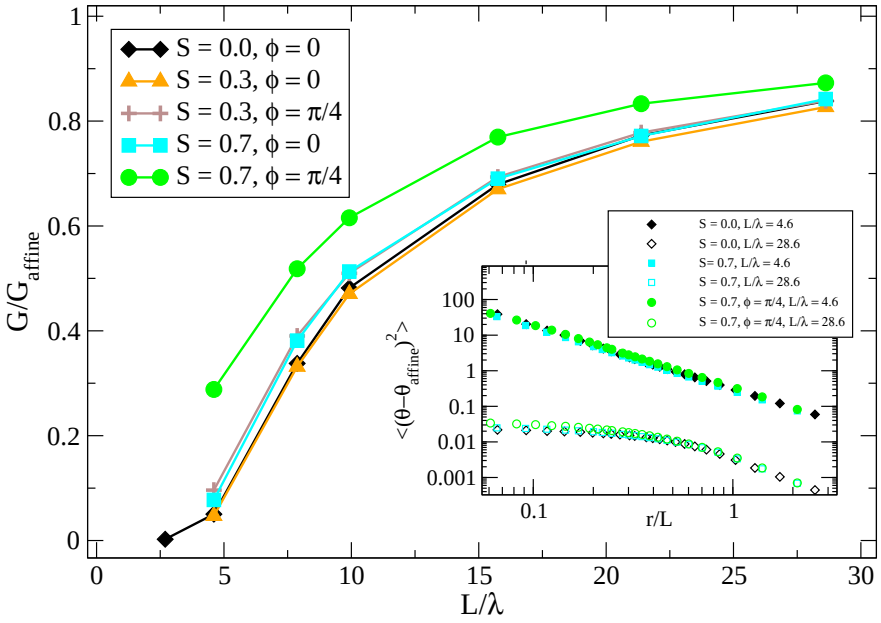

Figure 5.2: Normalized shear modulus $G(\phi)/G_{\text{affine}}(\phi)$ versus L/λ for varying degrees of anisotropy S and shear orientation angle ϕ. For highly anisotropic and nonaffine networks there is a large shear orientation angle dependence to the deviation from the affine shear modulus prediction. G was determined by fitting a three parameter polynomial function to the energy vs. shear data. Inset: The geometric nonaffinity measure Δ as a function of length scale for six different cases, including the $S = 0.7$ network at various values of ϕ, showing that Δ, unlike the modulus, is insensitive to the shearing angle.

Given that λ contains no information regarding the orientational order of the filaments,

one may ask whether the data collapse of the shear modulus for isotropic networks in the linear response regime that results from rescaling the filament length L by λ still applies to nematic networks. In this linear response regime we find that the data collapse is violated, suggesting that there are now additional length scales in the collective mechanics of the network. Fig. 5.2 plots the normalized shear modulus $G(\phi)/G_{\text{affine}(\phi)}$ as a function of L/λ for various values of S and ϕ. The shear modulus of presumably affine networks ($L/\lambda > 15$) nearly saturates the affine prediction and has a shear orientation angle dependence as predicted by the affine theory, as can be seen by the near-collapse of the ratios $G(\phi)/G_{\text{affine}}(\phi)$ for various values of ϕ in the affine regime. Deep in the nonaffine regime, however, the measured shear modulus of highly anisotropic networks ($S = 0.7$) varies more strongly with ϕ than can be understood by the affine theory. Interestingly, the direct geometric measure of the nonaffinity observed in the deformation fields of the networks (see inset of Fig. 5.2) does *not* appear to depend on S or on ϕ.

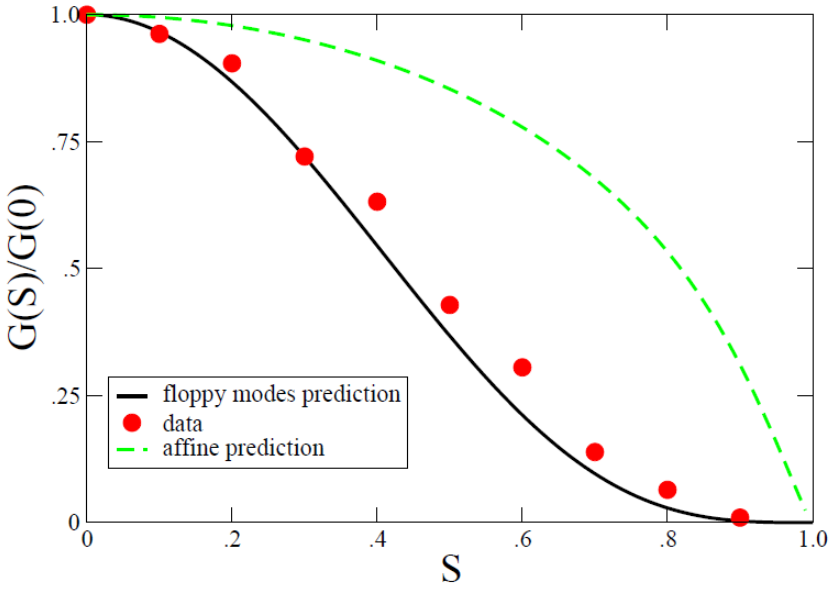

Figure 5.3: Shear modulus as a function of the nematic order parameter S (for fixed filament density) normalized by its value at $S = 0$. The gel with $S = 0$ has $L/\ell_c \simeq 25$ and $L/\lambda \simeq 5$, and all gels have $\phi = 0$. Gels were sheared up to $\gamma = .001$.

To understand the mechanics of anisotropic networks deep in the *nonaffine* regime, we

turn to an extension of the "floppy modes" model of Heussinger *et al.* [38]. This model assumes that the deformation energy is stored predominantly in filament bending. Considering a simply-supported beam with point load F at the center where a maximum deflection of δ_c is generated, its bending stiffness k_b is defined as F/δ_c. Using classical beam theory, $k_b \simeq \frac{EI}{L^3}$, where $EI = \kappa$. Thus, for a filament segment of length ℓ, it bending energy is $E_{\rm bend} \simeq \kappa\delta_{\rm na}^2/\ell^3$, where $\delta_{\rm na}$ is the typical size of axial displacements, and can be estimated to be approximately δ_c. From this relation it is clear that short filament segments are less compliant to bending than longer ones. Under deformation, we expect that the bending of one filament induces bending in filaments to which it is crosslinked; thus, network deformations in the nonaffine regime generate bends on all length scales down to some minimum length $\ell_{\rm min}$ at which the bending compliance of short segments becomes too low. To determine self-consistently this length, one notes that by energy minimization the bending energy stored in these smallest segments equals that of the surrounding network.

We adapt these ideas to the nematic networks by considering an idealized anisotropic gel with two classes of filaments: (i) *nematic* filaments oriented at $\theta = 0$ and (ii) *impurity* filaments oriented at $\theta = \pi/2$. The fraction of nematic filaments $2S-1$ is set to reproduce the correct nematic order parameter. Now the balance of energy of nematic filaments with their impurity neighbors and impurity energy with nematic neighbors results in two equations that must be solved simultaneously:

$$\begin{aligned} \frac{\kappa\delta_{\rm na}^2}{\ell_{\rm min,N}^3} &= n_{c,I}\int_{\ell_{\rm min,I}}^{\infty} d\ell_I\, P(\ell_I)\frac{\kappa\delta_{\rm na}^2}{\ell_I^3} \qquad \text{and} \\ \frac{\kappa\delta_{\rm na}^2}{\ell_{\rm min,I}^3} &= n_{c,N}\int_{\ell_{\rm min,N}}^{\infty} d\ell_N\, P(\ell_N)\frac{\kappa\delta_{\rm na}^2}{\ell_N^3}, \end{aligned} \tag{5.9}$$

where $P(\ell)$ is the distribution of segment lengths nematic (N) and impurity (I) filaments. The solution, as in the isotropic case, gives $G \sim \rho^7$, but also predicts the dependence of the shear modulus on S in the nonaffine regime. In Fig. 5.3 the anisotropic floppy mode theory (sold line) agrees well with the simulation data (red dots), while the affine prediction (green dashed line) does not.

We now turn to the *nonlinear* response of anisotropic networks in the nonaffine regime. Fig. 5.4 plots the difference between G measured at $\phi = \pi/4$ and $\phi = -\pi/4$ at $\gamma = 0.001$ as

a function of L/λ for a network with $S = 0.7$. G_γ is computed as the second derivative of the energy density with respect to γ. As these two orientations are equivalent under a mirror reflection, according to continuum linear elasticity ΔG_γ should vanish at suitably small strains. Indeed it does so as we reach the affine regime ($L/\lambda \gg 1$). For nonaffine networks, however, the range of strains over which linearity holds becomes exceedingly small, such that ΔG_γ is large even at strains as small as 0.1%. Examining Fig. 5.5(a) we see the origin of this particular deviation from continuum linear elasticity for nonaffine gels ($L/\lambda = 7.9$): the modulus for $\phi = -\pi/4$ (dotted black line) monotonically softens relative to that of $\phi = \pi/4$ (solid black line) as γ increases. This indicates that ΔG_γ increases with γ, demonstrating that it is an inherently nonlinear effect. For an affine network ($L/\lambda = 29$) these two shear moduli (green solid and dotted lines) are equal for all strains explored showing that affine networks have a significantly larger linear response regime.

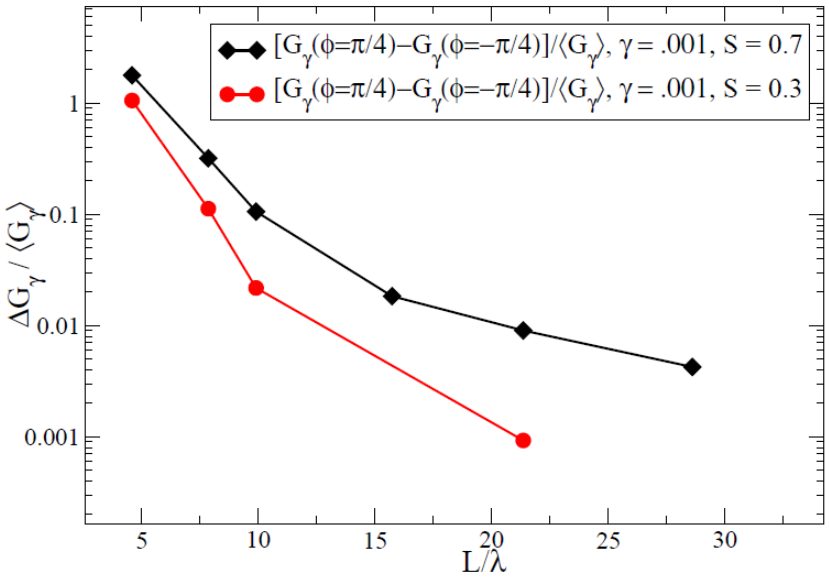

Figure 5.4: Difference in G for $\phi = \pm\pi/4$ at $S = .7$ as a function of L/λ. The shear modulus was measured strain $\gamma = .001$.

The nonlinearity that leads to the difference ΔG_γ was hypothesized to be due to cooperative Euler buckling of the network that leads to the nonlinear softening of the shear modulus at $\phi = -\pi/4$. As shown in Fig. 5.6, with the network orientation being $\phi = -\pi/4$ relative to

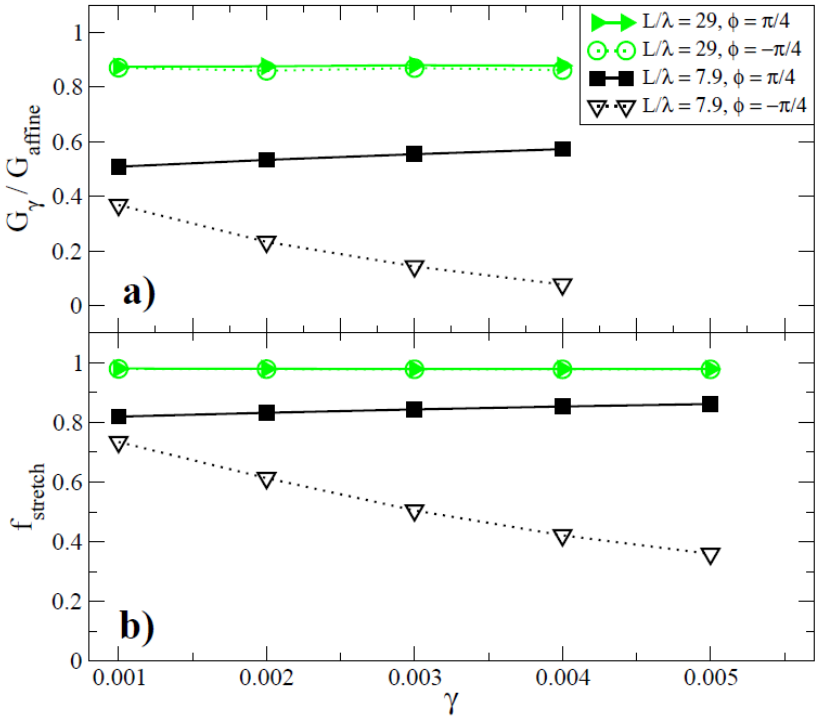

Figure 5.5: (a) G/G_{affine} vs. γ for $S = .7$ for various values of L/λ and ϕ; (b) Fraction of energy in stretching as a function of shear for the same networks.

the shearing direction, more filaments in nematic order are placed under compressive stress, whereas in network of $\phi = \pi/4$, only a few impurity filaments are under compression. Moreover, these nematic filaments in $\phi = -\pi/4$ network have larger values of ℓ_c, which allows for buckling at smaller strains.

To demonstrate the buckling hypothesis, in Fig. 5.5(b) the fraction of elastic energy stored in stretching is plotted as a function of both strain and L/λ. In the nonaffine regime ($L/\lambda = 7.9$), there is generically a smaller fraction of elastic energy stored in stretching, as expected from previous work, but the fraction of stretching energy decreases dramatically with strain as the network is sheared at angle $\phi = -\pi/4$ (dotted black line) applying compressive stresses to the filaments along $\hat{n}$. Shearing along $\phi = \pi/4$ puts the nematically aligned filaments under tension. The filaments now under compression are generically cross-linked on a much finer scale so that the network now collectively resists buckling.

This mechanism suggests that, for fixed L/λ and ϕ, the nonlinear response of semiflexible

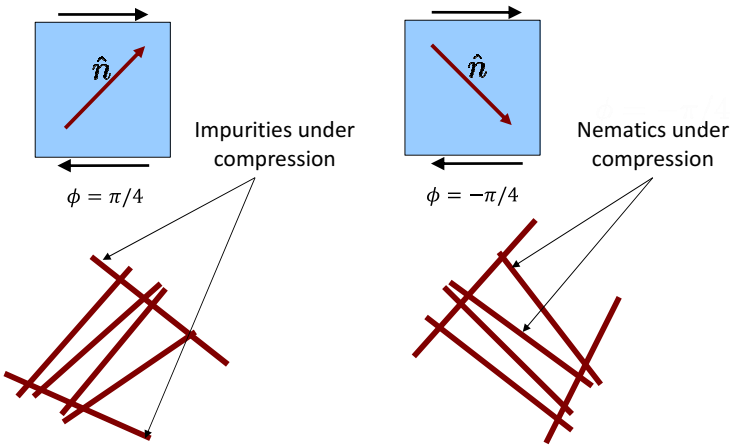

Figure 5.6: Schematic representation of hypothesis that more filaments in $\phi = -\pi/4$ networks are under compression and easier to buckle because of longer ℓ_c, compared with network of $\phi = \pi/4$.

gels should become more pronounced with increasing S. We have found that this is indeed the case, as can be seen in Fig. 5.7, which shows both G/G_{affine} and the fraction of energy in stretching for gels with $L/\lambda = 7.9$ and $\phi = -\pi/4$ for various values of S. As S increases, the filaments along the nematic direction (which are under compression for $\phi = -\pi/4$) become more sparsely crosslinked and are thus more easily buckled, leading to a decrease in the linearized G (Fig. 5.7(a)) and in the fraction of energy stored in stretching (Fig. 5.7(b)).

Similar to Conti and Macintosh's measure [86], define a relative importance measurement of buckling with respect to affine deformation B,

$$B = \frac{\Delta E_c}{\Delta E_{tot}} / \frac{\Delta E_{c,\text{affine}}}{\Delta E_{tot,\text{affine}}}, \tag{5.10}$$

where E_c is the compressive energy, E_{tot} is the total energy including both compressive and bending, $E_{c,\text{affine}}$ and $E_{tot,\text{affine}}$ have the same meaning and are taken by assuming affine deformation of the network. The energy difference (Δ) is taken between two shear steps. This way, $\frac{\Delta E_c}{\Delta E_{tot}}$ is a measure of buckling event between shear steps and is always smaller than 1. Since there is only compressive (or tensional) energy in affine deformation, $\frac{\Delta E_{c,\text{affine}}}{\Delta E_{tot,\text{affine}}}$ will always be greater than $\frac{\Delta E_c}{\Delta E_{tot}}$, so that B is always smaller than 1.

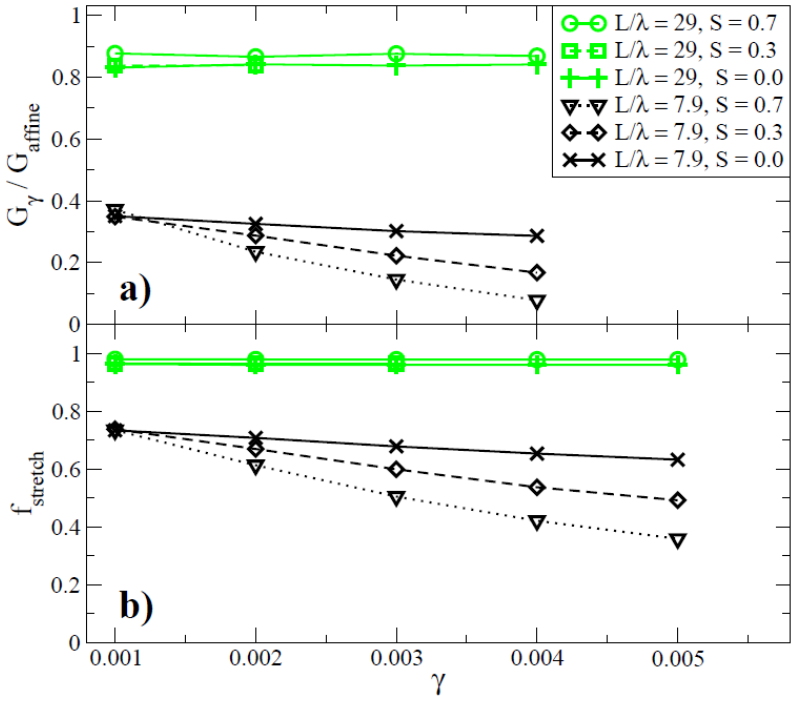

Figure 5.7: (a) G/G_{affine} vs. γ for $L/\lambda = 7.9$ and $\phi = -\pi/4$ for various values of S; (b) Fraction of energy in stretching as a function of shear for the same networks.

It is intuitive to think that buckling of filaments is a chain reaction, such that one buckled segment will generate a soft region and cause its adjacent segments more likely to buckle as well. To investigate whether that is true, the spatial correlation of the buckling order parameter B is calculated. Firstly, filament networks are divided into equally-sized square boxes and each box has a unique position (x, y); Secondly, the buckling order parameter $B(x, y)$ is computed for each box with coordinates x and y; Thirdly, spatial correlation function $\boldsymbol{B} = \langle (1 - B - < 1 - B >)^2 \rangle$; Lastly, $\boldsymbol{B}$ is plotted as function of positions, (x, y) at different shear. Fig. 5.8 shows the the spatial correlation of $\boldsymbol{B}$ for an isotropic network, in which buckling events have a clear spatial correlation along the $\phi = -\pi/4$ direction. Fig. 5.9 shows the spatial correlation of $\boldsymbol{B}$ of an anisotropic network, with clearly increaing spatial correlation over increasing shear strain. It can also be seen that the correlation is more pronounced than the previous isotropic case.

We can estimate the critical strain γ_c at which we expect to observe buckling leading

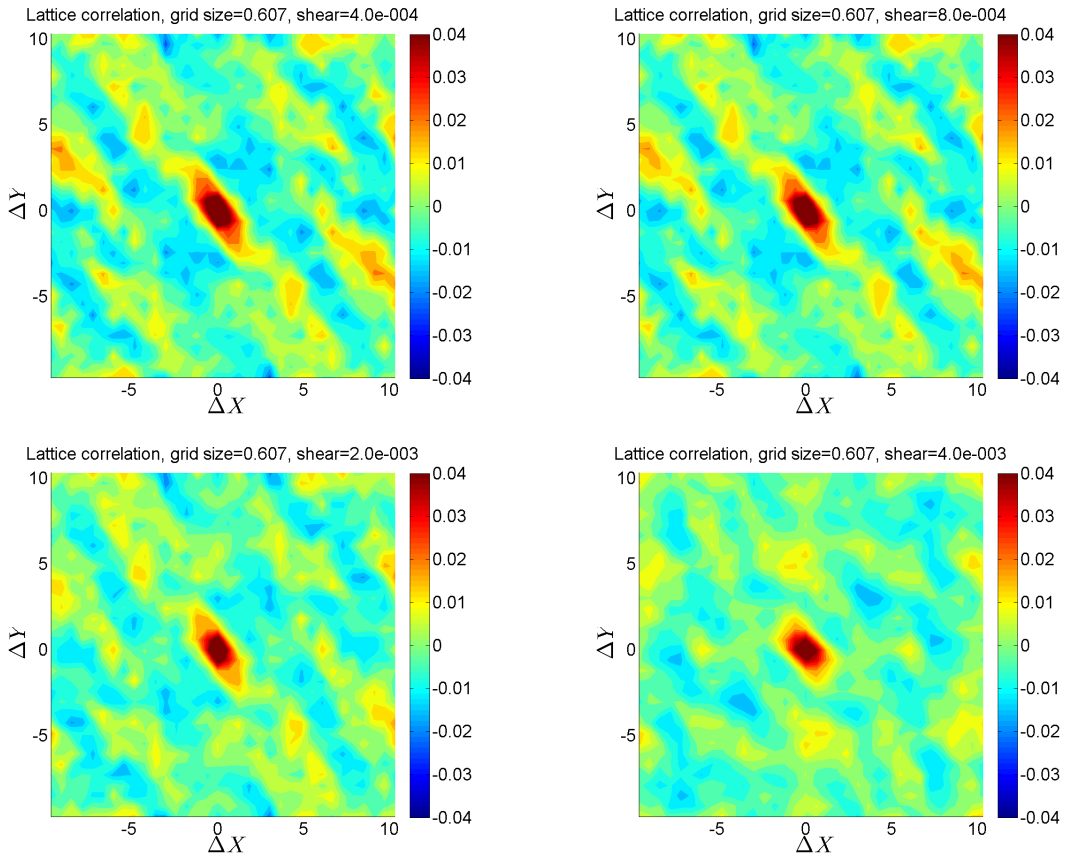

Figure 5.8: Spatial correlation of $\boldsymbol{B}$ at different shear for isotropic network.

to the growth of ΔG_γ by using the critical compressive load $F_c = \pi^2\kappa/\ell^2$ [41] for Euler buckling of a filament of length ℓ. Assuming affine deformation and compressive strain along $\phi = -\pi/4$, we find a critical strain $\gamma_c = 2\pi^2(\ell_b/\ell)^2$ for buckling. Clearly, the longest simply-supported segments will be the first to become unstable to compressive loads. These will be followed, at higher strains, by segments of more typical length $\sim \ell_c(-\pi/4)$ (the typical distance between crosslinks on filaments under compression). The collective mechanical response of the gel is likely to already be nonlinear at the strain values where these more common filament segments buckle, so our assumption of affine deformation in making this estimate is suspect. Consequently, we suggest that γ_c must be treated as an upper bound on the critical strain for buckling. For a network with $L/\lambda = 7.9$ one finds that $\gamma_c \simeq 10^{-2}$; from Fig. 5, we see that this is an acceptable upper bound, as the gel leaves the linear

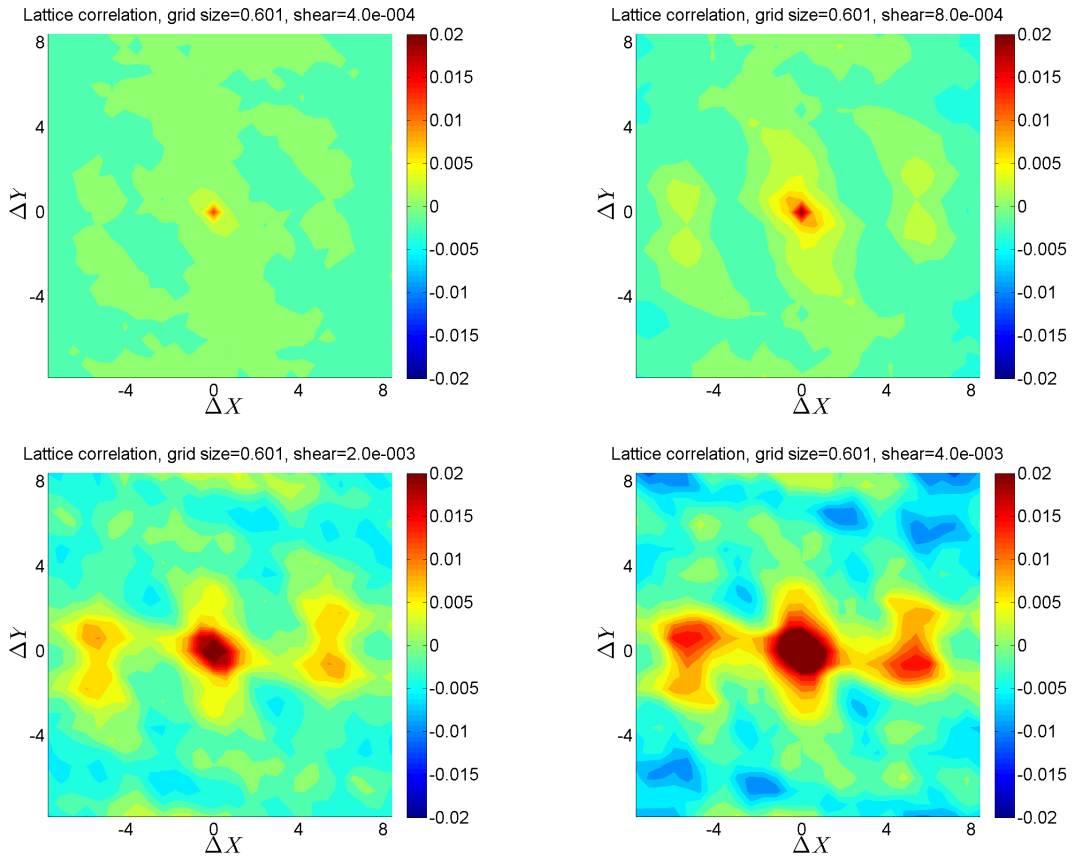

Figure 5.9: Spatial correlation of $\boldsymbol{B}$ at different shear for anisotropic network.

response regime at strains about an order of magnitude smaller. Buckling of the longer simply-supported segments appears to induce buckling in adjoining segments and generate nonaffine deformations, which suppresses the critical shear strain for nonlinear response below our estimate.

5.4 Conclusion

It is found that anisotropic networks, like isotropic networks, undergo an affine to nonaffine cross-over that is controlled by L/λ. The geometric measure of non-affinity depends on L/λ in a manner independent of anisotropy. The mechanics of affine networks of arbitrary anisotropy can be understood in terms of the usual generalization of isotropic continuum elasticity theory to orthotropic solids; nonaffine anisotropic networks, however, are more

complex. Though the linear elastic response of these nonaffine anisotropic networks can be accounted for by a generalization of the floppy modes analysis, the regime of linear response is vanishingly small; well-oriented and sparse regions of the cytoskeleton will thus invariably have a highly nonlinear elastic response dominated by buckling of filaments. Such gels are highly sensitive to the orientation of applied loading relative to their symmetry axes—more so than can be accounted for by the symmetries of the linear elastic modulus tensor. The model predicts that these gels exhibit stiffening when strained with the nematic direction in tension and softening in compression; these effects, present at the very small strains we have studied, will be even more pronounced at larger (biologically relevant) strains, and should be clearly observable in experiments.

CHAPTER 6

Dynamic Network with Labile Crosslinks

6.1 Introduction

In all the previous chapters, the network is analyzed in a zero-frequency manner with the assumption that the crosslinks, which may be thought of as modeling some type of actin binding proteins, are permanent. In real cells, however, they can break and rebind with varying rates [87], which is both a reason that the actin filament network is a dynamic system, and the phenomenon that governs cytoskeleton's rheology [88]. While most of the existing modeling work on semiflexible networks has been focused on networks with rigid, permanent crosslinks, recent efforts have been started to understand the role of crosslink deformability [89] and dissociation [90, 91] on the overall transient network response under dynamic loading. Although models of a network with permanent crosslinks can predict its linear and nonlinear elastic response, they fall short of predicting a semiflexible network's viscoelastic behavior seen both in vitro [88] and in vivo [92, 93]. Thus, there is a great need to determine the contribution of crosslinks that are *labile* to the overall viscoelastic response of semiflexible network.

In contrast to the permanent, infinitely stiff crosslinks used in the simulations shown in previous chapters, crosslinks in cytoskeleton have finite stiffness and are breakable. Since crosslinks connect filaments and therefore are also load-bearing components, their dissociation should be dependent on their local force. Here the increased dissociation rate of chemical adhesion bond due to external load is described by a simple statistical mechanical model first introduced by Bell [94]. Bell proposed that the dissociation rate of bond, ω, is the product of the bond's natural vibration frequency ω_0 and the quasi-equilibrium probability of reaching

the dissociation state with an energy barrier E_b, subtracting work done by external load $f \times \delta$, with f being the force acting on the bond and δ being displacement, to give

$$\omega = \omega_0 \exp \frac{E_b - f\delta}{k_B T} \tag{6.1}$$

Thus, the dissociation rate is exponentially dependent on the bond's external load. Bell's model was the first model dealing with chemical bond dissociation to consider the importantce of mechanical forces, and all parameters of the energy barrier has been simplified into one parameter, the displacement δ. There have been other chemical bond dissociation models based on Bell's model. For instance, Evans *et al.* [95] introduced a dissociation rate model following power law to capture the variation from ductile to brittle bond failure. Although more sophisticated models are available, I use Bell's original model in the following simulations and will show that this model is sufficient to describe semiflexible network's transient response to dynamic loading.

Since broken crosslinks in cytoskeleton are free to rebind, the rebinding process will be considered and modeled in this simulation, too. There is limited information in the literature on the rate of crosslink rebinding of actin filament or microtubule. Based on the assumption that there is always plenty of actin binding protein available in the proximity of network, I use a constant rebinding rate for the network.

6.2 Model and Simulation Procedures

6.2.1 Network Discretization

Similar to the networks presented in previous chapters, some number of filaments are placed onto a 2-D square box with random positions and orientations. The filaments are discretized into segments of the same length and modeled as beam elements with stretching modulus μ and bending modulus κ. Intersections of each pair of two segments (of two intersecting filaments) are calculated and crosslinks are attached onto each of the two segments at their intersection point. Crosslinks are modeled as linear springs with stiffness k, which is taken to be much larger than the characteristic stiffness of the filaments. An example of such a

network is shown in Fig. 6.1.

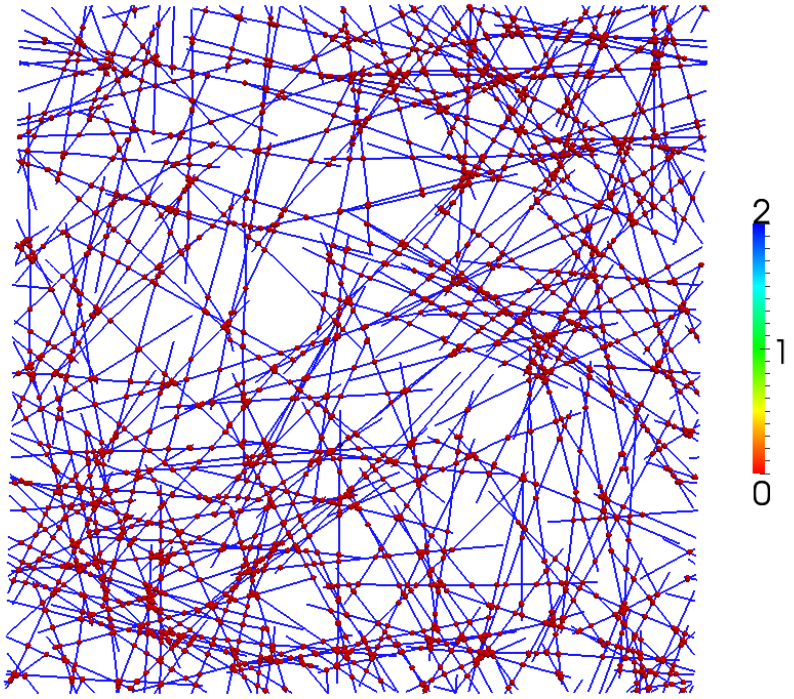

Figure 6.1: An example of network with labile crosslinks under shearing. Intersections with intact or active crosslinks are shown with colored spheres: red spheres are intact crosslinks, green ones are crosslinks that are about to break, and blue ones are crosslinks that have just been rebound. Network is loaded by shearing the top and bottom boundaries.

Crosslinks get broken and rebound randomly at each intersection site while simulation goes. Because crosslinks are now labile and it is generally not the case that *all* the intersection sites get linked. Overall, the total number of attached crosslinks in the network is stable with small oscillation around a number which is determined by the mechanics of the network. The protocol of determining how crosslinks get broken and rebound will be explained in details later in this chapter. Also, when the simulation proceeds, the intersection point of two segments generally will change due to the changing geometry of the network. To avoid expensive remeshing steps, the filaments are all discretized uniformly with the same segment length. Crosslinks are then attached to intersection point of two segments by interpolating the connection node between segment nodes. Fig. 6.2 shows a schematic of the

crosslink interpolation connection idea. Two segment (black lines) with four filament nodes (gray dots) are shown with a crosslink (red dots) attached at one third of each segment. The interpolation parameter ξ denotes the relative position of the crosslink's end on each segment (ξ_1 and ξ_2). For example, $\xi = 0.5$ means the crosslink end is right at the center of the segment. For the example shown in Fig. 6.2, $\xi_1 = \xi_2 = \frac{1}{3}$ which means the distance between the crosslink end to the first node of segment is one third of the segment length. Although a crosslink has two ends which are attached to filament segments, they are not active degree of freedom in the simulation. The positions of the ends of crosslinks are interpolated from the segment nodes which are connected by the crosslinks. Assume the positions of the four nodes of two segments are $\vec{x_{11}}$, $\vec{x_{12}}$, $\vec{x_{21}}$, and $\vec{x_{22}}$ respectively, then the positions of the ends of a crosslink, that connects these two segment, $\vec{c_1}$ and $\vec{c_2}$ can be interpolated from

$$\vec{c_1} = \xi_1 \vec{x_{11}} + (1 - \xi_1)\vec{x_{12}} \tag{6.2}$$

$$\vec{c_2} = \xi_2 \vec{x_{21}} + (1 - \xi_2)\vec{x_{22}}. \tag{6.3}$$

Since crosslinks are modeled as linear springs, their internal force can be calculated from $F = k\Delta x$, where Δ is the distance between crosslink ends. The crosslink force then has to be transferred to the active DOF's of the segments. I use the following formulae to make sure that the crosslink doesn't generate any moment on the segments

$$F_{11} = (1 - \xi_1)F \tag{6.4}$$

$$F_{12} = \xi_1 F \tag{6.5}$$

$$F_{21} = (1 - \xi_2)F \tag{6.6}$$

$$F_{22} = \xi_2 F. \tag{6.7}$$

The directions of these nodal forces are always along the crosslink's direction, as shown in Fig. 6.2. The interpolation parameter ξ is calculated when a crosslink is generated or rebound at a new site. Using this technique, breaking/rebinding crosslinks are made possible without the need of remeshing the whole network, which is very expensive.

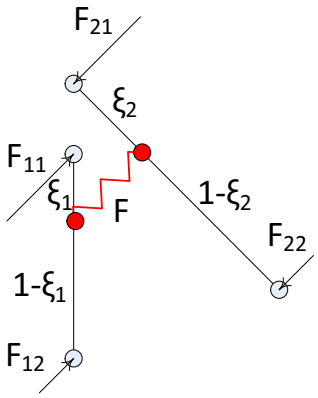

Figure 6.2: Schematic of a crosslink (red spring) connecting two filament segments (black lines). The actual nodes of filaments are represented by gray circles, and the interpolation points of the crosslinks are shown in red circles. The interpolation parameter $\xi(0 < \xi < 1)$ is a measure of the crosslink attaching point relative to the segment. The internal force of the crosslink modeled as a spring is calculated from $F = k\Delta x$, and each one of the four filament nodes connected by the crosslink gets a nodal force (F_{11} through F_{22}) from the crosslink's internal spring force.

6.2.2 Force-controlled Loading

Besides the breakable crosslinks, another major difference between the model in this chapter and previous is the external loading. Here we wish to examine the viscoelastic response of network under both fixed displacement(i.e. stress relaxation) and fixed applied force(i.e. creep). In addition to the displacement (strain) control used exclusively in previous chapters, a variational method for force (stress) control is developed for the Lees-Edwards periodic boundary condition and used in simulations. To load the network by a fixed external force, the work done by it is subtracted from the total energy of the network

$$E = E_{\text{fil}} + E_{\text{cross}} - Fd. \tag{6.8}$$

Here F is the external load applied on the top and bottom boundaries (opposite directions), d is the displacement of the network's boundary in the shear direction, and the expressions for E_{fil} and E_{cross} can be found in Chapter 2.

Now that the shear of the boundary, given by d, is an unknown degree of freedom, it is clear that application of the force control loading to Lees-Edwards periodic boundaries is a tricky problem. The reason is that we need to compute the internal force conjugate to d, which is $F = \frac{\partial}{\partial d}(E_{fil} + E_{cross})$. One crude option is to remove the periodicity on the top/bottom boundary and use fixed/force boundary condition for each of them. Although this may be a quick fix, this method generates an unfavorable layer near the top/bottom boundary where sigficantly less crosslinks can be attached, and this issue can be problematic especially for smaller networks. To develop a more robust implementation of force control for periodic Lees-Edwards boundary, we found it helpful to define the concept of a pseudo node, onto which the force is applied, and effectively distributed to the network nodes in a consistent way as follows. The only DOF of the pseudo node is the displacement d in the shearing direction, and the displacement d provides a one-on-one mapping between displacement and shear strain, by $\gamma = d/h$, where h is the height of network. With γ given from d, the network can be mapped using Lees-Edwards periodic boundary condition in the same way as in displacement controlled networks. However, in order to equilibrate the pseudo node and thus the system, there has to be some internal forces to counter the external force acting on the pseudo node, and those forces, come from the crosslinks. Let's first think about the displacement-controlled networks: the shearing is essentially performed by mapping tied filament nodes using periodic boundary conditions; when two nodes are mapped and tied, there is a distance generated between them from the shear strain, and the crosslink will try to pull one of the node to the other, thus generate shear deformation throughout the network. So it is the same idea for a force controlled Lees-Edward boundary, where mapped crosslinks are the ones distribute shear loading throughout the network and generate shear deformation. This can be derived by minimizing the total energy of the network, take the derivative of Eq. 6.8 with respect to d,

$$\frac{\partial E}{\partial d} = \frac{\partial E_{\text{fil}}}{\partial d} + \frac{\partial E_{\text{cross}}}{\partial d} - F = 0 \tag{6.9}$$

Noting that E_{fil} is not a function of d since shear strain of network essentially affect the

mapped distance between two nodes of crosslink, thus

$$F = \frac{\partial E_{\text{cross}}}{\partial d} \tag{6.10}$$

Let's define f_i being the internal force of crosslinks whose two nodes get mapped around the periodic boundary condition, such that $f_i = kd$ if the stiffness of crosslink is stiff enough such that the crosslink's initial deformation can be neglected. Thus

$$F = \frac{\partial E_{\text{cross}}}{\partial d} = \sum_i f_i \tag{6.11}$$

Thus, the shear loading F acting on the pseudo node should be balanced by the internal spring forces (component in shearing direction) from all crosslinks that get mapped. Thus the nodal force on the pseudo node is

$$f_{\text{pseudo}} = F + \sum_i f_{i,x} \tag{6.12}$$

where it is assumed that F is acting in the x direction, and $f_{i,x}$ represents the ith crosslink's x component. This method allows the author to use force control on a Lees-Edward periodic network without having to deal with the boundary layer issue arised from a fixed bottom/top boundary network.

6.2.3 Time-Stepping and Crosslink Kinetics

Using the force controlled boundary condition, the network's equilibrium will be solved at each time step. During each time step, crosslinks are allowed to break or rebind after which the residual forces in the network are relaxed by minimizing the energy and allowing the network to deform. For the crosslink breaking process, the Bell's model in Eq. 6.1 is used. The Bell's model provides crosslink's off *rate*, which involves time. I didn't use physical time in my simulation for the following reasons: First, we don't really know the value of energy barrier E_b in Eq. 6.1 for actin crosslinks, and it will have different values for different type of crosslinks anyway; Second, using a fixed physical time in the simulation gives me no control over how many crosslinks break during each step. I instead treats this problem in pseudo time or *simulation time* which is a physical time unit that is equal to an unknown

but constant time interval. Furthermore, the term $\exp E_b/k_BT$ in Eq. 6.1 is lumped into ω_0 and a new constant is defined as $p_{\text{off}} = \omega_0 \exp E_b/k_BT$. If we consider the off *rate* in Bell's model as a measure of off *probability*, we may define the probability of the ith crosslink to break during each time step to be

$$p_{i,\text{off}}(f_i) = p_{\text{off}} \exp(f_i\delta/k_BT) \tag{6.13}$$

where f_i is the spring force of the ith crosslink. As stated before, it is assume that the rebinding (on) rate of a crosslink is constant independent of crosslinks or their spring forces, thus the rebinding probability at each open intersection is

$$p_{i,\text{on}} = p_{\text{on}} \tag{6.14}$$

Since the *simulation time* is a quantity free to be determined, we determine its value by considering the following two aspects: First, simulation time covered by each step, Δt, can not be too small, because of the limited total computation time. Remember that during each time step, the network's equilibirum needs to be solved. Second, simulation time covered by each step can not be too large, either. If Δt is so large that way more than 1 crosslinks are broken each step, the effect of all the broken crosslinks on the network will only be solved once at the end of the step, which is not physical in reality. As a result, the program will use adaptive time step Δt by tuning the prefactor p_{off} and p_{on} before each time step marching to make sure there is around 1 breakage during each step. Using this adaptive time steps, during Δt marching, both intact and broken (if any) crosslinks will be looped: intact crosslinks are randomly selected to break following Bell's model with probability in Eq. 6.13; broken crosslinks are randomy selected to rebind following a constant probability p_{on}. The following algorithm and Fig. 6.3 demonstrate the process.

1. Before each step starts, all the *intact* crosslinks are looped through and the probability for each of the crosslinks to break, $p_{i,\text{off}}$ is calculated (Fig. 6.3(a))

2. The breaking and rebinding constants p_0 and p_f are rescaled while keeping their ratio $p_0/p_f = 1/4$ such that

$$0.5 < \sum_i p_{i,\text{off}} < 1.5$$

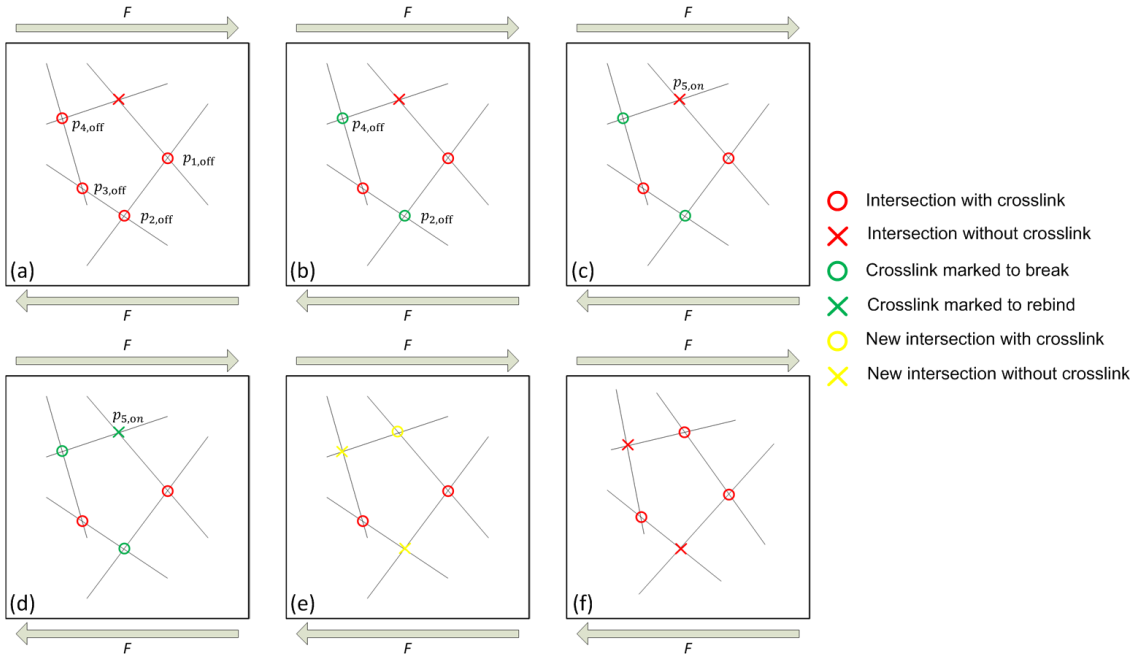

Figure 6.3: Schematic representation of labile crosslinks breaking and rebinding algorithm in a simulation step: (a) All the intact crosslinks (crosslinks 1 through 4 in figure) are looped through and the probability for each crosslink breaking, $p_{i,\text{off}}$ is calculated; (b) Crosslinks are randomly selected to break (crosslinks 2 and 4 in figure); (c) Available crosslink sites (broken crosslinks) will be rebound randomly according to $p_{i,\text{on}}$ with zero initial spring force; (d) Crosslink 5 is marked to rebind; (e) Crosslinks are marked to break and rebind, network in this state is not in equilibrium; (f) Network is solved and is equilibrium, go to next step.

3. Each *intact* crosslink goes through the random breaking process according to a random number p generated every time by the program, if $p < p_{i,\text{off}}$, the crosslink is removed (Fig. 6.3(b))

4. Each *broken* crosslink (or more precisely, open filament intersections without crosslink) will rebind randomly according to a random number p generated every time by the programconstant probability (Fig. 6.3(c)). If $p < p_{\text{on}}$, a new crosslink will rebind at the intersection with zero initial spring force (Fig. 6.3(d))

5. The network is solved by minimizing the total energy of the network. Note that the

broken crosslinks will not have any contribution on the total network energy nor affect the mechanics of the filament (Fig. 6.3(e) and (f))

6. Statistical quantities of the network is calculated; Output files are generated

7. Next step starts, go to step 1.

Due to the long computational time required by dynamic simulations, the number of filaments and system size are reduced to about a quarter of that used in previous chapters. For the simulations shown later in this chapter, pN and μm will be used as the force and length units. Here are some constants and numbers used in the simulation: around 250 filaments are placed onto a 25 by 25 μm box, which generates nearly 3000 initial crosslinks; the filaments are modeled using microtubule's stretching and bending stiffness with L_P being 2000 μm and ℓ_B being 0.025; the spring stiffness of crosslinks is chosen to be $1.0e5pN/\mu m$; the average length of filament is chosen to be 10 μm and δ is 0.01 μm; room temperature is used so that $k_BT = 4.1e-3\mu m \cdot pN$; the load applied ($F$) on network ranges from 5 to 200 pN.

6.3 Results

This section discusses the results from the simulation of semiflexible network with labile crosslinks. First of all, several benchmark simulations are performed and presented to show that the breaking/rebinding mechanism is working properly; secondly, simulation data is compared with experimental data to validate the simulation procedure and study semiflexible network's rheology; lastly, some additional results are shown together with some discussions.

6.3.1 Labile Crosslink Benchmark Tests

Before implementing the program to do real simulations, couple of sanity checks on the crosslinks breaking/rebinding mechanism is performed to make sure the mechanism is working properly and also to assess its behavior. Firstly, the random breaking/rebinding process is tested on networks without loading to see whether the number of intact crosslinks can

stabilize around the right number; secondly, the random process is tested on networks with loading to check whether the effect from loading can shift the stabilized number of intact crosslinks to the correct direction.

The first check is done without applying load. Using networks consist of labile crosslinks, random breakings and rebindings are performed during each step according to Eq. 6.13 and 6.14, and around forty thousand steps are run until the simulation time reaches 4. Networks with 30 percent crosslinks bonded initially are released/rebound with 3 different sets of crosslink breaking probability p_{off} and rebinding probability p_{on}, as shown in Fig. 6.4. The ratio of bonded crosslinks N_{b} and total number of available crosslink sites, N_{total}, is plotted evolving over time. Since there's no load on the network, the internal force of each crosslink should be zero at any time. Thus, every crosslink's breaking probability should be $p_{\text{i,off}} = p_{\text{off}}$ with rebinding probability being p_{on}, from which we can easily expect that the ratio $N_{\text{b}}/N_{\text{total}}$ should be around $p_{\text{on}}/(p_{\text{off}}+p_{\text{on}}) = p_{\text{on}}$ when the network's breaking/rebinding process gains equilibrium. It can be seen from Fig. 6.4 that all the three cases start at 30% and eventually approach to their corresponding probability ratio p_{on}. This proves that the random breaking/rebinding mechanism in the code produces correct statistics when load is turned off.

The second check is on the simulations of network with various shearing loads. Fig. 6.5 compares three networks under shear loading evolving over time. All the three networks initially have around 80% bonded crosslinks [1]. The network's shear strain response (upper subfigure) is plotted alongside with their bonded crosslink ratio $N_{\text{b}}/N_{\text{total}}$ (lower subfigure) over time. In the strain-time plot, there are two things supporting that the program is running right: first, the instant elastic responses from $F = 5$, 10, and 20pN have ratio around 1:2:4, which means the network's force boundary control generates linear elastic responses when the network is applied constant force; second, network with higher load has faster creep speed, which also makes sense, and will be discussed in more details in the following section. The $N_{\text{b}}/N_{\text{total}}$ over time plot shows that for all the three networks initially

[1] Note that the initial bonded crosslinks are selected randomly at each crosslink site such that each network will not have excatly the same bonded crosslink percentage at the beginning of simulation

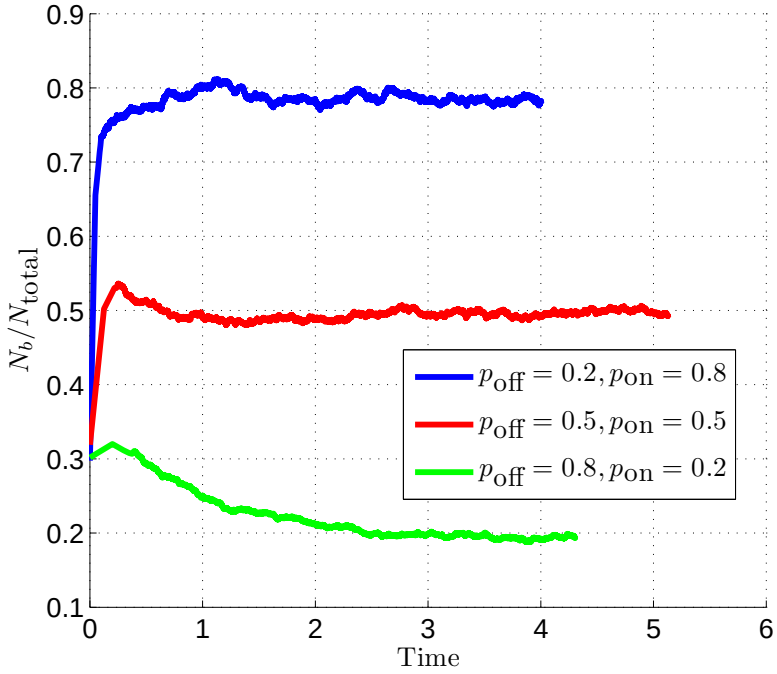

Figure 6.4: Three networks with different breaking/rebinding probabilities are evolved over tiem without load to test whether teh code generates correct statistics, all three networks have an initial bonded crosslink ratio of 30%. Ratio of bonded crosslinks over total available crosslink sites is plotted versus time, and all three networks approaches their corresponding probability p_{on} respectively

having 80% bonded crosslinks, while sheared under loads, the bonded crosslink percentage tends to go below the 80% mark. Note that the breaking/rebinding probability for these networks are $p_{\text{off}} = 0.2$ and $p_{\text{on}} = 0.8$, thus for a network without load, the $N_{\text{b}}/N_{\text{total}}$ ratio will be around $0.8/(0.8+0.2) = 80\%$. When load is applied, most of the crosslinks will have forces due to the external loading, which according to Eq. 6.13, increases crosslinks breaking probability. Thus, it makes sense to see that all the three networks eventually have their $N_{\text{b}}/N_{\text{total}}$ ratios below 80% mark and the higher the load applied, the lower is the $N_{\text{b}}/N_{\text{total}}$ ratio while in equilibrium.

Both of the tests shown above demonstrate that the crosslink breaking/rebinding process is working properly in the program. More simulation data will be shown in detail in the

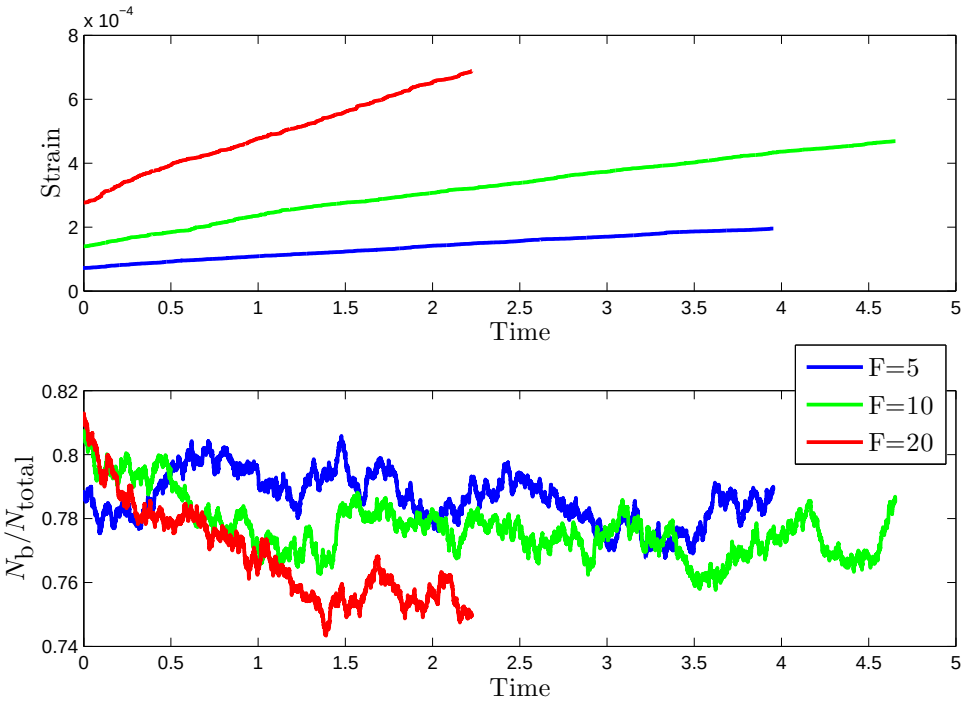

Figure 6.5: Three networks under shear loading $F = 5, 10, 20pN$, evolving over time are plotted. All the three networks initially have around 80% bonded crosslinks. Upper: the network's shear strain response over time. Lower: Bonded crosslink ratio N_b/N_{total} over time.

following sections using the program.

6.3.2 Comparison with Experiment

To validate the crosslink breaking/rebinding mechanism, numerical simulations of network rheology, modelling the microtubule networks has been carried out. Since it is assumed that the mechanical relaxation of the network is arbitrarily fast in comparison, the *simulation time* is the only timescale in the problem. Consequently, all the simulation dynamics will be reported in terms of simulation time. The data is then compared with the experiment reported by Yang *et al.* [4]. In their experiment, time- and force-dependent viscoelastic responses of reconstituted networks of microtubules, which have been strongly crosslinked

by biotin-streptavidin bonds, are investigated and reported. To measure the microscale viscoelasticity of such networks, a magnetic tweezer device is used to apply localized forces on a bead which in turn pulls the microtubule network.

A direct comparison is shown in Fig. 6.6 for the dependence of the creep strain rate on applied shear stress between simulation (red circles, right ordinate axis) to the experimentally observed creep velocity of the bead (black symbols, left ordinate axis) as a function of loading (common abscissa). Since the simulations involve an arbitrarily chosen fundamental time scale, and it is a complex problem in this nonlinear viscoelastic material to relate the local shear strain rate in the network to the bead's velocity, there is an unknown conversion factor between the simulation and experimental data. Similarly there is a scaling factor between the shear stress and bead's loading. A single rescaling of the x-axis by 0.8 has been made to make the simulation results match at the lowest loading, and the strain rate data has been plotted using the right y-axis. The overall agreement between the simulation and experiment over all loading regimes strongly supports our contention that a simple Bell model of crosslinker unbinding is sufficient to account for all of the observed creep dynamics. In both cases, the creep rate appears to be exponential for moderate loads, and then increases more slowly at higher loads. As discussed above, to eliminate both fitting parameters in the comparison of simulation and experiment one must either understand the solution of the hydrodynamic flow in this highly nonlinear and viscoelastic material, or directly simulate the motion of a bead in a model network, requiring much larger systems that are not currently feasible.

The creep velocity responses of the simulation are plotted in Fig. 6.7, for a characteristic set of model parameters. The simulations show the same main qualitative features as the experiments [4]: An instantaneous elastic jump, followed by a creep regime in which strain increases roughly linearly in time. When the force is removed, there is another elastic jump back of roughly the same magnitude as the initial elastic jump forward. This final elastic jump is followed by an exponential relaxation of some fraction of the remaining strain. The key utility of the simulations is that one has access to all crosslinker breakage and formation events under load. In Fig. 6.7 we test our contention that the nonrecoverable strain, i.e., plastic deformation of the material can be understood in terms of bond breakage.

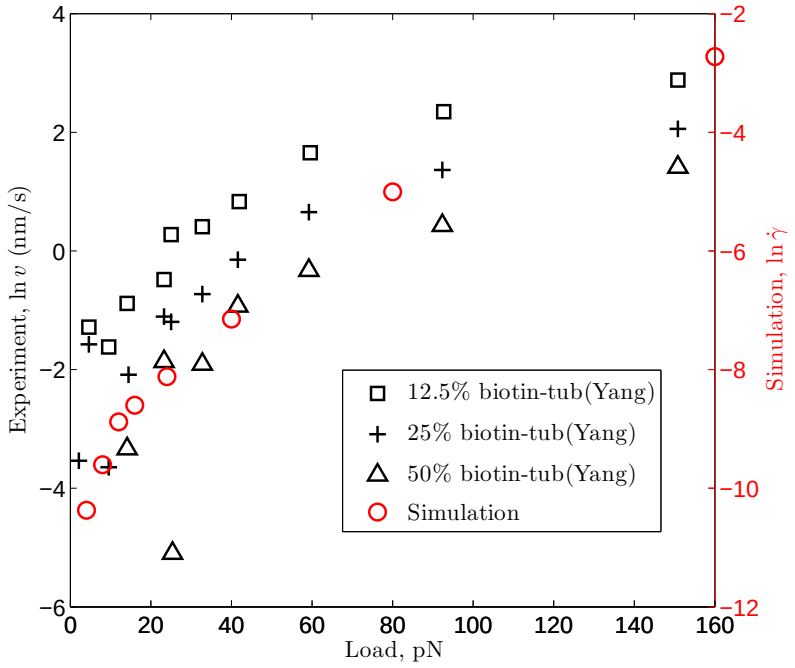

Figure 6.6: The creep velocity v is plotted as a function of force on the log-linear plot. From experimental data (black symbols), the creep velocity v increases with force and decreases with filament density. The experimental data are compared to that inferred from the simulation of the strain rate as a function of applied shear stress (red circles). To enable comparison, the author rescaled the x-axis by 0.8 so that the data and simulation agreed at the lowest loading. The agreement over all loadings shows that the Bell's model crosslinker unbinding in a filament network is sufficient to explain the experimentally observed dynamics.

The network is strained for three different lengths of time chosen so that nearly all (98%) of the original crosslinks were preserved (red), about half (54%) were preserved (green), or only a small fraction (18%) of them were preserved (blue). It is clear that the size of the unrecoverable strain in the network increases with the decreasing fraction of original crosslinkers preserved. This supports our interpretation of the experimental data for which we cannot observe individual bond breaking events. Moreover the equivalence of the elastic jumps at the time of loading and unloading the system shows that the elasticity of the network is essentially unchanged by the bond breakage and reformation events. Only the

original reference state of the elastic material has evolved in time. From these numerical results we propose that the bond breakage mechanism is sufficient to account for the observed data in the experimental system.

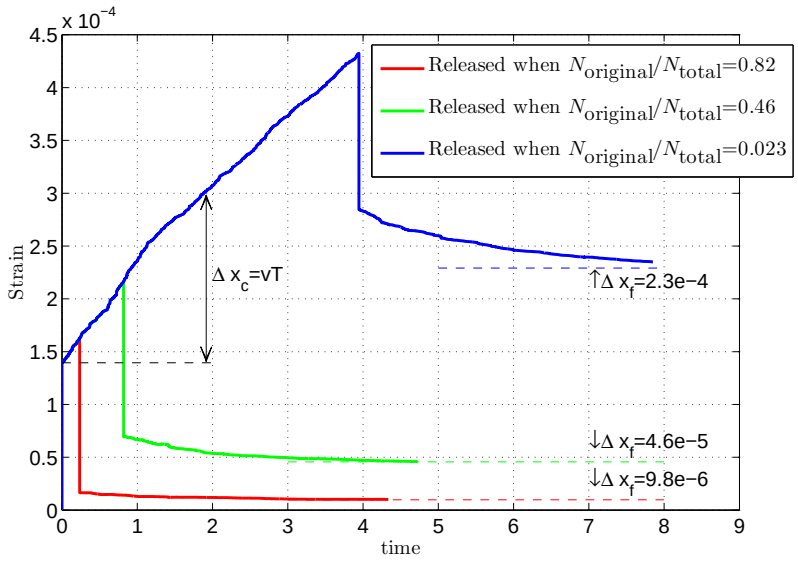

Figure 6.7: Numerical simulation of strained filament networks for three different loading times chosen to leave different fraction of the original crosslinkers (N_{original}) intact. Total crosslinkers is N_{total}. Simulation time is defined in terms of the Bell model crosslinker unbinding rate for unloaded bonds – see text for more details. Each shear strain trace shows the principal dynamics observed experimentally: loading produces an instantaneous elastic strain followed by a creep regime (Δx_c) in which the strain increases linearly in time; unloading triggers a partial elastic recovery followed by an additional exponential relaxation. The loading times were chosen so as to preserve differing fractions of the original crosslinkers. For the shortest loading time (red), 98% of the original crosslinkers were preserved and the residual plastic deformation was unobservable. As the fraction of original crosslinkers decreased (longer force application times) the residual plastic deformation (Δx_f) increased.

The residual strain Δx_f can be further examined by normalizing with the creep strain $\Delta x_c = vT$, which is defined as the product of creep velocity v and simulation time T. The ratio of Δx_f and Δx_c is then a dimensionless measure of plastic residue over creep

deformation. Fig. 6.8 shows $\Delta x_f/\Delta x_c$ as function of time and force. The left panel in Fig. 6.8 shows creep tests with load $F = 10$pN which are relaxed at t=0.23, 0.82, and 3.95 respectively; the longer the network is allowed to creep, the greater is $\Delta x_f/\Delta x_c$. This is another proof that the final plastic residue generated by creep is dependent on how many original crosslinks are there in the network, because the longer the loading, the more original crosslinks will get broken. The right panel in Fig. 6.8 shows that for tests with loads $F =$ 5,10,20, and 30pN, all relaxed at t = 0.7. It shows that when networks are relaxed at the same time, their $\Delta x_f/\Delta x_c$ ratio decreases with increasing load. In another point of agreement with the simulations and the experiments is that, the simulations yield incomplete recovery of networks after shear stress loading. Fig. 6.8 also shows that the permanent plastic deformation Δx_f retained after unloading and relaxation is in the range of 50-75% of the creep deformation, meaning that about 25-50% of the viscous creep deformation is recoverable.

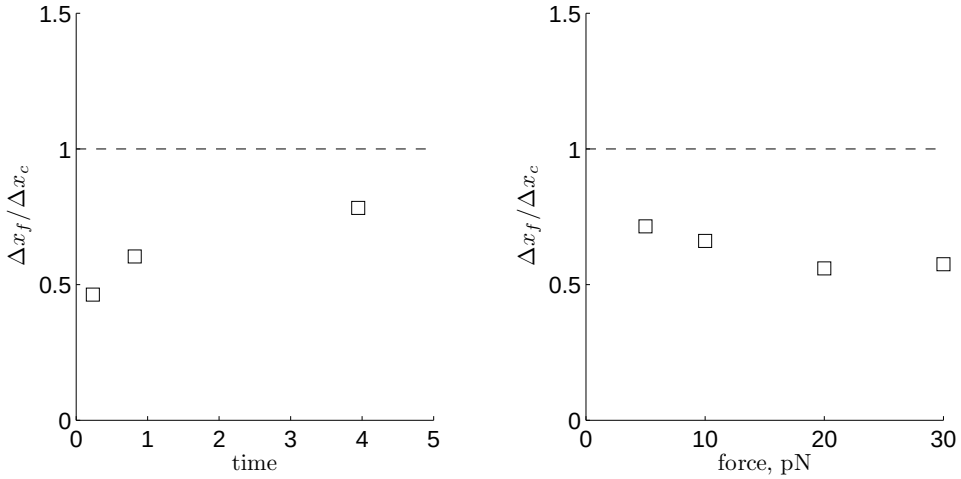

Figure 6.8: Using the total creep distance Δx_c and residual plastic deformation Δx_f, the author computes from the simulation data the analogues of experimental data [4]. Left: $\Delta x_f/\Delta x_c$ vs. force, all four networks relexed at $t = 0.7$. The ratio of $\Delta x_f/\Delta x_c$ decreases with force, which is in good agreement with the experiment. Right: $\Delta x_f/\Delta x_c$ vs. time, all three networks having load $F = 10$pN. $\Delta x_c/\Delta x_f$ increases with time, which supports the claim that plastic residue is dependent on how many original crosslinks are there in the network

6.4 Discussion

It has been shown in the previous sections that the network model with labile crosslinks is working properly and produces reasonable results matching experimental data. This section shows some more simulation results which are not available from experiment measurement but will shed light onto the dynamics of semiflexible network with breaking/rebinding crosslinks.

The dynamic response of semiflexible network with labile crosslinks under external force loading is shown in Fig. 6.7, where the network's creep shear strain over time is plotted. So how is the strain energy stored in the network? This question could not be answered by experiment since strain energy measurement is not achievable in semiflexible network experiment, simulations can easily track network's strain energy storage. Fig. 6.9 plots strain energy distribution (bending, stretching, and crosslinks) and work done by external load over time, and three cases with different loading time are plotted individually to better show their trends. First of all, it can be seen that most of the strain energy of the network is stored in stretching energy form, which is as expected from our understanding of istropic network in Chap.3 and 4 that dense network like this ($L/\ell_c \approx 20$) has most energy stored in stretching. Secondly, after an initial jump of energy due to the network's elastic response to loading, all energy increases over time but eventually approaches a plateau. This means the energy dissipation rate, which is the difference between work done by external load and strain energy stored per unit time, will increase when the network is just loaded, and will eventually approach to a constant rate. The constant rate is just the power of the external loading since eventually the network can not take in any more energy and all the power done by external load will be dissipated. Thirdly, when network is released from loading after some time, the stretching and bending energy will instantly recover approximately the same amount of energy as the initial loading energy, which means the portion of network/filament deformation accounting for the initial loading energy is never dissipated until the load is removed. Also, notice that in Fig. 6.7, the network's shear strain has a significant residue Δx_f if loaded over a long time (blue and green curves); however in Fig. 6.9, none of the three cases has any residual energy, i.e. all the strain energy will be dissipated at the end. The

difference in strain and strain energy residues proves that, during the creep stage, there is some type of structual reorganization of the filaments in the network, e.g. reletive filament sliding/moving, which permanently changes the undeformed state of the network such that when all the strain energy is dissipated through crosslink breaking/rebinding, network will have permanent, plastic residual strain.

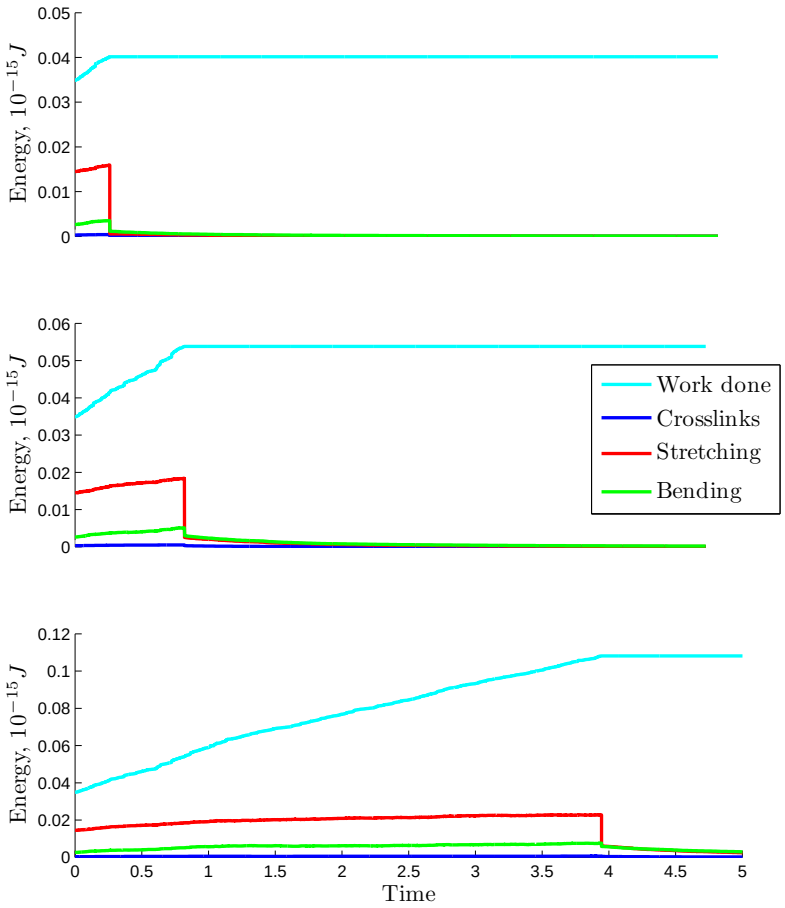

Figure 6.9: Strain energy and work done by external load over time for networks under shear loading and unloaded at three different time. The network is the same and under the same loading as in Fig.6.7

Talking about network's structural reorganization, there is an interesting question to ask: whether crosslinks have any preference while choosing which one to break? To answer this

question, let's first see whether crosslink breakages tend to happen at the same filament. Define the event of the i'th filament having some crosslink on it to break at time t, as $B_{i,t}$, then

$$B_{i,t} = \begin{cases} 1, & \text{filament } i \text{ has some crosslink on it breaking at time } t \\ 0, & \text{filament } i \text{ doesn't have any breakage at time } t \end{cases} \tag{6.15}$$

Then the event $B_{i,t}$'s autocorrelation is

$$\langle B_{i,t+\Delta t} \cdot B_{i,t} \rangle = \left(\sum_t B_{i,t+\Delta t} \cdot B_{i,t} \right) / \sum_t \tag{6.16}$$

where Δt is the simulation time during each time step since the simulation has discrete time steps. For the whole network, the autocorrelation of crosslink breakage on the same filament, $\langle B_{\Delta t} \rangle$, can be calculated from

$$\langle B_{\Delta t} \rangle = \left(\sum_i \sum_t B_{i,t+\Delta t} \cdot B_{i,t} \right) / \sum_{i,t} . \tag{6.17}$$

Fig.6.10 shows autocorrelation of same filament crosslink breakage over $\Delta t = 0 \sim 0.2$ simulation time, and obviously there's no correlation up to 0.2 simulation time interval. That's means when the i'th filament has a crosslink breakage at time t, for the next 0.2 time, the same filament doesn't have a higher chance to have another crosslink breakage. So, now the answer to whether crosslinks tend to break at the same filament, is no. Let's then see whether there is any spatial correlation on crosslink breakage.

To calculate the spatial correlation of crosslink breakage in the network, the spatial snapshots of all crosslink breakage locations over several time steps are saved and analyzed. Fig.6.11's right panel shows a snapshot of broken crosslink's positions in 300 steps collapsed together. The position snapshot is used to count each pair of broken crosslinks and sorted according to their distance. The number of pairs in each bin of distance is then normalized by its annulus area to get avearage number of pairs per unit area (equivalent to probability density function as function of radius $P(r)$), as shown in the left panel of Fig.6.11. The plot clearly shows there is a strong spatial correlation of crosslink breakage, in other words, crosslink breakages tend to happen near each other. From the plot, the correlation is up to 1 μm, which is about 3 times average distance between crosslinks ℓ_c.

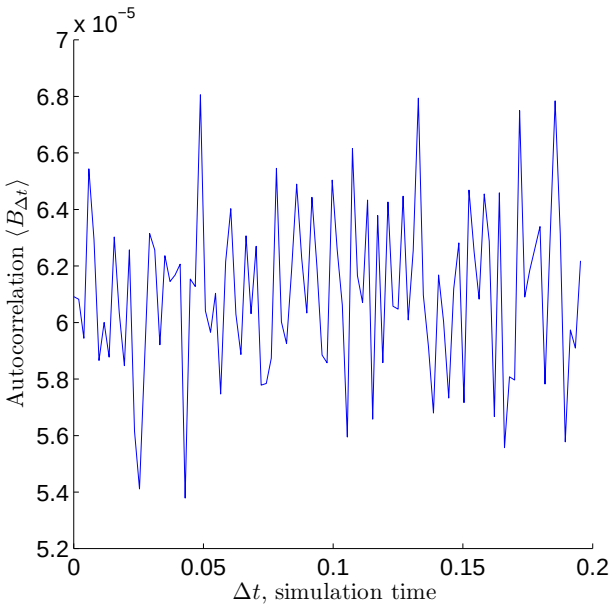

Figure 6.10: Defining the event of filament i has some crosslink on it break at time t, as $B_{i,t}$, its autocorrelation $\langle B_{\Delta t} \rangle$ is plotted over $\Delta t = 0 \sim 0.2$. There is no obvious correlation of same filament crosslink breakage up to $\Delta t = 0.2$.

So from Fig. 6.10 and 6.11, crosslink breakage has spatial correlation but not same filament correlation. To explain this, crosslinks around each broken crosslink is examined right before and after the breakage to see what are the changes in those crosslinks' mechanics. Fig. 6.12 shows four snapshots at different time step of network with each crosslink's force difference (vector) plotted, which is calculated by subtracting each crosslink's force vector before and after a crosslink breakage. Three observations can be made from those figures: first, the force changes in crosslinks around the broken one is smaller but on the same order of the force initially in the broken crosslink before it breaks, which means if the force in the broken crosslink was large enough to make it highly probable to break, after its breaking, the crosslinks right next to it will get higher probability to break too; second, the effect from the broken crosslink is only limited to several crosslinks away, which is consistent with the $3 \times \ell_c$ spatial correlation distance shown in Fig. 6.11; third, the effect from the broken crosslink is transmitted to any filament connected to the crosslink site, without any filament preference. From these observations, a possible explanation is that although there's strong

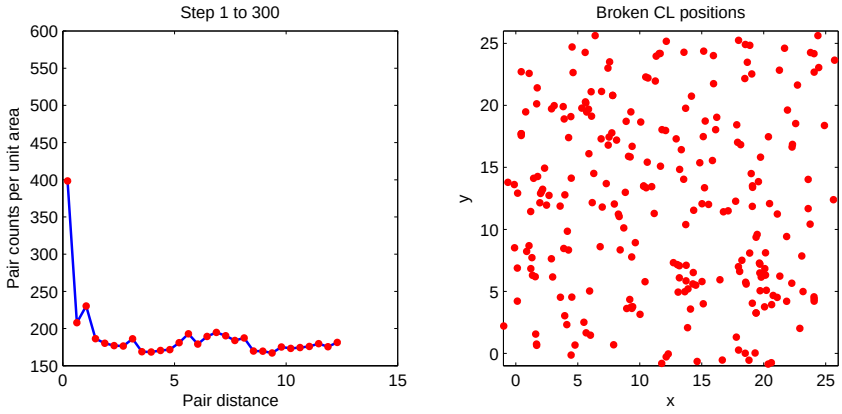

Figure 6.11: Broken crosslink pairs per unit area versus pair distance. Broken crosslink pairs are counted and sorted according to their distance and then normalized by the annulus area cover by the distance range, which in essence represents the probability of the distance between two crosslink breakages during a short time interval (here is 300 simulation time. It clearly shows that there's a spatial correlation between two breakages up to 1 μm apart, which is about 3 times the average crosslink distance ℓ_c

spatial correlation of crosslinks, crosslink may not tend to break on the same filament; the breakage, as shown in Fig. 6.12, always has the opportunity to be passed on from one filament to another filament it connects to. Thus, although crosslinks tend to break close to each other (Fig. 6.11), the broken crosslink effect can be transferred from one filament to another, without any favoribility to stay on the same filament.

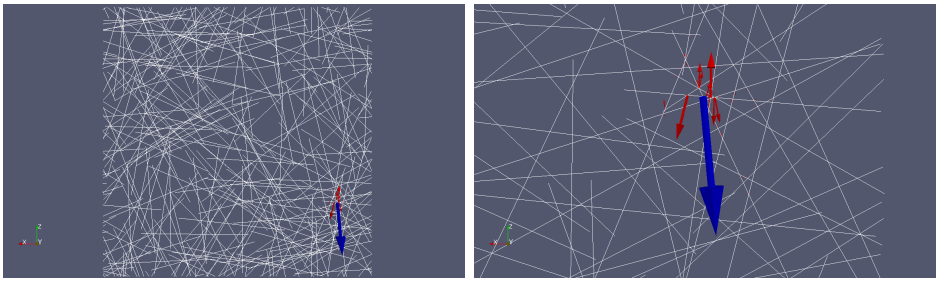

(a) case 1 (simulation time 200)

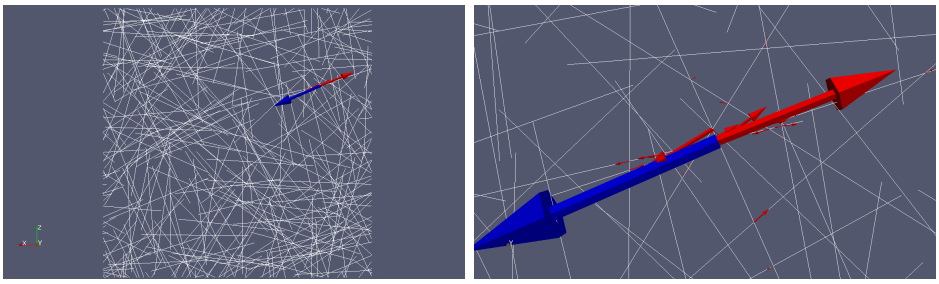

(b) case 2 (simulation time 400)

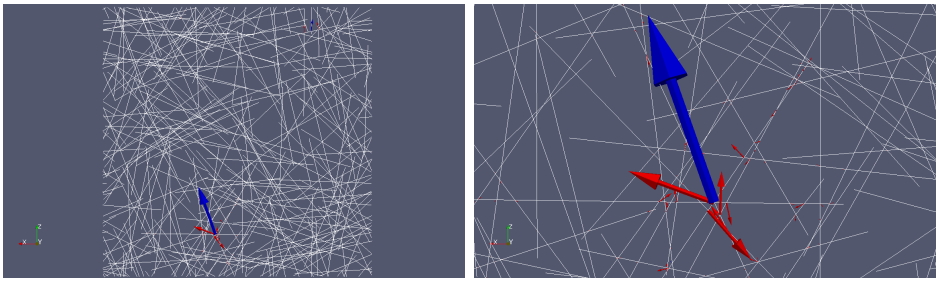

(c) case 3 (simulation time 600)

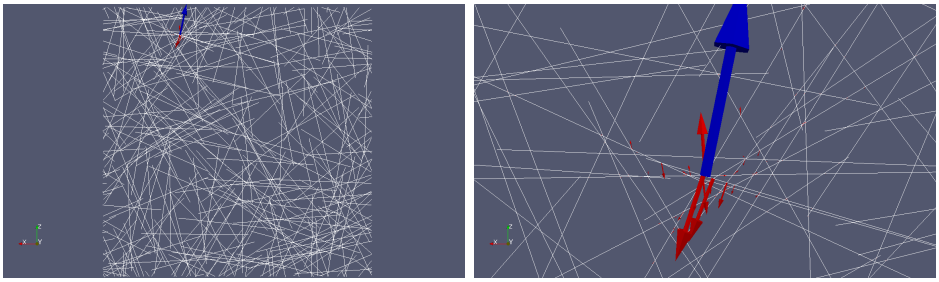

(d) case 4 (simulation time 1000)

Figure 6.12: The *whole network's* crosslinks force change (shown as arrow vectors) before and after one crosslink breakage. The blue arrow is the force change of the broken crosslink; The red arrows are the force changes of all the other bonded crosslinks; Left column shows the whole network, right column shows the details around the broken crosslink site; Note that although all the crosslink's force changes are displayed, most of the crosslinks away from the breakage site barely have any force changes (thus no arrows could be seen for most of the network)

CHAPTER 7

Conclusions and Future Work

7.1 Main Conclusions

This study reports a numerical model of semiflexible filament network using beam and spring elements with peoridic boundary conditions. The mechanical response of network to both displacement and force loading conditions are tested. Networks with length and stiffness polydispersity, anisotropy, and labile crosslinks, which are inspired by both *in vivo* cytoskeleton and *in vitro* filament networks, have been investigated numerically and analytically, and also compared with experimental data. The main conclusions from these numerical studies are summarized as follows:

Length polydispersity, which is prevalent both *in vivo* and *in vitro* semiflexible networks, makes the mean filament length alone not sufficient to determine network's mechanics, especially when the network is in deep nonaffine region. To better quantify the effect of length polydispersity in network's mechanics, bidisperse networks with only long and short filaments are examined. The concept of *mechanical efficiency*: the ratio of the network's shear modulus to its affine prediction as a function of total length density, is introduced. It is found that, network with bidisperse length distribution outperforms monodisperse network in network rigidity when their filament densities are kept the smae. Further examination on network with exponential length distribution found that the broader the distribution of lengths, the stiffer the network. Such broad length distributions proved the most efficient use of the material to create a stiff random structure, which is especially true in deep nonaffine region. In the affine regime, on the other hand, the filament length distribution is irrelevant, if the trivial dangling end effect is removed.

Another type of polydispersity, the stiffness heterogenuity among filaments (e.g. actin filament and microtubule), which commonly seen in the cytoskeleton of cells, represents an ideal test ground for heterogenuous filament networks. Filaments with the same stretching modulus (actin filament) are interconnected to form a network and a small number of them are made much longer and stiffer in bending modulus to represent impurities (microtubules). It is shown that the effect of introducing a small number of stiff impurity filaments can dramatically increase the shear modulus of the network originally in the nonaffine regime and shift the elastic energy storage from being primarily in the bending of the filaments to their stretching. In originally affine networks, the addition of impurities still slightly increases the collective shear modulus of the network, pushing it to the affine limit. This stiffening effect on collective network shear modulus is more significant for networks in the transition region between affine and affine. Deep in the nonaffine region, it is found that the introduction of a low density of impurities produces an increase in the shear modulus of over four orders in magnitude that is nonlinear in the impurity number density. Moreover, when the impurity filaments can store tensile stress they shift the elastic energy storage of the network from bending to stretching modes, more specifically, the impurity filaments stretch other filaments even more but without decreasing their bending energy. For geometric nonaffinity, a sufficient number of impurity filaments will force the nonaffinity into small areas of the network.

Those findings from numerical simulation on polydisperse networks have important implications for experiments on semiflexible networks. It has been long reported that experiments on semiflexible networks didn't find significant affine/nonaffine transition, which is predicted by both analytical and simulation on monodisperse semiflexible networks. This may be very well explained by the fact that most *in vivo* and *in vitro* semiflexible networks are polydiperse and even heterogenous, such that the nonaffine regions predicted by monodisperse network thoery is partially suppressed by polydispersity in networks, both mechanically and geometrically. For example, in the particle tracking experiments designed to explore the deformation field in heterogeneous semiflexible networks, the introduction of stiff impurities may make the network appear to deform affinely if the system's deformation field is not

resolved at a sufficient level of spatial resolution since the regions of nonaffine deformation should become localized in the network.

On the other hand, anisotropic networks with monodisperse filaments, like isotropic networks, undergo an affine to nonaffine cross-over that is controlled solely by L/λ, in a manner independent of anisotropy. The mechanics of affine networks of arbitrary anisotropy can be understood in terms of the usual generalization of isotropic continuum elasticity theory to orthotropic solids, as an extension of the analysis of isotropic, monodisperse network; nonaffine anisotropic networks, however, are more complex. Though the linear elastic response of these nonaffine anisotropic networks can be accounted for by a generalization of the floppy modes analysis, the regime of linear response is vanishingly small; well-oriented and sparse semiflexible networks will thus invariably have a highly nonlinear elastic response dominated by buckling of filaments. Such gels are highly dependent on the orientation of applied loading relative to their nematic axes—more so than can be accounted for by the symmetries of the linear elastic modulus tensor. It is predicted by simulation that these gels with nematic order exhibit stiffening when sheared in the nematic direction in tension and softening in compression.

Adding labile crosslinks that are breakable and reformable to the network makes the model able to predict the network's dynamic response to loading. Creep test to examine the network's viscoelasticiy is performed by marching the network under loading over tens of thousands of time steps. It has been shown that the simple Bell's model is sufficient to model semiflexible gel's viscoelasticity as observed from many *in vitro* experiments. It is found that creep eventually changes the network's initial undeformed state of structure, and whether the network can recover most of its shear strain depends on how many original original crosslinks are left in the network. As a result, the final plastic residual strain is dependent on both loading time and magnitude. It increases with time but decreases with force, which is also found in experiments. The simulation also provides some observations which are not yet available from experiments. The main finding is that there is a strong spatial correlation on crosslink breakage but no transient correlation of crosslink breaking on the same filament, which suggests that the crosslink breakage event does affect nearby

crosslinks and make them more likely to break afterwards, but the breakage spreads through network without any specific direction preference (i.e. along any filament).

7.2 Future Work

The future work on this cytoskeleton model would be focused on extending the network model with labile crosslinks. It has been shown in Chapter 6 that the model with labile crosslinks generates reasonable results predicting network's viscoelastic behavior, which is validated by comparing with experimental data. There are a lot of potentials with this model, and I recommend the following improvement and research:

First, if measurement data is available, it is interesting to see how the results from this model would be compared with experimental data, provided that the actual physical parameters in Bell's model for cytoskeletal crosslinks are used. With the actual measured parameters of crosslinks, there is no need to use the *simulation* time any more, and real time could be used, which will make comparing with actual experimental data possible.

Second, implementing a true, event-driven adaptive time stepping would save more computational time. At this time, the kinetic Monte Carlo method seems to be the most promising method for this application.

Third, the effect of viscous force from fluid solution needs to be added. All cytoskeletal network, both *in vivo* and *in vitro*, are in fluid solution, which affects network's mechanical response by providing viscous damping onto its filaments. It is possible that the lack of transition between network's instantaneous elastic response and its later creeping from simulation, is due to the lack of viscous force in the model.

Lastly, one of many interesting tests the model could perform is to investigate network's dynamic response under oscillating load. The relation between network's dynamic modulus and loading frequency is commonly measured in experiments of *in vitro* filament network, and it will be very interesting to see how will network in this model respond in this test.

Appendix A

Derivation of G_{affine} for Polydisperse Filament Network

We assume that the distribution of filament lengths L in a gel is given by the probability density function $P(L)$, and that the mean filament length $\langle L \rangle$ is finite. Imagine a filament of length L lying along the x-axis. If another filament of length L' is now placed in the system at some random position with some random angle θ, the probability of the two filaments crossing is given by

$$p_{\text{cross}}(L, L', \theta) = \frac{LL'|\sin\theta|}{A}, \tag{A.1}$$

where A is the area of the system. Averaging this probability over the angle θ gives the probability that the first filament is crossed by the second filament:

$$P_{\text{cross}}(L, L') = \frac{2LL'}{\pi A}. \tag{A.2}$$

This quantity can then be averaged over the length of the second filament L' to produce $P_{\text{cross}}(L)$, which is simply the probability that a second filament (with its length chosen from the distribution $P(L)$) placed randomly in the system intersects the first filament:

$$P_{\text{cross}}(L) = \frac{2L\langle L \rangle}{\pi A}. \tag{A.3}$$

If there are $N \gg 1$ filaments in the system, then the probability distribution for the number of crosslinks on a filament of length L is given by the binomial distribution with N trials and a success probability $P_{\text{cross}}(L)$ as

$$p_n(L) = \frac{[P_{\text{cross}}(L)]^n \, [1 - P_{\text{cross}}(L)]^{N-n} \, N!}{(N-n)!n!}. \tag{A.4}$$

To simplify this, take the natural logarithm of $p_n(L)$, and using Stirling's Approximation $\ln(n!) \approx n\ln(n) - n$, which yields

$$\begin{aligned}\ln(p_n(L)) &\approx n\ln\left[P_{\text{cross}}(L)\right] + (N-n)\ln\left[1 - P_{\text{cross}}(L)\right] + N\ln(N) - N - (N-n)\ln(N-n) \\ &\quad +N - n - n\ln(n) + n \\ &= n\ln\left[P_{\text{cross}}(L)\right] + (N-n)\ln\left[1 - P_{\text{cross}}(L)\right] + N\ln(N) \\ &\quad -(N-n)\ln(N-n) - n\ln(n) \end{aligned} \tag{A.5}$$

Note that $P_{\text{cross}}(L) \ll 1$, so by Taylor expansion at 1, $\ln\left[1 - P_{\text{cross}}(L)\right]$ can be approximated by $-P_{\text{cross}}(L)$. Also, considering $N \gg n$, the above equation can be written as

$$\begin{aligned}\ln(p_n(L)) &\approx n\ln\left[P_{\text{cross}}(L)\right] - (N-n)P_{\text{cross}}(L) + N\ln(N) - (N-n)\ln(N-n) - n\ln(n) \\ &= n\ln\left[P_{\text{cross}}(L)\right] - (N-n)P_{\text{cross}}(L) - N\ln(\frac{N-n}{N}) + n\ln(\frac{N-n}{n}) \\ &\approx n\ln\left[P_{\text{cross}}(L)\right] - NP_{\text{cross}}(L) + n\ln(\frac{N}{n}) \end{aligned} \tag{A.6}$$

Thus, getting back to $p_n(L)$ and applying $n^n \approx n!$ yields

$$\begin{aligned} p_n(L) &\approx \left[P_{\text{cross}}(L)\right]^n e^{-NP_{\text{cross}}(L)} - (\frac{N}{n})^n \\ &\approx \frac{\left[NP_{\text{cross}}(L)\right]^n e^{-NP_{\text{cross}}(L)}}{n!} \end{aligned} \tag{A.7}$$

Thus, it's shown that since N is large and $P_{\text{cross}}(L)$ is expected to be small, the binomial distribution can be approximated by the exponential distribution with parameter $\lambda(L) = NP_{\text{cross}}(L)$. That is, we take the probability $p_n(L)$ that a filament of length L is crosslinked n times to be

$$p_n(L) = \frac{e^{-\lambda(L)}\left[\lambda(L)\right]^n}{n!}, \tag{A.8}$$

with $\lambda(L) = 2\rho L\langle L\rangle/\pi$ and $\rho = N/A$.

Now we are in a position to calculate ℓ_c, the mean distance between crosslinks. This quantity is equal to the average total distance between crosslinks pairs Λ_c divided by the

mean number of crosslink pairs N_c. These quantities are given by:

$$\begin{aligned}\Lambda_c &= \int_0^\infty dL\, P(L) \sum_{n=2}^{\infty} p_n(L)\, L\, \frac{n-1}{n+1};\\ N_c &= \int_0^\infty dL\, P(L) \sum_{n=2}^{\infty} p_n(L)(n-1).\end{aligned} \tag{A.9}$$

Noting Taylor expansion

$$e^\lambda = \sum_{n=0}^{\infty} \frac{\lambda^n}{n!} \tag{A.10}$$

Then, the sums can be done exactly as follows

$$\begin{aligned}\sum_{n=2}^{\infty} p_n(L)\frac{n-1}{n+1} &= \sum_{n=2}^{\infty} \frac{e^{-\lambda(L)}\,[\lambda(L)]^n}{n!}\,\frac{n-1}{n+1}\\ &= e^{-\lambda}\sum_{n=2}^{\infty}\frac{\lambda^n}{n!}(1-\frac{2}{n+1})\\ &= e^{-\lambda}\left[\sum_{n=2}^{\infty}\frac{\lambda^n}{n!} - \frac{2}{\lambda}\sum_{n=3}^{\infty}\frac{\lambda^n}{n!}\right]\\ &= e^{-\lambda}\left[e^\lambda - 1 - \lambda - \frac{2}{\lambda}(e^\lambda - 1 - \lambda - \frac{\lambda^2}{2})\right]\\ &= 1 + e^{-\lambda} - \frac{2}{\lambda}(1-e^{-\lambda})\end{aligned} \tag{A.11}$$

The average total distance between crosslinks pairs Λ_c then can be written as

$$\begin{aligned}\Lambda_c &= \int_0^\infty dL\, P(L)\, L\, \left[1 + e^{-\lambda} - \frac{2}{\lambda}(1-e^{-\lambda})\right]\\ &= \langle L\rangle + \langle L e^{-\lambda}\rangle - \int_0^\infty dL\, P(L)\,\frac{2L}{\lambda}(1-e^{-\lambda})\end{aligned} \tag{A.12}$$

Note $\lambda(L) = 2\rho L\langle L\rangle/\pi$, thus L/λ is not dependent on L and can be taken out of the integral. So

$$\Lambda_c = \langle L\rangle + \langle L e^{-\lambda}\rangle - \frac{2\langle L\rangle}{\langle\lambda\rangle}(1-\langle e^{-\lambda}\rangle) \tag{A.13}$$

Likewise, the mean number of crosslink pairs N_c can be calculated exactly as

$$N_c = \langle\lambda\rangle - 1\langle e^{-\lambda}\rangle \tag{A.14}$$

Finally, Eq. (A.13) and (A.14) lead to the following expression for the ratio $\langle L\rangle/\ell_c$:

$$\frac{\langle L\rangle}{\ell_c} = \frac{\langle L\rangle\left[\langle\lambda(L)\rangle - \left(1-\langle e^{-\lambda(L)}\rangle\right)\right]}{\langle L\rangle + \langle L e^{-\lambda(L)}\rangle - \frac{2\langle L\rangle}{\langle\lambda(L)\rangle}\left(1-\langle e^{-\lambda(L)}\rangle\right)}, \tag{A.15}$$

where the brackets denote averaging over filaments lengths with the weight $P(L)$ and $\langle\lambda(L)\rangle = 2\rho\langle L\rangle^2/\pi$. For the case of a monodisperse network, this reduces to the formula derived by Head *et al.*:

$$\left.\frac{L}{\ell_c}\right|_{\text{monodisperse}} = \frac{\lambda - (1-e^{-\lambda})}{1 + e^{-\lambda} - \frac{2}{\lambda}(1-e^{-\lambda})} \tag{A.16}$$

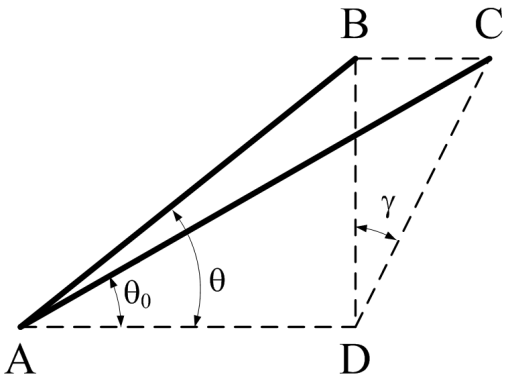

Figure A.1: Schematic of a single filament in undeformed and deformed states

The calculation of G_{affine}, and indeed all of the elastic constants, proceeds in a similar manner. Consider a single filament of length L with angle θ_0 in the undeformed network (Fig. A.1).We must sum over filament orientations and lengths and average over the number of crosslinks to get the affine modulus:

$$G_{\text{affine}} = \mu\rho \int_0^\infty dL\, P(L)\, \frac{1}{2\pi} \int_0^{2\pi} d\theta\, \sin^2\theta \cos^2\theta \sum_{n=2}^{\infty} p_n(L)\, L\, \frac{n-1}{n+1}, \tag{A.17}$$

where μ is the stretching modulus. Performing the sum and the integrals leads to

$$G_{\text{affine}} = \frac{\mu\rho}{8}\left[\langle L\rangle + \langle L e^{-\lambda(L)}\rangle - \frac{2\langle L\rangle}{\langle\lambda(L)\rangle}\left(1 - \langle e^{-\lambda(L)}\rangle\right)\right]. \tag{A.18}$$

We can also express this in terms of the mean crosslink separation ℓ_c:

$$G_{\text{affine}} = \frac{\mu\rho\ell_c}{8}\left[\langle\lambda(L)\rangle - (1 - \langle e^{-\lambda(L)}\rangle)\right]. \tag{A.19}$$

We refer to the above as the affine prediction for the shear modulus of our polydisperse networks.

Appendix B

Derivation of G_{affine} for Anisotropic Filament Network

The procedure for calculating the elastic constants of an affinely-deforming anisotropic gel is very similar to that presented in the previous section for a polydisperse gel. The major difference is that an anisotropic gel in two dimensions is characterized by four elastic constants rather than two; therefore, we will need to consider expansion deformations as well as shear deformations in order to fully characterize the material.

We start by again considering a straight filament of length L lying down in the plane. Because the rotational symmetry of the isotropic gel is now broken, we will need to specify the angle θ this filament makes with the nematic direction. If we now place a second filament down at some angle ϕ with respect to the first filament, the probability of the two filaments crossing is

$$p_{\text{cross}}(\theta, \phi) = \frac{L^2 |\sin \phi|}{A}. \tag{B.1}$$

In order to obtain the crossing probability independent of the relative angle ϕ, we need to integrate the above quantity over ϕ with a weight $P(\theta + \phi)$, where $P(x)$ is the angular probability distribution. Doing this gives:

$$P_{\text{cross}}(\theta) = \frac{2L^2}{A} \int_0^\pi d\phi \, \sin \phi \, P(\theta + \phi). \tag{B.2}$$

This quantity is simply the probability that a given filament oriented with angle θ to the nematic direction is crossed by a second filament with its direction chosen from the angular probability distribution and its position chosen randomly. We will again assume that our system contains a large number of filaments N in a large area A, so that $P_{\text{cross}}(\theta)$ is small; in this limit, the probability distribution $p_n(\theta)$ for the number of crosslinks on a filament

oriented with angle θ to the nematic direction is simply

$$p_n = \frac{e^{-\lambda(\theta)}\,[\lambda(\theta)]^n}{n!}, \tag{B.3}$$

where

$$\lambda(\theta) \equiv N P_{\rm cross}(\theta) = 2\rho L^2 \int_0^\pi d\phi\, \sin\phi\, P(\theta+\phi). \tag{B.4}$$

In the above equation, $\rho = N/A$ is the number density of filaments. Note that $\lambda(\theta)$ is simply the mean number of crosslinks on a filament oriented with angle θ.

The calculation of L/ℓ_c is similar to the one already shown for a polydisperse network. The mean crosslink distance ℓ_c is once again identified as the average total distance between crosslink pairs Λ_c divided by the mean number of crosslinks pairs N_c:

$$\begin{aligned} \Lambda_c &= NL \int_0^{2\pi} d\theta\, P(\theta) \sum_{n=2}^{\infty} p_n(\theta)\, \frac{n-1}{n+1}; \\ N_c &= N \int_0^{\infty} d\theta\, P(\theta) \sum_{n=2}^{\infty} p_n(\theta)(n-1). \end{aligned} \tag{B.5}$$

The quantity L/ℓ_c is thus

$$\frac{L}{\ell_c} = \frac{\langle\lambda\rangle - \left(1 - \langle e^{-\lambda}\rangle\right)}{1 + \langle e^{-\lambda}\rangle - 2\left(\langle\frac{1}{\lambda}\rangle - \langle\frac{e^{-\lambda}}{\lambda}\rangle\right)}, \tag{B.6}$$

where the angle brackets denote averaging with the weight $P(\theta)$.

Now that we have found an expression for L/ℓ_c in an anisotropic network, we can turn to the calculation of the elastic constants for the case of affine deformations. We will first calculate the shear modulus G for the case where the shear direction—defined in Fig. B.1—makes an angle ϕ with the nematic direction. That is, we assume that we are shearing the gel so that the shear direction is $+x$ and the nematic director points at an angle ϕ with respect to the x direction. A crosslinked filament segment of length dL oriented at angle ψ with respect to the x-axis contributes an energy $\mu\, dL\gamma^2 \cos^2\psi \sin^2\psi/2$ upon shearing, so the total energy density can be written as:

$$E(\phi) = \frac{\mu\rho\gamma^2}{2} \int_0^{2\pi} d\psi\, P(\psi-\phi) \sin^2\psi \cos^2\psi \sum_{n=2}^{\infty} p_n(\psi-\phi) L \frac{n-1}{n+1}. \tag{B.7}$$

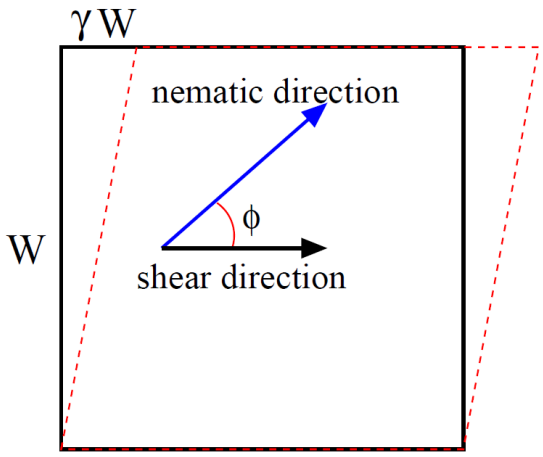

Figure B.1: Definition of the shear direction and the angle ϕ between the shear and nematic directions. Note that due to the nematic order of the sysem, all elastic constants that depend on ϕ must remain the same as $\phi \to \phi \pm \pi$,

Using the fact that $E(\phi) = G(\phi)\gamma^2/2$ for small shear, we can write the affine shear modulus as:

$$G_{\text{affine}}(\phi) = \mu\rho L \int_{-\phi}^{-\phi+2\pi} d\theta\, P(\theta) \sin^2(\theta+\phi) \cos^2(\theta+\phi) \sum_{n=2}^{\infty} p_n(\theta) \frac{n-1}{n+1}, \tag{B.8}$$

where we have switched integration variables to $\theta = \psi - \phi$. We can use standard trig identities to expand out the $\sin(\theta+\phi)$ and $\cos(\theta+\phi)$ terms, leading, after some rearranging, to the following expression for $G_{\text{affine}}(\phi)$:

$$G_{\text{affine}}(\phi) = G_{\text{affine}}(0) \left[1 - 8\sin^2\phi\cos^2\phi\right] + \Delta \sin^2\phi\cos^2\phi \tag{B.9}$$

where

$$\Delta = \mu\rho L \int_{0}^{2\pi} d\theta\, P(\theta) \sum_{n=2}^{\infty} p_n(\theta) \frac{n-1}{n+1},$$

and $G_{\text{affine}}(0)$ is the affine shear modulus for the case where the shear direction is parallel to the nematic direction. Note that $G_{\text{affine}}(\phi)$ is unchanged under $\phi \to \phi \pm \pi$ *and* under $\phi \to \phi \pm \pi/2$. This latter symmetry is simply a restatement of the fact that a two-dimensional anisotropic continuum solid has only one shear modulus.

SPECIAL NOTE: The filament angle distribution $P(\theta)$ should have certain properties: first, it must be symmetric under $\theta \to -\theta$; second, it must be symmetric under $\theta \to \theta \pm n\pi$,

where n is some integer; finally, it should produce a nematic order parameter S according to

$$S = \int_0^{2\pi} d\theta \, P(\theta) \cos 2\theta. \tag{B.10}$$

We have been using the following distribution in our simulations:

$$P(\theta) = \frac{e^{\alpha \cos 2\theta}}{2\pi I_0(\alpha)}, \tag{B.11}$$

where $I_0(\alpha)$ is the modified Bessel function of the first kind of order 0. It is possible to analytially calculate a few of the quantities discussed in this paper using this distribution. First off, the nematic order parameter is given by:

$$S = \frac{I_1(\alpha)}{I_0(\alpha)}. \tag{B.12}$$

For a given S, one only needs to solve this simple equation numerically to determine the parameter α. Second, the quantity $\lambda(\theta)$ is given, for this filament angle PDF, by

$$\lambda(\theta) = \frac{\rho L^2}{\sqrt{2\pi\alpha}\, I_0(\alpha)} \left[e^{-\alpha} \cos\theta \, \mathrm{erfi}(\sqrt{2\alpha}\cos\theta) + e^{\alpha} \sin\theta \, \mathrm{erf}(\sqrt{2\alpha}\sin\theta) \right], \tag{B.13}$$

where $\mathrm{erf}(x)$ and $\mathrm{erfi}(x)$ are the error and imaginary error functions, respectively.

Appendix C

Probability Distribution of Dangling Ends

In this appendix we will derive the probability distribution for the dangling end length mentioned at the end of Section 4.2. Imagine a filament of length L with $n \geq 2$ crosslinks. We begin by noting that the probability that *no* crosslinks exist within a distance s_1 of one end of the filament and s_2 of the other end of the filament is given by $[1-(s_1+s_2)/L]^n$. Taking the derivative with respect to s_1 and again with respect to s_2 gives the joint probability density for having the outermost crosslinks on the filament at distances s_1 and s_2 from the ends. This probability is given by:

$$p(s_1, s_2, L, n) = \frac{n(n-1)}{L^2}\left[1 - \frac{s_1+s_2}{L}\right]^{n-2}$$

Integrating across s_1 and s_2 subject to the constraints $L-(s_1+s_2) = L_{\text{mech}}$ and, of course, $s_1+s_2 \leq L$ results in a probability density for the mechanically relevant filament length L_{mech} as a function of L and n:

$$p(L_{\text{mech}}, L, n) = \frac{n(n-1)}{L^2}\left(\frac{L_{\text{mech}}}{L}\right)^{n-2}(L - L_{\text{mech}})\,.$$

To arrive at a probability density that is independent of the number of crosslinks, we must sum over n with the weight $p_n(L)$ given in Eq. 3.2. This results in the probability distribution for the mechanical length of a filament of length L that is crosslinked at least twice; from this, it is trivial to derive the probability distribution for having a dangling end length of L_{end} given a filament length of L:

$$p(L_{\text{end}}, L) = \frac{\omega^2 L_{\text{end}} e^{-\omega L_{\text{end}}/L}}{L^2[1-e^{-\omega}(1+\omega)]},$$

where $\omega(L) = 2\rho L\langle L\rangle/\pi$, with ρ the total number density of filaments and $\langle L\rangle$ the mean filament length.

References

[1] J. Howard, *Mechanics of Motor Proteins and the Cytoskeleton*, Sinauer Associates, Inc, Sunderland, MA, 2001.

[2] M.A. Geeves and K.C. Holmes, "Structural mechanism of muscle contraction", *Annu. Rev. Biochem*, vol. 68, pp. 687–728, 1999.

[3] E. Nogales, M. Whittaker, R.A. Milligan, and K.H. Downing, "High-resolution model of the microtubule", *Cell*, vol. 96, pp. 79–88, 1999.

[4] Y. Yang, M. Bai, W.S. Klug, A.J. Levine, and M.T. Valentine, "Microrheology of highly crosslinked microtubule networks is dominated by force-induced crosslinker unbinding", *Soft Matter*, Accepted for publication.

[5] H.T. Higuchi, T. Yanagida, and Y.E. Goldman, "Compliance of thin filaments in skinned fibers of rabbit skeletal muscle", *Biophys. J.*, vol. 69, pp. 1000–1010, 1995.

[6] J. Howard and A.J. Hudspeth, "Mechanical relxation of the hair bundle mediates adaptation in mechanoelectrical transduction by the bullfrog's saccular hair cell", *Proc. Natl. Acad. Sci. USA*, vol. 84, pp. 3064–3068, 1987.

[7] J. Howard and J.F. Ashmore, "Stiffness of sensory hair bundles in the sacculus of the frog", *Hear. Res.*, vol. 23, pp. 93–104, 1986.

[8] M. Okuno and Y. Hiramoto, "Direct measurements of the stiffness of echinoderm sperm flagella", *J. Exp. Biol.*, vol. 79, pp. 235–243, 1979.

[9] F. Gittes, B. Mickey, J. Nettleton, and J. Howard, "Flexural rigidity of microtubules and actin filaments measured from thermal fluctuations in shape", *J. Cell Biol.*, vol. 120, pp. 923–934, 1993.

[10] S. Heins, P.C. Wong, S. Muller, K. Goldie, D.W. Cleveland, and U. Aebi, "The rod domain of nf-l determines neurofilament architecture, whereas the end domains specify filament assembly and network formation", *J. Cell Biol.*, vol. 123, pp. 1517–1533, 1993.

[11] M.R.K. Mofrad and R.D. Kamm, *Cytoskeletal Mechanics, models and measurements*, Cambridge University Press, New York, 2006.

[12] J.L. Drury and M. Dembo, "Aspiration of human neutrophils: effects of shear thinning and cortical dissipation", *Biophys. J.*, vol. 81(6), pp. 3166–3177, 2001.

[13] F.P.T. Baaijens, W.R. Trickey, T.A. Laursen, and F. Guilak, "Large deformation finite element analysis of micropipette aspiration to determine the mechanical properties of the chondrocyte", *An. Biomed. Eng.*, vol. 33, pp. 494–501, 2005.

[14] R.B. Fuller, "Tensegrity", *Portfolio Artnews Annual*, vol. 4, pp. 112–127, 1961.

[15] D.E. Ingber and J.D. Jameison, *Cells as tensegrity structures: Architectural regulation of histodifferentiation by physical forces transduced over basement membrane. In: Gene Expression during Normal and Malignant Differentiation*, Academic Press, Orlando, FL, 1981.

[16] D. Stamenovic, "Microtubules may harden or soften cells, depending on the extent of cell distension", *J. Biomech.*, vol. 38, pp. 1728–1732, 2005.

[17] F.C. MacKintosh, J. Kas, and P.A. Janmey, "Elasticity of semiflexible biopolymer networks", *Phys. Rev. Lett*, vol. 75, pp. 4425, 1995.

[18] D.A. Head, A.J. Levine, and F.C. MacKintosh, "Deformation of cross-linked semiflexible polymer networks", *Phys. Rev. Lett*, vol. 91, pp. 108102, 2003.

[19] D.A. Head, A.J. Levine, and F.C. MacKintosh, "Distinct regimes of elastic response and deformation modes of cross-linked cytoskeletal and semiflexible polymer networks", *Phys. Rev. E*, vol. 68, pp. 061907, 2003.

[20] M. Rubinstein and R.H. Colby, *Polymer physics*, Oxford University Press, USA, 2003.

[21] O. Breuer and U. Sundararaj, "Big returns from small fibers: a review of polymer/carbon nanotube composites", *Polymer composites*, vol. 25, no. 6, pp. 630–645, 2004.

[22] J.N. Coleman, U. Khan, and Y.K. Gun'ko, "Mechanical reinforcement of polymers using carbon nanotubes", *Advanced materials*, vol. 18, no. 6, pp. 689–706, 2006.

[23] P.A. Janmey and D.A. Weitz, "Dealing with mechanics: mechanisms of force transduction in cells", *Trends in biochemical sciences*, vol. 29, no. 7, pp. 364–370, 2004.

[24] ML Gardel, F. Nakamura, JH Hartwig, JC Crocker, TP Stossel, and DA Weitz, "Prestressed F-actin networks cross-linked by hinged filamins replicate mechanical properties of cells", *Proceedings of the National Academy of Sciences*, vol. 103, no. 6, pp. 1762, 2006.

[25] AR Bausch and K. Kroy, "A bottom-up approach to cell mechanics", *Nature Physics*, vol. 2, no. 4, pp. 231–238, 2006.

[26] P.A. Janmey and C.A. McCulloch, "Cell mechanics: integrating cell responses to mechanical stimuli", *Annual Review of Biomedical Engineering*, vol. 9, pp. 1–34, 2007.

[27] T.P. Stossel, J. Condeelis, L. Cooley, J.H. Hartwig, A. Noegel, M. Schleicher, and S.S. Shapiro, "Filamins as integrators of cell mechanics and signalling", *Nature Reviews Molecular Cell Biology*, vol. 2, no. 2, pp. 138–145, 2001.

[28] DH Wachsstock, WH Schwarz, and TD Pollard, "Cross-linker dynamics determine the mechanical properties of actin gels", *Biophysical journal*, vol. 66, no. 3P1, pp. 801–809, 1994.

[29] D Mizuno, C Tardin, CF Schmidt, and FC MacKintosh, "Nonequilibrium mechanics of active cytoskeletal networks", *Science*, vol. 315, no. 5810, pp. 370, 2007.

[30] ML Gardel, JH Shin, FC MacKintosh, L. Mahadevan, P. Matsudaira, and DA Weitz, "Elastic behavior of cross-linked and bundled actin networks", *Science*, vol. 304, no. 5675, pp. 1301, 2004.

[31] F. Gittes, B. Schnurr, PD Olmsted, FC MacKintosh, and CF Schmidt, "Microscopic viscoelasticity: shear moduli of soft materials determined from thermal fluctuations", *Physical Review Letters*, vol. 79, no. 17, pp. 3286–3289, 1997.

[32] D. Humphrey, C. Duggan, D. Saha, D. Smith, and J. Käs, "Active fluidization of polymer networks through molecular motors", *Nature*, vol. 416, no. 6879, pp. 413–416, 2002.

[33] KM Schmoller, O. Lieleg, and AR Bausch, "Cross-linking molecules modify composite actin networks independently", *Physical review letters*, vol. 101, no. 11, pp. 118102, 2008.

[34] FC MacKintosh, J. Käs, and PA Janmey, "Elasticity of semiflexible biopolymer networks", *Physical Review Letters*, vol. 75, no. 24, pp. 4425–4428, 1995.

[35] D.A. Head, A.J. Levine, and FC MacKintosh, "Deformation of cross-linked semiflexible polymer networks", *Physical review letters*, vol. 91, no. 10, pp. 108102, 2003.

[36] DA Head, AJ Levine, and FC MacKintosh, "Distinct regimes of elastic response and deformation modes of cross-linked cytoskeletal and semiflexible polymer networks", *Physical Review E*, vol. 68, no. 6, pp. 61907, 2003.

[37] DA Head, AJ Levine, and FC MacKintosh, "Mechanical response of semiflexible networks to localized perturbations", *Physical Review E*, vol. 72, no. 6, pp. 61914, 2005.

[38] C. Heussinger and E. Frey, "Floppy modes and nonaffine deformations in random fiber networks", *Physical review letters*, vol. 97, no. 10, pp. 105501, 2006.

[39] C. Heussinger, B. Schaefer, and E. Frey, "Nonaffine rubber elasticity for stiff polymer networks", *Physical Review E*, vol. 76, no. 3, pp. 31906, 2007.

[40] MF Thorpe, "Continuous deformations in random networks", *Journal of Non-Crystalline Solids*, vol. 57, no. 3, pp. 355–370, 1983.

[41] L.D. Landau and E.M. Lifshitz, *Theory of Elasticity, Course of Theoretical Physics vol 7*, 1995.

[42] A.R. Missel, M. Bai, W.S. Klug, and A.J. Levine, "Affine-nonaffine transition in networks of nematically ordered semiflexible polymers", *Physical Review E*, vol. 82, no. 4, pp. 041907, 2010.

[43] Y-C. Lin, G.H. Koenkerink, F.C. MacKintosh, and D.A Weitz, "Control of nonlinear elasticity in actin networks with microtubules", Submitted to *Soft Matter.*, 2010.

[44] M. Bai, A.R. Missel, W.S. Klug, and A.J. Levine, "The mechanics and affine–nonaffine transition in polydisperse semiflexible networks", *Soft Matter*, vol. 7, no. 3, pp. 907–914, 2011.

[45] KE Kasza, CP Broedersz, GH Koenderink, YC Lin, W. Messner, EA Millman, F. Nakamura, TP Stossel, FC MacKintosh, and DA Weitz, "Actin Filament Length Tunes Elasticity of Flexibly Cross-Linked Actin Networks", *Biophysical Journal*, vol. 99, no. 4, pp. 1091–1100, 2010.

[46] BA DiDonna and A.J. Levine, "Unfolding cross-linkers as rheology regulators in F-actin networks", *Physical Review E*, vol. 75, no. 4, pp. 41909, 2007.

[47] CP Broedersz, C. Storm, and FC MacKintosh, "Effective-medium approach for stiff polymer networks with flexible cross-links", *Physical Review E*, vol. 79, no. 6, pp. 61914, 2009.

[48] P.A. Janmey, U. Euteneuer, P. Traub, and M. Schliwa, "Viscoelastic properties of vimentin compared with other filamentous biopolymer networks.", *The Journal of cell biology*, vol. 113, no. 1, pp. 155, 1991.

[49] C. Storm, J.J. Pastore, F.C. MacKintosh, T.C. Lubensky, and P.A. Janmey, "Nonlinear elasticity in biological gels", *Nature*, vol. 435, no. 7039, pp. 191–194, 2005.

[50] J. Xu, D. Wirtz, and T.D. Pollard, "Dynamic cross-linking by α-actinin determines the mechanical properties of actin filament networks", *Journal of Biological Chemistry*, vol. 273, no. 16, pp. 9570, 1998.

[51] JH Shin, ML Gardel, L. Mahadevan, P. Matsudaira, and DA Weitz, "Relating microstructure to rheology of a bundled and cross-linked F-actin network in vitro", *Proceedings of the National Academy of Sciences*, vol. 101, no. 26, pp. 9636, 2004.

[52] T. Gisler and D.A. Weitz, "Scaling of the microrheology of semidilute F-actin solutions", *Physical Review Letters*, vol. 82, no. 7, pp. 1606–1609, 1999.

[53] D. Stamenović, N. Rosenblatt, M. Montoya-Zavala, B.D. Matthews, S. Hu, B. Suki, N. Wang, and D.E. Ingber, "Rheological behavior of living cells is timescale-dependent", *Biophysical journal*, vol. 93, no. 8, pp. 39–41, 2007.

[54] L. Deng, X. Trepat, J.P. Butler, E. Millet, K.G. Morgan, D.A. Weitz, and J.J. Fredberg, "Fast and slow dynamics of the cytoskeleton", *Nature Materials*, vol. 5, no. 8, pp. 636–640, 2006.

[55] J.J. Fredberg and R.D. Kamm, "Stress transmission in the lung: pathways from organ to molecule", *Annu. Rev. Physiol*, vol. 68, pp. 507–41, 2006.

[56] D. Wirtz, "Particle-tracking microrheology of living cells: principles and applications", *Annual review of biophysics*, vol. 38, pp. 301–326, 2009.

[57] Y. Tseng, T.P. Kole, and D. Wirtz, "Micromechanical mapping of live cells by multiple-particle-tracking microrheology", *Biophysical journal*, vol. 83, no. 6, pp. 3162–3176, 2002.

[58] X. Trepat, L. Deng, S.S. An, D. Navajas, D.J. Tschumperlin, W.T. Gerthoffer, J.P. Butler, and J.J. Fredberg, "Universal physical responses to stretch in the living cell", *Nature*, vol. 447, no. 7144, pp. 592–595, 2007.

[59] AWC Lau, B.D. Hoffman, A. Davies, J.C. Crocker, and T.C. Lubensky, "Microrheology, stress fluctuations, and active behavior of living cells", *Physical review letters*, vol. 91, no. 19, pp. 198101, 2003.

[60] AW Lees and SF Edwards, "The computer study of transport processes under extreme conditions", *Journal of Physics C: Solid State Physics*, vol. 5, pp. 1921–1928, 1972.

[61] R.H. Byrd, P. Lu, J. Nocedal, and C. Zhu, "A limited memory algorithm for bound constrained optimization", *SIAM J. Scientific Computing*, vol. 16, no. 5, pp. 1190–1208, 1995.

[62] C. Zhu, R.H. Byrd, P. Lu, and J. Nocedal, "Algorithm 778: L-BFGS-B: Fortran subroutines for large-scale bound-constrained optimization", *ACM Transactions on Mathematical Software (TOMS)*, vol. 23, no. 4, pp. 550–560, 1997.

[63] B. Wagner, R. Tharmann, I. Haase, M. Fischer, and AR Bausch, "Cytoskeletal polymer networks: The molecular structure of cross-linkers determines macroscopic properties", *Proceedings of the National Academy of Sciences*, vol. 103, no. 38, pp. 13974, 2006.

[64] J. Liu, GH Koenderink, KE Kasza, FC MacKintosh, and DA Weitz, "Visualizing the strain field in semiflexible polymer networks: Strain fluctuations and nonlinear rheology of F-actin gels", *Physical review letters*, vol. 98, no. 19, pp. 198304, 2007.

[65] J. Wilhelm and E. Frey, "Elasticity of stiff polymer networks", *Physical review letters*, vol. 91, no. 10, pp. 108103, 2003.

[66] C. Heussinger and E. Frey, "Stiff polymers, foams, and fiber networks", *Physical review letters*, vol. 96, no. 1, pp. 17802, 2006.

[67] C. Heussinger and E. Frey, "Role of architecture in the elastic response of semiflexible polymer and fiber networks", *Physical Review E*, vol. 75, no. 1, pp. 11917, 2007.

[68] C. Heussinger and E. Frey, "Force distributions and force chains in random stiff fiber networks", *Eur. Phys. J. E*, vol. 24, no. 1, pp. 47–53, sep 2007.

[69] Moumita Das, F. C. MacKintosh, and Alex J. Levine, "Effective medium theory of semiflexible filamentous networks", *Phys. Rev. Lett.*, vol. 99, no. 3, pp. 038101, Jul 2007.

[70] D. Sept, J. Xu, T.D. Pollard, and J. Andrew McCammon, "Annealing accounts for the length of actin filaments formed by spontaneous polymerization", *Biophysical journal*, vol. 77, no. 6, pp. 2911–2919, 1999.

[71] I. Fujiwara, S. Takahashi, H. Tadakuma, T. Funatsu, and S. Ishiwata, "Microscopic analysis of polymerization dynamics with individual actin filaments", *Nature cell biology*, vol. 4, no. 9, pp. 666–673, 2002.

[72] J. Viamontes, S. Narayanan, A.R. Sandy, and J.X. Tang, "Orientational order parameter of the nematic liquid crystalline phase of F-actin", *Physical Review E*, vol. 73, no. 6, pp. 61901, 2006.

[73] H. Bolterauer, H.J. Limbach, and JA Tuszyski, "Microtubules: strange polymers inside the cell", *Bioelectrochemistry and Bioenergetics*, vol. 48, no. 2, pp. 285–295, 1999.

[74] M. Bai, A.R. Missel, A.J. Levine, and W.S. Klug, "On the role of the filament length distribution in the mechanics of semiflexible networks", *Acta Biomaterialia*, vol. 7, no. 5, pp. 2109–2118, 2011.

[75] DA Head, FC MacKintosh, and AJ Levine, "Nonuniversality of elastic exponents in random bond-bending networks", *Physical Review E*, vol. 68, pp. 025101(R), 2003.

[76] C. Heussinger, M. Bathe, and E. Frey, "Statistical mechanics of semiflexible bundles of wormlike polymer chains", *Physical Review Letters*, vol. 99, no. 4, pp. 48101, 2007.

[77] PR Onck, T. Koeman, T. Van Dillen, and E. Van der Giessen, "Alternative explanation of stiffening in cross-linked semiflexible networks", *Physical review letters*, vol. 95, no. 17, pp. 178102, 2005.

[78] T. van Dillen, PR Onck, and E. Van der Giessen, "Models for stiffening in cross-linked biopolymer networks: A comparative study", *Journal of the Mechanics and Physics of Solids*, vol. 56, no. 6, pp. 2240–2264, 2008.

[79] A. Kabla and L. Mahadevan, "Nonlinear mechanics of soft fibrous networks", *Journal of The Royal Society Interface*, vol. 4, no. 12, pp. 99, 2007.

[80] M. Wyart, H. Liang, A. Kabla, and L. Mahadevan, "Elasticity of floppy and stiff random networks", *Physical review letters*, vol. 101, no. 21, pp. 215501, 2008.

[81] ME Cates and SF Edwards, "Linear theory of disordered fibre-reinforced composites", *Proceedings of the Royal Society of London. Series A, Mathematical and Physical Sciences*, pp. 89–109, 1984.

[82] R. Kaunas, P. Nguyen, S. Usami, and S. Chien, "Cooperative effects of rho and mechanical stretch on stress fiber organization", *Proceedings of the National Academy of Sciences of the United States of America*, vol. 102, no. 44, pp. 15895–15900, 2005.

[83] P. Mohazzabi and F. Behroozi, "Elastic Behavior of Anisotropic Monolayers", *Langmuir*, vol. 14, no. 4, pp. 904–909, 1998.

[84] P.M. Chaikin, T.C. Lubensky, and T.A. Witten, *Principles of condensed matter physics*, vol. 1, Cambridge Univ Press, 2000.

[85] BA DiDonna and TC Lubensky, "Nonaffine correlations in random elastic media", *Physical Review E*, vol. 72, no. 6, pp. 066619, 2005.

[86] E. Conti and F.C. MacKintosh, "Cross-linked networks of stiff filaments exhibit negative normal stress", *Physical review letters*, vol. 102, no. 8, pp. 88102, 2009.

[87] H. Lee, B. Pelz, J.M. Ferrer, T. Kim, M.J. Lang, and R.D. Kamm, "Cytoskeletal deformation at high strains and the role of cross-link unfolding or unbinding", *Cellular and Molecular Bioengineering*, vol. 2, no. 1, pp. 28–38, 2009.

[88] ML Gardel, MT Valentine, J.C. Crocker, AR Bausch, and DA Weitz, "Microrheology of entangled f-actin solutions", *Physical review letters*, vol. 91, no. 15, pp. 158302, 2003.

[89] CP Broedersz, C. Storm, and FC MacKintosh, "Nonlinear elasticity of composite networks of stiff biopolymers with flexible linkers", *Physical review letters*, vol. 101, no. 11, pp. 118103, 2008.

[90] J.A. Åström, P.B.S. Kumar, I. Vattulainen, and M. Karttunen, "Strain hardening, avalanches, and strain softening in dense cross-linked actin networks", *Physical Review E*, vol. 77, no. 5, pp. 051913, 2008.

[91] AS Abhilash, P.K. Purohit, and S.P. Joshi, "Stochastic rate-dependent elasticity and failure of soft fibrous networks", *Soft Matter*, 2012.

[92] A.R. Bausch, F. Ziemann, A.A. Boulbitch, K. Jacobson, and E. Sackmann, "Local measurements of viscoelastic parameters of adherent cell surfaces by magnetic bead microrheometry", *Biophysical Journal*, vol. 75, no. 4, pp. 2038–2049, 1998.

[93] G.N. Maksym, B. Fabry, J.P. Butler, D. Navajas, D.J. Tschumperlin, J.D. Laporte, and J.J. Fredberg, "Mechanical properties of cultured human airway smooth muscle cells from 0.05 to 0.4 hz", *Journal of Applied Physiology*, vol. 89, no. 4, pp. 1619–1632, 2000.

[94] G.I. Bell, "Models for the specific adhesion of cells to cells", *Science*, vol. 200, no. 4342, pp. 618–627, 1978.

[95] E. Evans, D. Berk, and A. Leung, "Detachment of agglutinin-bonded red blood cells. i. forces to rupture molecular-point attachments", *Biophysical journal*, vol. 59, no. 4, pp. 838–848, 1991.